The Astrophysical Journal Supplement Series, 280:1 (56pp), 2025 September https://doi.org/10.3847/1538-4365/addabb

PHANGS-HST Catalogs for ∼100,000 Star Clusters and Compact Associations in 38 Galaxies. II. Physical Properties from Decision-tree-based Spectral Energy Distribution Fitting of NUV-*U*-*B*-*V*-*I* Photometry with Categorical Priors Set by Hα Emission, Cluster Morphology, and Other Auxiliary Information

David A. Thilker[1], Janice C. Lee[2,3], Bradley C. Whitmore[2], Daniel Maschmann[2,3], Kiana Henny[4], Rupali Chandar[5], Daniel A. Dale[4], Sinan Deger[6,7], Médéric Boquien[8], Aida Wofford[9,10], Leonardo Úbeda[2], Alessandro Razza[11], Ashley T. Barnes[12], Francesco Belfiore[13], Frank Bigiel[14], Kathryn Grasha[15,16,26], Brent Groves[17], Hwihyun Kim[18], Ralf S. Klessen[19,20], Justus Neumann[21], Francesca Pinna[21,22,23], M. Jimena Rodríguez[2,3], Erik Rosolowsky[24], Eva Schinnerer[21], and Thomas G. Williams[25]

[1] Department of Physics and Astronomy, The Johns Hopkins University, Baltimore, MD 21218, USA; dthilker@jhu.edu
[2] Space Telescope Science Institute, 3700 San Martin Drive, Baltimore, MD 21218, USA
[3] Steward Observatory, University of Arizona, Tucson, AZ 85721, USA
[4] Department of Physics and Astronomy, University of Wyoming, Laramie, WY 82071, USA
[5] University of Toledo, 2801 W. Bancroft Street, Mail Stop 111, Toledo, OH 43606, USA
[6] Institute of Astronomy, University of Cambridge, Madingley Road, Cambridge CB3 0HA, UK
[7] Kavli Institute for Cosmology Cambridge, Madingley Road, Cambridge CB3 0HA, UK
[8] Université Côte d'Azur, Observatoire de la Côte d'Azur, CNRS, Laboratoire Lagrange, 06000, Nice, France
[9] Instituto de Astronomía, Universidad Nacional Autónoma de México, Unidad Académica en Ensenada, Km 103 Carr. TijuanaEnsenada, Ensenada, B.C., C.P. 22860, Mexico
[10] Department of Astronomy and Astrophysics, University of California, San Diego, 9500 Gilman Drive, La Jolla, CA 92093, USA
[11] Departamento de Astronomía, Universidad de Chile, Camino del Observatorio 1515, Las Condes, Santiago, Chile
[12] European Southern Observatory, Karl-Schwarzschild Straße 2, D-85748 Garching bei München, Germany
[13] INAF–Osservatorio Astrofisico di Arcetri, Largo E. Fermi 5, I-50157, Firenze, Italy
[14] Argelander-Institut für Astronomie, Universität Bonn, Auf dem Hügel 71, 53121 Bonn, Germany
[15] Research School of Astronomy and Astrophysics, Australian National University, Canberra, ACT 2611, Australia
[16] ARC Centre of Excellence for All Sky Astrophysics in 3 Dimensions (ASTRO 3D), Australia
[17] International Centre for Radio Astronomy Research, University of Western Australia, 35 Stirling Highway, Crawley, WA 6009, Australia
[18] Gemini Observatory/NSF's NOIRLab, 950 N. Cherry Avenue, Tucson, AZ, 85719, USA
[19] Universität Heidelberg, Zentrum für Astronomie, Institut für Theoretische Astrophysik, Albert-Ueberle-Str 2, D-69120 Heidelberg, Germany
[20] Universität Heidelberg, Interdisziplinäres Zentrum für Wissenschaftliches Rechnen, Im Neuenheimer Feld 205, D-69120 Heidelberg, Germany
[21] Max-Planck-Institut für Astronomie, Königstuhl 17, D-69117, Heidelberg, Germany
[22] Instituto de Astrofísica de Canarias, C/ Vía Láctea s/n, E-38205, La Laguna, Spain
[23] Departamento de Astrofísica, Universidad de La Laguna, Av. del Astrofísico Francisco Sánchez s/n, E-38206, La Laguna, Spain
[24] Department of Physics, University of Alberta, Edmonton, AB T6G 2E1, Canada
[25] Sub-department of Astrophysics, Department of Physics, University of Oxford, Keble Road, Oxford OX1 3RH, UK
Received 2024 January 19; revised 2025 March 13; accepted 2025 March 14; published 2025 August 11

Abstract

This paper is the second in a series presenting the catalogs and properties of the largest sample to date of ∼100,000 star clusters and compact associations, in 38 spiral galaxies observed by the PHANGS-HST Treasury survey. Here, we present spectral energy distribution (SED) fitting techniques used to compute the age, mass, and reddening for each object. Our decision-tree-based strategy incorporates categorical priors on model age, reddening, and metallicity determined from additional observed parameters: localized Hα emission, source morphology, and demographic-specific locations in the *UBVI* color–color diagram. This approach is implemented to mitigate model degeneracies, particularly between young dusty clusters and old clusters with minimal dust, which can have identical optical colors. Results based on Hα narrowband imaging from the ground and from Hubble Space Telescope are intercompared, and contrasted with previous SED-fitting efforts. The fraction of the population that is subject to such priors is ∼14%, and of this subset, ∼63% of old globular clusters (GCs) have ages that change by a factor of 10 or more relative to unconstrained fits with single metallicity ($Z_{\odot}$) simple stellar population models. The demographics of the population are examined through age–mass and age–reddening diagrams (for individual galaxies as well as aggregated over the sample), and the GC mass function. We demonstrate relationships between cluster age–mass diagrams and properties of parent galaxies (galaxy morphology and location relative to the galaxy main sequence). We outline continuing efforts to improve the inference of physical properties, including the incorporation of JWST infrared photometry and updated synthesis models.

[26] ARC DECRA Fellow.

Unified Astronomy Thesaurus concepts: Open star clusters (1160); Globular star clusters (656); Galaxies (573); Galaxy evolution (594); Spiral galaxies (1560); Interstellar reddening (853); Barred spiral galaxies (136); Star clusters (1567); Young massive clusters (2049); Young star clusters (1833); OB associations (1140); Stellar associations (1582)

Materials only available in the online version of record: animations

1. Introduction

An ambitious long-term community goal in the study of nearby galaxies has been to build large samples of star clusters and stellar associations, and to systematically characterize their physical properties over a full span of galactic environments, from low-metallicity, low-mass dwarfs to massive dusty mergers.

Over the past decade, a number of Hubble Space Telescope (HST) programs, notably the Panchromatic Hubble Andromeda Treasury (PHAT; J. J. Dalcanton et al. 2012), Legacy ExtraGalactic Ultraviolet Survey (LEGUS; D. Calzetti et al. 2015), and Physics at High Angular resolution in Nearby GalaxieS (PHANGS)-HST (J. C. Lee et al. 2022), have targeted different segments of the nearby galaxy population ($\lesssim$20 Mpc) and conducted UV-optical inventories of their stellar populations. The resulting abundance of high-resolution, panchromatic imaging provides the long-sought opportunity to develop a full understanding of the star cluster life cycle: how clusters form, evolve, and eventually disrupt; and how their formation may depend on both the local environment and the properties of their host galaxies.

However, while the characterization of the observed photometric properties of star clusters and associations has provided clear new results (e.g., A. Adamo et al. 2017; M. R. Krumholz et al. 2019; D. Maschmann et al. 2024; and references therein), the study of the (1) factors that influence cluster formation, evolution, disruption; plus (2) timescales and efficiency of star formation feedback, require physical properties to be derived from the photometric observations, which have encountered roadblocks and remain subjects of active research (H. Baumgardt et al. 2019a; R. Gratton et al. 2019; A. T. Barnes et al. 2021, 2022; M. Chevance et al. 2022; L. Della Bruna et al. 2022; O. V. Egorov et al. 2023; J. Kim et al. 2023; F. Scheuermann et al. 2023; T. McQuaid et al. 2024; E. Lacchin et al. 2024).

Ages, masses, and reddenings have been determined for extragalactic cluster samples using integrated multiband photometry[27] and various spectral energy distribution (SED) fitting techniques (e.g., A. Adamo et al. 2010; R. Chandar et al. 2010; M. R. Krumholz et al. 2015a, 2015b; A. Adamo et al. 2017; M. Boquien et al. 2019; J. A. Turner et al. 2021). Following this process, physical properties have been derived for thousands of clusters, and have enabled much of the current generation of star cluster research, including studies of cluster mass and age functions (e.g., M. Fouesneau et al. 2014; G. Ashworth et al. 2017; R. Chandar et al. 2017; S. T. Linden et al. 2017; A. Mok et al. 2019), cluster formation and evolution in different environments (e.g., B. C. Whitmore et al. 2014; R. Chandar et al. 2017, 2023 K. Grasha et al. 2017a, 2017b; A. Adamo et al. 2020), and star formation efficiencies and timescales (e.g., K. Grasha et al. 2018, 2019; M. J. Rodríguez et al. 2023). Recent reviews of the field have been provided by M. R. Krumholz et al. (2019) and A. Adamo et al. (2020).

Well-documented limitations with current SED-fitting methods (S. Hannon et al. 2019; A. Adamo et al. 2020; B. C. Whitmore et al. 2020, 2023a; J. A. Turner et al. 2021; S. Deger et al. 2022; S. Hannon et al. 2022) have, however, not yet been systematically addressed. In particular, photometric degeneracies between age, metallicity, and reddening require further attention. The optical SEDs of young dusty objects and dust-free old clusters can mimic each other, while old metal-poor objects will have bluer SEDs than metal-rich analogs, which can be incorrectly fit with intermediate-age models if metallicity is not properly accounted for. B. C. Whitmore et al. (2023a) find that $\sim$ 10%–20% of all clusters detected in spiral galaxies can have ages that are incorrect by an order of magnitude, based on a study of four galaxies.

In D. Maschmann et al. (2024; hereafter Paper I), we present photometric catalogs for the largest census to date of $\sim$100,000 star clusters and compact associations resulting from the PHANGS-HST Treasury survey of 38 nearby spiral galaxies (J. C. Lee et al. 2022). Here, we describe categorical[28] prior SED-fitting techniques that explicitly address persistent issues involving the age–reddening–metallicity degeneracy. We apply these techniques to our catalogs and take a first look at the distributions of age, mass, and reddening across the full population. The general approach is to restrict the allowed range of simple stellar population (SSP)[29] model parameters for subsets of the population where other available information indicates that they are highly likely to be very young (primarily based on association with Hα emission), or very old based on lack of Hα emission *and* membership in the old globular cluster clump (OGCC) in the *UBVI* and *BVI* color–color diagrams (Paper I). Cluster morphology is also considered when sorting into population subsets. In essence, our method is capable of establishing empirically and/or physically motivated age–reddening-metallicity priors for two of the most distinct cluster subpopulations, specifically those that would otherwise suffer most seriously from model degeneracies. Note that we are not formally resolving SED degeneracies within the fitting process but instead aim to eliminate them in advance. In order to break them intrinsically within the SED fit, additional photometry in other band passes and regions of the spectrum would be needed. The physical parameters resulting from our "decision tree" SED-fitting approach (SED-TreeFit), together with those based on earlier

[27] For star clusters in galaxies beyond a few megaparsecs, essentially only the integrated light can be measured with present capabilities (as opposed to clusters in the Milky Way and Local Group galaxies, where the stellar populations can be resolved). Luminous stars such as RSGs and/or massive MS members are sometimes individually distinguishable in addition to unresolved cluster light.

[28] We introduce the terminology of "categorical" priors to distinguish our decision tree category-based priors (applied only to object subsets) from Bayesian priors (applied across entire object ensembles).

[29] C. Conroy (2013) describes an SSP as a "single, coeval stellar population at a single metallicity and abundance pattern," as opposed to a composite stellar population built from combining SSPs of varied age and metallicity plus effects of dust.

methods (Section 3; J. A. Turner et al. 2021, as used in DR3), will be provided in PHANGS-HST Data Release 4 and associated Catalog Release 3 (DR4/CR3).[30]

The remainder of this paper is organized as follows. In Section 2, we provide a brief summary of the PHANGS program and PHANGS-HST cluster and compact association catalogs used in this analysis. In Section 3, we summarize our initial approach for SED fitting (J. A. Turner et al. 2021), and review the issues to be addressed with categorical prior-based methods. In Section 4, we describe a new decision tree procedure implemented in our SED-fitting pipeline, which leverages additional information to limit the ranges of age, reddening, and metallicity allowed in the SED fitting. In Section 5, we present the main results of our new procedure, focusing on the distributions of age, mass, and reddening. We also quantify the differences between our new and previous results, and examine the impact on our understanding of star cluster and compact association properties. Section 5 ends with an exploratory look at the connection between galaxy properties and demographics of the cluster population. In Section 6, we provide key caveats for readers using the physical parameters in our catalogs and comment on future work. Finally, in Section 7, we summarize our main results. In the appendices, we describe our means of analysis for multimodal probability distribution functions, processing of ground-based and HST Hα images, criteria for evaluating which objects have locally associated Hα emission, and environment maps used in our decision tree to improve the age-dating results.

2. Data

2.1. The PHANGS-HST Survey

The PHANGS-HST sample includes 38 massive spiral galaxies located at distances between ≈5 and 23 Mpc. The galaxies cover morphological types Sa through Sd (including barred and unbarred galaxies), have star formation rates (SFRs) ranging from ∼0.2 to 17 $M_\odot\,\mathrm{yr}^{-1}$, specific SFRs (sSFRs) from $\sim10^{-10.5}$ to $10^{-9}\,\mathrm{yr}^{-1}$, and cloud-scale molecular gas surface densities (Σ_{mol}) from $\sim10^{0.5}$ to $10^{2.7}$ $M_\odot\,\mathrm{pc}^{-2}$ (see compilation in Table 1 of J. C. Lee et al. 2022). The nebular metallicities of the galaxies in the sample have been well established, including by PHANGS-MUSE, to be around $Z_\odot$ (e.g., D. Zaritsky et al. 1994; E. D. Skillman et al. 1996; J. Moustakas et al. 2010; B. Groves et al. 2023; F. Scheuermann et al. 2023).

From 2019 to 2021, the PHANGS-HST Treasury Survey obtained near-ultraviolet (NUV)-*U*-*B*-*V*-*I* imaging for 38 spiral galaxies to conduct a census of star clusters and associations in the context of the comprehensive effort of the PHANGS collaboration to enable the multiscale, multiphase study of star formation in the local universe. The foundation of PHANGS consists of four principal large surveys with the Atacama Large Millimeter/submillimeter Array (ALMA; A. K. Leroy et al. 2021), Very Large Telescope/MUSE (E. Emsellem et al. 2022), HST (J. C. Lee et al. 2022), and JWST (J. C. Lee et al. 2023). PHANGS is studying the relationships between molecular clouds, H II regions, dust, and star clusters across the large diversity of environments found in nearby galaxies. Beyond these four principal surveys, a wealth of additional supporting data is available and continues to be obtained by PHANGS, including Astrosat-UVIT far-ultraviolet (FUV)/NUV imaging (PI: E. Rosolowsky, H. Hassani et al. 2024), HST Hα narrowband imaging (PIs: R. Chandar, D. Thilker, F. Belfiore), ground-based wide-field Hα narrowband imaging (PIs: G. Blanc, I.-T. Ho), and H I 21 cm observations with the Very Large Array (PI: C. Eibensteiner) and MeerKAT (PIs: D. Utomo, D.J. Pisano). New large HST and JWST surveys to expand the number of galaxies with HST-JWST-ALMA data to 74 have been recently approved in 2023 (JWST Cycle 2 GO-3707, PI: A. Leroy; HST Cycle 31 GO-17502, PI: D. Thilker). To support community-led investigations with this wealth of data, PHANGS[31] has been producing and publicly releasing an extensive set of "science-ready" data products, including images and catalogs. PHANGS-HST data products are available via MAST;[32] and at doi:10.17909/t9-r08f-dq31.

2.2. Photometry of ∼100,000 Star Clusters and Compact Associations

The PHANGS-HST photometric catalogs of star clusters and compact associations result from a pipeline that supports end-to-end image processing, beginning with image drizzling and astrometric alignment (J. C. Lee et al. 2022); source detection, photometry, cluster candidate selection (S. Deger et al. 2022; D. A. Thilker et al. 2022); and morphological classification (W. Wei et al. 2020; B. C. Whitmore et al. 2021; S. Hannon et al. 2023). The pipeline is based on standard procedures for the production of catalogs of star clusters in nearby galaxies (e.g., B. C. Whitmore et al. 2010; A. Adamo et al. 2017), with new techniques for candidate selection based on multiple concentration indices calibrated with artificial star clusters and point sources (D. A. Thilker et al. 2022), aperture corrections (S. Deger et al. 2022), and automated morphological classifications with neural networks (W. Wei et al. 2020; S. Hannon et al. 2023). SED fitting of five-band NUV-*U*-*B*-*V*-*I* HST imaging has been previously performed for an initial catalog release (DR3/CR1)[33] as described in J. A. Turner et al. (2021) and summarized in Section 3, and will be improved upon by the techniques presented here. An overview of the overall pipeline is given by J. C. Lee et al. (2022), and the reader is referred to this paper and the others cited here for more information about the production of the catalogs.

As reported in Paper I, the PHANGS-HST survey and pipeline have yielded the largest census of star clusters and compact associations to date in nearby galaxies beyond the Local Group. The effort has resulted in uniform catalogs with aperture-corrected NUV-*U*-*B*-*V*-*I* photometry for ∼20,000 clusters and compact associations that have passed human inspection and morphological classification, and a larger sample of ∼100,000 classified by neural network models (W. Wei et al. 2020; B. C. Whitmore et al. 2021; S. Hannon et al. 2023), which were trained using human classifications. We have performed a range of analyses to validate the machine learning (ML) classifications, and these are summarized in Paper I Sections 2.3 and 4.2.

[30] https://archive.stsci.edu/hlsp/phangs/phangs-cat; doi:10.17909/jray-9798

[31] https://sites.google.com/view/phangs/home/data

[32] https://archive.stsci.edu/hlsp/phangs/phangs-hst

[33] DR3/CR1 only contained five galaxies. An internal release (IR4, 2023 February) to the PHANGS Collaboration included all 38 galaxies, processed as for the public DR3/CR1 but with the improvement of incorporating upper limits in the SED fitting. When we refer to our previous SED fitting in the manner of J. A. Turner et al. (2021) throughout the paper, we implicitly mean IR4.

A three-component morphological classification system, associated with the likelihood of gravitational boundedness for clusters older than 10 Myr, is used (D. Calzetti et al. 2015; A. Adamo et al. 2017; M. R. Krumholz et al. 2019; W. Wei et al. 2020, and references therein). Class 1 (C1) objects are clusters appearing symmetric and centrally concentrated. Class 2 (C2) objects are clusters appearing asymmetric and centrally concentrated. Class 3 (C3) objects are compact associations appearing multipeaked. See B. C. Whitmore et al. (2021) for a thorough review of morphological cluster classification in general, with discussion of various classification systems and procedures used over the years. We stress that C3 objects (compact associations) are retained in our work primarily to enable comparison with previous studies. Readers interested in a far more complete catalog of true associations should use the PHANGS-HST multiscale stellar association structures introduced by K. L. Larson et al. (2023).

The catalogs are essentially *V*-band selected, as the F555W imaging provides our candidate cluster source list, which is then down-selected by photometric and morphological criteria (see D. A. Thilker et al. 2022). The median m_V of the human-classified sample is about −8 mag (Vegamag),[34] while the machine-classified sample is ∼1 mag deeper. A circular aperture of 0.″16 radius (4 pixels) is used for all sources, which subtends 3.4 to 18 pc for the range of galaxy distances in the PHANGS-HST sample.

Paper I supports our PHANGS-HST sample-wide release of the cluster and compact association catalogs, and reviews observed photometric properties of the catalog (DR4/CR2). It describes the size and photometric depths of the samples detected in each galaxy, discusses completeness, and provides advice on catalog use. The observed properties of the population are studied in the context of the *UBVI* color–color diagram, and its three principal features: the young cluster locus (YCL), the middle-age plume (MAP), and the OGCC. The 2D spatial distribution of clusters and compact associations versus molecular clouds from PHANGS-ALMA is also examined.

3. Degeneracies in Star Cluster Age Dating

The SED-fitting procedures that were initially used to infer the age, mass, and reddening of star clusters and associations in an early set of PHANGS-HST catalogs are described in J. A. Turner et al. (2021). Catalogs of these properties have been published for five PHANGS-HST galaxies as part of DR3/CR1. For both the initial and new techniques used in this paper, star clusters and compact associations are assumed to be effectively single-age populations, and the SSP synthesis model predictions from G. Bruzual & S. Charlot (2003) are adopted. The SED-fitting method for sources in the PHANGS-HST catalogs is implemented in the publicly available Code Investigating GALaxy Emission (CIGALE) package[35] (D. Burgarella et al. 2005; S. Noll et al. 2009; M. Boquien et al. 2019) as detailed in J. A. Turner et al. (2021).

Fitting is performed on SEDs constructed from five-band (NUV-*U*-*B*-*V*-*I*) aperture-corrected photometry, including formal constraints from upper limits for non-detections. Our "general pipeline" model library (J. A. Turner et al. 2021, and herein, except for special cases) adopts the following parameters:

1. Solar ($Z_\odot$) metallicity models, with the single-age population implemented as a burst with a duration of 1 Myr.
2. The stellar IMF of G. Chabrier (2003) with standard mass limits of 0.1–100 $M_\odot$, assumed to be fully sampled.
3. No nebular contributions (neither emission lines nor nebular continuum).
4. The extinction curve of J. A. Cardelli et al. (1989) with $R_V = 3.1$.
5. Maximum $E(B-V) = 1.5$ mag, with steps of 0.01 mag starting from $E(B-V) = 0$ mag.
6. Ages spanning from 1 Myr to 13.75 Gyr, with linear steps of 1 Myr up to 10 Myr, and 100 logarithmic age steps of 0.03 dex from 11 Myr to 13.75 Gyr.

The rationale for these specific choices was presented in J. A. Turner et al. (2021). The SED fits produced for DR3/CR1 (and IR4) adopted the age and $E(B-V)$, yielding the minimum reduced χ^2 following J. A. Turner et al. (2021). As explained in Sections 4.1–4.4, for the new work of this paper, we instead take age and $E(B-V)$ from a determination of the most likely mode in CIGALE output probability density function (PDFs). In both cases, however, the stellar mass is then calculated from the mass-to-light ratio predicted for the inferred age, together with the extinction-corrected luminosity.

SED fits that rely only on broadband NUV-*U*-*B*-*V*-*I* integrated photometry have a number of degeneracies, which can be significantly amplified by photometric uncertainties. Although this combination of five filters probes the SED blueward of the 4000Å break and is an improvement over the three filter $B-V-I$ combination commonly used for stellar populations studies, similar NUV-*U*-*B*-*V*-*I* SEDs can still correspond to very different sets of physical properties. The SED shape is degenerate among several pairs and even triples of age, reddening, and metallicity, if all parameters are allowed to vary freely.

These degeneracies are illustrated in Figures 1 and 2. The BC03 solar metallicity SSP model track is shown in the *UBVI* color–color diagram as a cyan line (left panels in Figures 1 and 2). The reddening vector will cross multiple points in the track for various young and old models. For example, if the reddening vector is placed at the beginning of the $Z_\odot$ track (at 1 Myr) it will intersect the model track at ∼7 Myr and 20 Myr (blue points in Figure 2 left panels, and blue age distribution in Figure 2 right panels). These multipeaked age distributions based on standard fitting methods (e.g., minimum χ^2 fits) show the severity of the problem. Essentially, for any object in the portion of a color–color slice "downstream" (redward) of the last slice/model crossing, the standard SED-fitting method will allow solutions tied to all crossings without any preference between them other than what additional constraint the NUV band (not shown in this color space) can provide.[36] Even having access to the entire broadband NUV-optical SED is not sufficient to eliminate age–reddening degeneracy: e.g.,

[34] Vega magnitudes are used in this paper to facilitate comparison to previous work, but flux densities (in mJy) are given in the published catalogs.

[35] https://cigale.lam.fr

[36] Note that we perform SED fits to age and reddening using all available photometric bands (e.g., F275W, F336W, F435W, F555W, and F814W for PHANGS-HST), rather than fitting in 2D color–color diagrams (a projection which incurs information loss). The color–color diagrams, however, frequently simplify visualization of what is happening in the higher-dimensional SED space, and hence are used extensively herein.

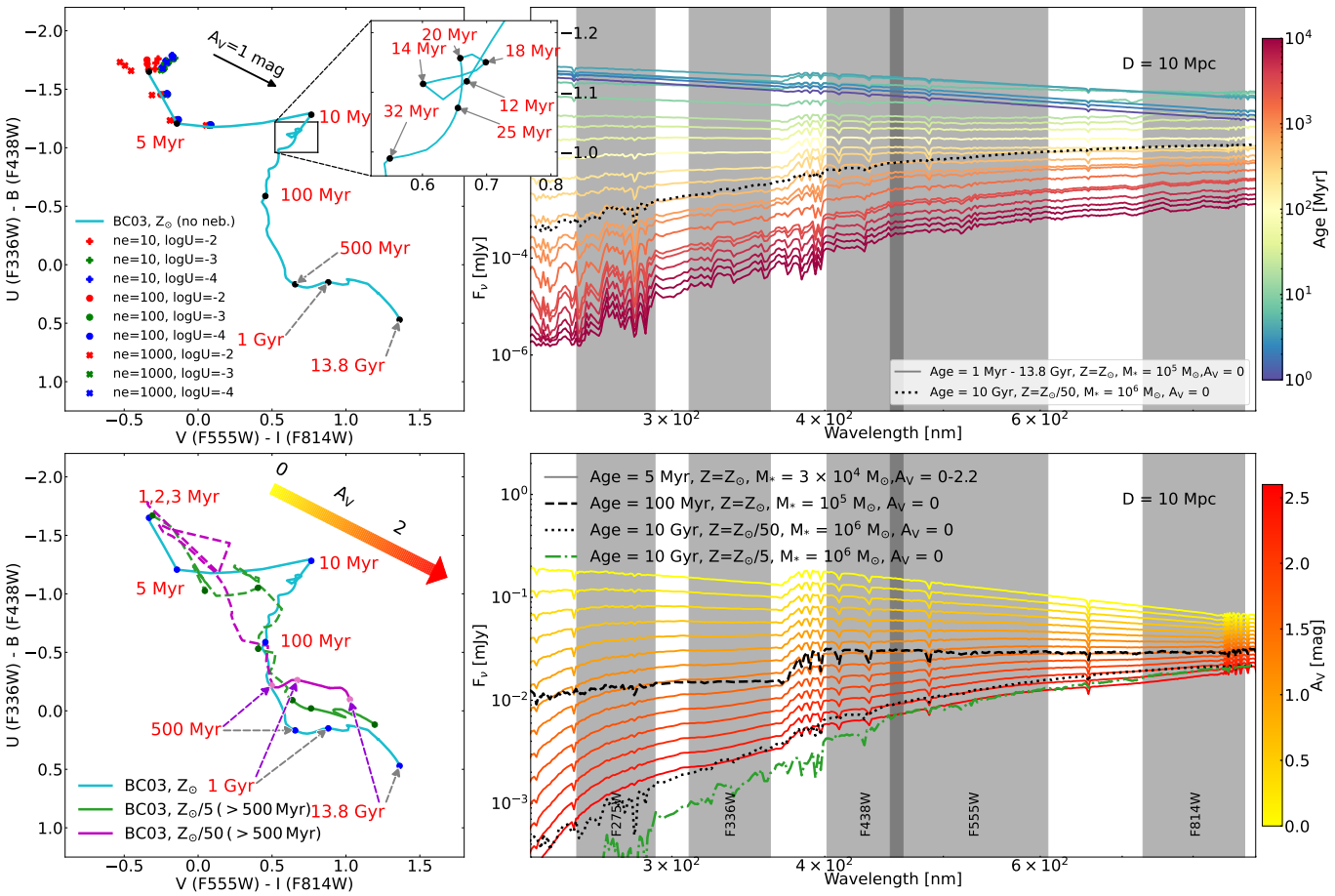

Figure 1. Illustration of the age–reddening and age–metallicity degeneracies for star clusters, using the single stellar population G. Bruzual & S. Charlot (2003) SSP model. Left panels: time evolution of the SED for an aging cluster as projected into the *UBVI* color–color diagram, oriented so that the youngest model (1 Myr) appears at the upper left corner, and age increases toward the bottom right. A reddening vector is shown in both color–color diagrams. Note how a reddened cluster of 1–3 Myr age (if given sufficient dust) can closely mimic the colors of clusters in two older, degenerate age ranges. Model tracks for different metallicities are indicated: $Z_\odot$ (cyan), $Z_\odot/5$ (green, lower panel only), $Z_\odot/50$ (purple, lower panel only). The first 500 Myr of the subsolar metallicity tracks are dashed to de-emphasize them, as such young metal-poor populations are not expected in our galaxies. With colored dots, we show model predictions including nebular continuum and emission line contributions for young ionizing clusters assuming f_{esc}=0.5 (see Section 4.2). The zoomed inset in the top panel features an expanded view of loops in the SSP evolutionary track between 20–30 Myr. The colors of old metal-poor populations are bluer than those of solar metallicity populations with the same age, and can be incorrectly fit with much younger models if solar metallicity tracks are used. Right panels: model SEDs, with the wavelength ranges sampled by the HST filters shaded in gray. The top right panel shows intrinsic (dust-free) $Z_\odot$ models at selected ages spanning from 1 Myr to 13.8 Gyr (colored lines). The top right panel also includes one model for $Z_\odot/50$ and 10 Gyr, demonstrating age–metallicity degeneracy (e.g., note the similarity to intermediate-age $Z_\odot$ models). The bottom-right panel shows fixed-age (5 Myr) $Z_\odot$ models with reddening varied from $A(V) =$ 0.0–2.6 mag (colored lines). Three additional models are overlaid to further illustrate degeneracies: 100 Myr SSP with $Z_\odot$ having $A(V) = 0$ (dashed black line); 10 Gyr, $Z_\odot/50$, $A(V) = 0$ (dotted black); and 10 Gyr, $Z_\odot/5$, $A(V) = 0$ (dotted–dashed green line).

the lower right panel in Figure 1 shows that an SED corresponding to 100 Myr, $Z = Z_\odot$ and $A(V) = 0$ mag (dashed black spectrum) is similar to a 5 Myr old $Z = Z_\odot$ model with $A(V) \gtrsim 1$ mag. Figure 2 also demonstrates that photometric uncertainty plays a role in the severity of degenerate modeling outcomes. Notice how in the bottom half of Figure 2 (presenting the faint clusters specifically) the PDFs of $\log(t\ \mathrm{yr}^{-1})$ become broader (even merging in some cases) and entirely new peaks are present for each color–color sliced subset, representing other degenerate options. Paper I quantifies our typical photometric uncertainty versus position in color–color space.

Model degeneracy becomes even more complex if metallicity is allowed to vary. This can be seen in the left bottom panel of Figure 1, where we plot model tracks for $Z = Z_\odot/50$ and $Z_\odot/5$ in addition to the solar metallicity track. Because it is unlikely, in the PHANGS-HST galaxy sample, for the metallicity to be so low for populations which formed in situ over the past ≈0.5 Gyr we de-emphasize the low-metallicity tracks for ages younger than this. In the color–color diagrams, metallicity-related degeneracies can be identified as metallicity-diverse track crossings for lines oriented with the reddening vector, but they are also illustrated in the lower right panel of Figure 1 where we demonstrate similarity between the SED of a 5 Myr, $A(V) = 2.6$, $Z_\odot$ cluster with a 10 Gyr, dust-free, $Z_\odot/50$ cluster.

In the next section, we develop improved SED-fitting procedures, which enable consideration of additional information about the environment and morphology of each object while also integrating prior knowledge of population demographics in color–color space, to improve age dating of clusters and compact associations.

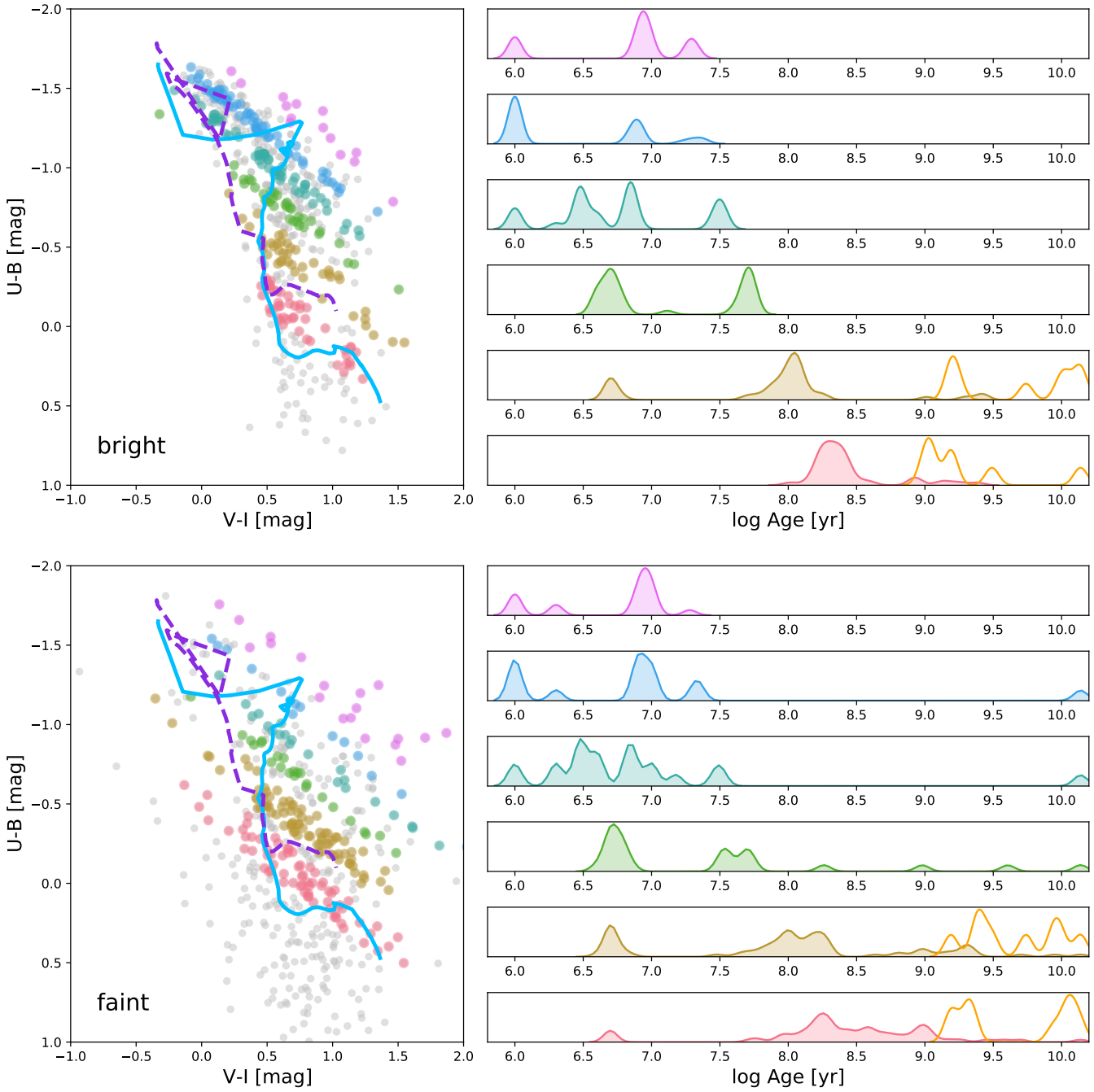

Figure 2. Illustration of age degeneracies resulting from SED fitting of NUV-*U*-*B*-*V*-*I* HST star cluster photometry for NGC 4321 ML Class 1 and 2 objects. Left panels: slices in the *UBVI* color–color diagram defined in the direction of the reddening vector. The model tracks are the G. Bruzual & S. Charlot (2003) $Z_{\odot}$ (cyan solid) and $Z_{\odot}/50$ (purple dashed) predictions. Right panels: the KDE-smoothed inferred age distribution for each of the color–color slices, normalized to unit peak, and color coded to match the left panels. Top: Plots in the upper half of the figure show clusters in the brightest 33% of the catalog, having m(F555W)$\lesssim$ 23.1. Bottom: The plots in the lower half show the clusters belonging to the faintest 33% of the magnitude distribution, having m(F555W)$\gtrsim$ 23.9. We show the PHANGS_AGE_MINCHISQ values (following J. A. Turner et al. 2021)—not the SED-TreeFit outcomes of our present work. Note how each of the age distributions has more than one peak, even if the slice only intersects the model curve once (e.g., orange and magenta). The latter point is partially due to photometric uncertainty, allowing clusters to latch onto nearby model points even if they are off the reddening vector. With thick orange curves, we show the distribution of the ages based on the SED-TreeFit method in this paper for the subset of old globular clusters in the two reddest color–color slices.

4. Improved Cluster-age Dating Rooted in a Decision Tree Framework

4.1. Overview and SED-TreeFit Method Architecture

To mitigate age-dating failures resulting from fitting the NUV-*U*-*B*-*V*-*I* photometry of diverse objects to a single set of model assumptions, we introduce a decision tree-based SED-fitting process. The method uses additional information to constrain the range of allowed model parameters object by object (in essence setting custom priors to eliminate any degenerate, but implausible, solutions) by assigning catalog objects to different categories (tree branches) ahead of fitting, leading to improvements in the reliability of age, mass, and reddening estimates. There are two regimes where our new approach provides a critical step forward:

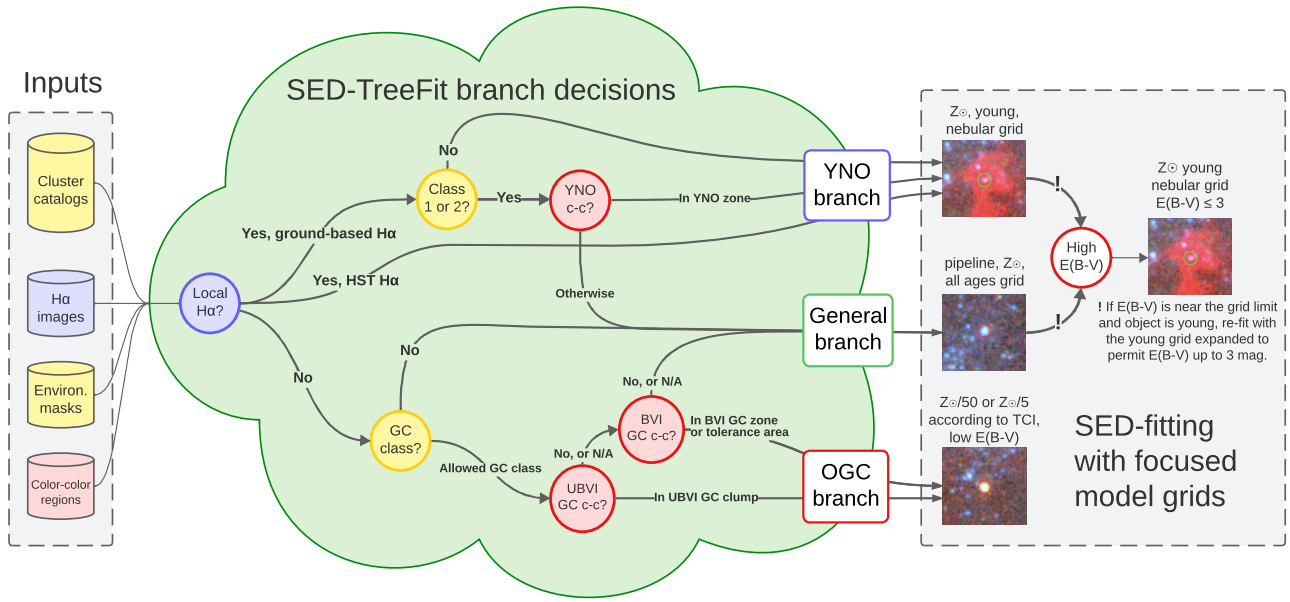

Figure 3. Schematic illustration of our decision tree for improving cluster SED-fitting outcomes and mitigating age–reddening–metallicity degeneracies by employing additional information, in this case from narrowband Hα imaging, cluster morphological classification, and color–color (c-c) space segmentation. SED-TreeFit decision points (or "nodes") guiding the disposition of objects through the tree are marked with circles having thick outlines, which have been color coded to match the variety of input information they employ (indicated at left).

1. Very young, often reddened clusters (age $\sim$ 1–several Myr; hereafter "young nebular objects" or YNOs)
2. Very old clusters (age $\gtrsim$ few to many Gyr; hereafter "old globular clusters" or OGCs).

Many of the strategies implemented in the decision tree analysis, which we also refer to as the "SED-TreeFit" method, were initially described by B. C. Whitmore et al. (2023a). The decision tree (see Figure 3) requires four inputs: (1) the cluster or compact association photometric catalogs (as described in Paper I), including morphological classifications, (2) measurements of Hα emission and identification of compact nebular structures (based on either ground-based or HST-based Hα images as described in Appendix B), (3) environmental masks specifying the location of spiral arms in each galaxy (see Appendix C), and (4) definition of an OGC region and YNO zone in color–color diagrams.

A branch schematic of the SED-TreeFit method is featured in Figure 3. The four inputs that go into the decision tree are shown on the left. The first decision point in the tree (shown as a blue circle labeled "Local Hα?") evaluates whether or not the source has locally associated Hα emission (see Section 4.3 and Appendix B). If the answer is "yes," then the source is sent onward to the YNO branch; if "no," then to the OGC branch, as shown in the Figure. There are two more decision points along the YNO branch (details in Section 4.3) and up to three along the OGC branch (Section 4.4). Any sources failing to fully traverse either branch are fit using a default, general pipeline model library (J. A. Turner et al. 2021), but selecting the most likely mode of the output parameter distribution instead of the single best model (with minimum χ^2). See Appendix A for a full description of how multiple modes of CIGALE PDFs are identified and characterized.

Five possible sets of SSP model grids are used for SED-TreeFit processing:

1. The default "general pipeline" grid, which assumes solar metallicity ($Z_\odot$, $Z = 0.02$), allows $E(B-V) = 0.0 - 1.5$ mag and all ages (see Section 3),
2. Two "young" grids which assume solar metallicity with nebular contributions to broadband flux and restrict the fitting to ages $\leqslant$5 Myr, with $E(B-V)$ maximum values of 1.5 or 3.0 (the latter only in special cases),
3. Two "metal-poor" grids that impose a maximum $E(B-V)$=0.2, allow all ages, and assume either $Z_\odot/50$ or $Z_\odot/5$ metallicity.[37]

The conditions and observables that determine which model grid will be used (per object) are summarized in Table 1, and described in detail in Sections 4.3 and 4.4. Note that in practice we actually do run all objects in the context of each model grid and plan to release supplemental data tables with such alternative outcomes at the time of MAST HLSP publication, allowing a user to change the selected model grid post facto if the SED-TreeFit branch assignment of an object has reason to be challenged.

4.2. Primer on SSP Models including Nebular Emission

As shown by earlier works (e.g., A. Adamo et al. 2017; N. Byler et al. 2017; R. Orozco-Duarte et al. 2022; E. R. Stanway & J. J. Eldridge 2023), allowance for nebular contributions to SSP model predictions (even for broad filters) is very important (it significantly alters colors), but it also imparts complexity in terms of dependencies on specific assumptions. Figure 4 demonstrates the way in which predicted broadband colors vary according to the assumed radiation field intensity (e.g., ionization parameter = log U) and physical conditions (e.g., electron density, n_e) in the H II

[37] Low Z BC03 models are available for $Z_\odot/200$, $Z_\odot/50$, and $Z_\odot/5$, but we adopted $Z_\odot/50$ and $Z_\odot/5$ as representative values for the development and initial application of our methods. Section 6.2 places this issue in the context of our future modeling and observational plans.

Table 1
SED-TreeFit Parameter Choices

Parameter	Value
(A) Parameters Influencing the Flow of Objects through the SED-TreeFit Decision Tree	
Hα surface brightness threshold	Ground-based Hα: $S(\mathrm{H}\alpha)_{\mathrm{bkgdsub}} = 8.4 \times 10^{-16}$ erg s^{-1} cm^{-2} arcsec^{-2} HST Hα: variable $S(\mathrm{H}\alpha)_{\mathrm{bkgdsub}}$ (1.1–20 $\times 10^{-16}$ erg s^{-1} cm^{-2} arcsec^{-2})
Hα diffuse background filtering scale (std. deviation)	Ground-based Hα: $\simeq$ 90 pc; HST Hα: $\simeq$ 10 pc
Hα segment-to-object linking criteria	(1) Object centered within the Hα segment, or (2) Hα segment maximum within the object's photometric aperture, or (3) Hα segment(s) cover $\geqslant$50% of the object's photometric aperture
Morphological class filters	OGC branch: permit Class 1 and Class 2 (outside spiral arm mask) YNO branch: permit Classes 1, 2, 3 Human classifications given preference when available
OGC color–color region	Polygons determined based on density values from Paper I, with options between inclusive (default) and restrictive regions as specified in Figure 6 and Section 4.4
YNO color–color zone	$(V-I) \geqslant 1.4$ or $(U-B) \leqslant 0.64\ ^{*}(V-I) - 1.0$ if *UBVI* detected, or $(V-I) \geqslant 1.4$ or $(B-V) \geqslant 0.73\ ^{*}(V-I) - 0.65$ if *BVI* detected, but only enforced for ground-based Hα SED-TreeFit processing of Class 1+2
(B) Parameters Adopted for CIGALE SED Modeling	
Applicable to all SED fits	
SFH	$\approx$instantaneous burst, $\delta t = 1$ Myr duration (implemented as 10 0.1 Myr minibursts)
SSP model	G. Bruzual & S. Charlot (2003)
IMF	G. Chabrier (2003); [0.1:100] $M_{\odot}$; fully sampled
YNO grids	
Metallicity	$Z = 0.02$ ($Z_{\odot}$)
Reddening and extinction	$E(B-V) =$ [0:1.5] mag; $\Delta = 0.01$ mag; in special cases up to 3.0 mag $R_V = A_V/E(B-V) = 3.1$
Ages	[1:5] Myr with $\Delta T = 1.0$ Myr
Gas covering fraction	0.5 $\Rightarrow$ CIGALE $f_{\mathrm{esc}} = 0.5$
Ionization parameter	$\log U = -3.6$
Electron density	$n_e = 10$ cm^{-3}, $\sim$ equivalent to $n_e = 100$ cm^{-3} for $\log U \lesssim -3$
Standard pipeline grid	
Metallicity	$Z = 0.02$ ($Z_{\odot}$)
Reddening and extinction	$E(B-V) =$ [0:1.5] mag; $\Delta = 0.01$ mag; $R_V = A_V/E(B-V) = 3.1$
Ages	[1:10] Myr with $\Delta T = 1.0$ Myr; [11:13750] Myr with $\Delta \log(T/\mathrm{Myr}) = 0.03$
Gas covering fraction	0.0 $\Rightarrow$ CIGALE $f_{\mathrm{esc}} = 1.0$
OGC grids	
Metallicity	$Z = 0.0004$ ($Z_{\odot}/50$) if $\mathrm{TCI}_{UBVI} < 2.16$, or if $\mathrm{TCI}_{BVI} < 1.83$ when only *BVI*-detected; $Z = 0.004$ ($Z_{\odot}/5$) otherwise
Reddening and extinction	$E(B-V) =$ [0:0.2] mag; $\Delta = 0.01$ mag; $R_V = A_V/E(B-V) = 3.1$
Ages	[1:10] Myr with $\Delta T = 1.0$ Myr; [11:13750] Myr with $\Delta \log(T/\mathrm{Myr}) = 0.03$
Gas covering fraction	0.0 $\Rightarrow$ CIGALE $f_{\mathrm{esc}} = 1.0$

Note. The extinction curve adopted is from J. A. Cardelli et al. (1989), appropriate for the Milky Way. For the YNO and standard pipeline model grids, in particular for dusty sources where $E(B-V)$ is $\geqslant$1.45 after initial fitting, we allow an elevated reddening limit of $E(B-V) =$ 3 mag but only if the age before such modification is $\leqslant$7 Myr.

region. One can see that the impact of nebular emission, from lines and nebular continuum, is most significant[38] for the first 3 Myr. Generally, the $U-B$ color at these ages becomes universally bluer, but the predictions in $V-I$ can shift either red- or blueward, with $\log U = -2$ (harder intensity radiation) producing bluer $V-I$ than for $\log U = -3$ or -4. The sense of the later effect is true at all ages expected to have nebular contributions, though it becomes progressively less pronounced by 5 Myr. Electron density also plays a role in setting the degree of nebular shift, but only for hard impinging

[38] Assuming BC03 models, which do not account for binarity or rotation. Such effects, if included, could lengthen the time period of substantial deviation between predictions with nebular contributions and those without.

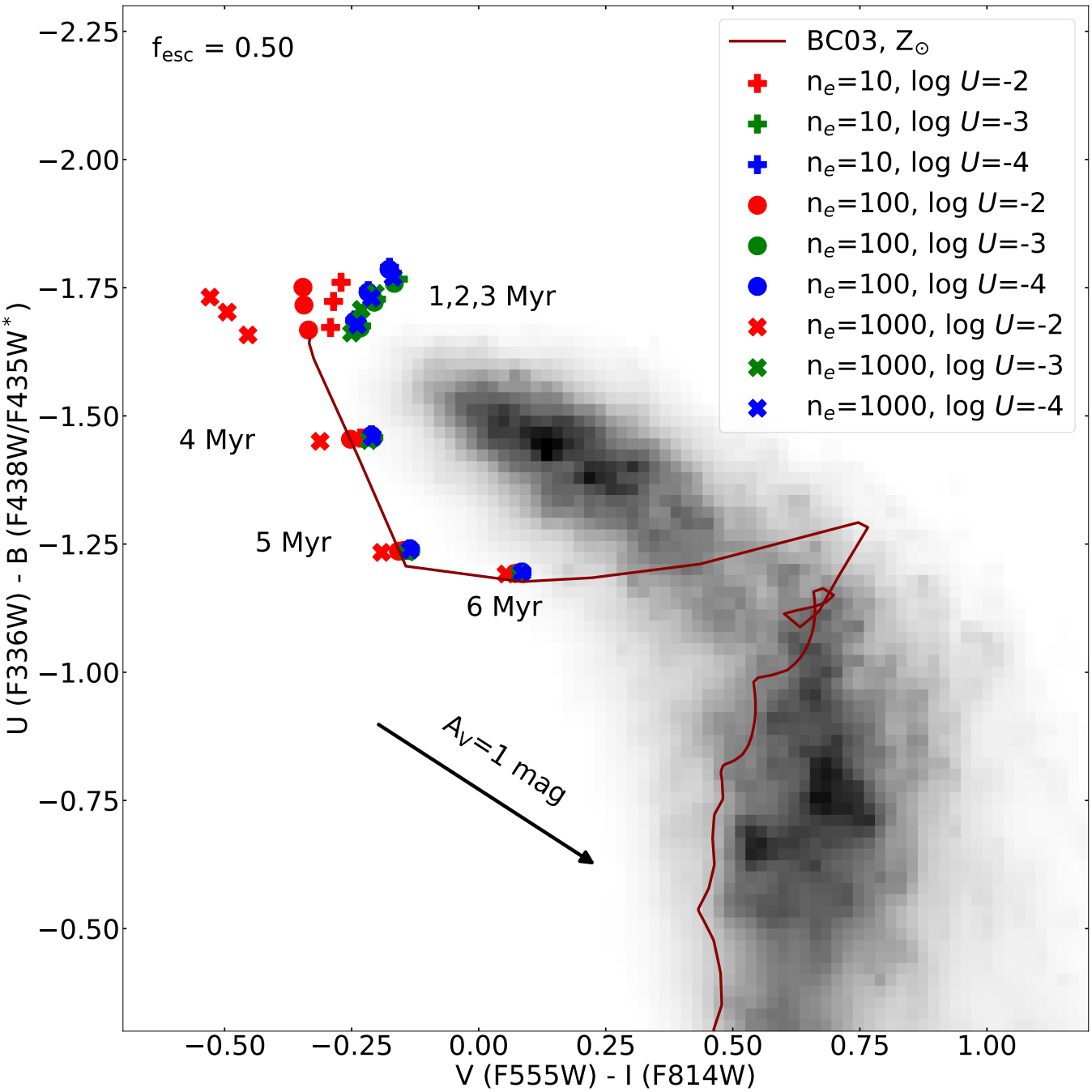

Figure 4. Zoomed-in view of the young/blue portion of *UBVI* color–color diagram showing BC03 models with CIGALE inclusion of nebular contributions (continuum and line) to the broadband flux. Models with such nebular emission are plotted as colored symbols, following the choices of log U and n_e indicated in the legend. This plot assumes $f_{esc} = 0.5$. For comparison, we show the distribution of observed YCL and MAP clusters as defined in Paper I. The animated version of the figure shows different escape fractions.

(An animation of this figure is available in the online article.)

radiation fields. Changes from $n_e = 10$ to $1000\,\mathrm{cm}^{-3}$ have essentially no effect for log $U = -3$ or -4. As indicated in Table 1, we adopted log $U = -3.6$ and $n_e = 10\,\mathrm{cm}^{-3}$ for our work, based on the detailed H II region analyses from PHANGS-MUSE (A. T. Barnes et al. 2021, 2022; B. Groves et al. 2023). Combining PHANGS-MUSE and PHANGS-HST Hα data sets, A. T. Barnes et al. (2022) find that typical n_e at HST resolution in NGC 1672 H II regions is usually between 10 and $100\,\mathrm{cm}^{-3}$. Concerning our adopted log U, we note that the reported measurements in B. Groves et al. (2023) are a factor of 100 too large, due to a unit conversion error that was only discovered after publication.

The preceding statements are for our "young" grid assumption of $f_{esc} = 0.5$. This choice is broadly consistent with a diffuse ionized gas (DIG) fraction of $\lesssim$0.5 (D. A. Thilker et al. 2002; M. S. Oey et al. 2007; F. Belfiore et al. 2022). Variation of the assumed ionizing photon leakage (e.g., J. W. Teh et al. 2023) will modulate the degree of changes,

in the sense expected—a reduction in color shift for increasing f_{esc}. An animated version of Figure 4 illustrates this by cycling through predictions generated for $f_{esc} = 0.0$, 0.25, 0.50, 0.75, 1.0. We present the predicted nebular models in *UBVI* color–color space because it is our workhorse diagram, but we point out that changes are even more pronounced in $B - V$ (in the *BVI* color–color diagram).

4.3. The YNO Branch: Improvements to Young Cluster Ages

As introduced in Section 4.1, objects with associated local Hα emission enter the YNO branch of our decision tree (at the blue circle labeled "Local Hα?" in Figure 3). These objects are very likely to be young clusters (YCs)/young associations, since they generate ionizing Lyman continuum photons, and should be most properly modeled with a CIGALE grid accounting for nebular contributions. The specific criteria for establishing a linkage between source and nebula are explained in detail in Appendix B, but in brief, we rely on a combination of blob/segment-based proximity and covering checks, modulated by an Hα surface brightness threshold in the immediate vicinity, toward/within the HST photometry aperture. Surface brightness $S(\mathrm{H}\alpha)_{\mathrm{bkgdsub}}$ is evaluated on the same locally background subtracted imaging (Appendix B.2) we use for blob identification (Appendix B.3), mitigating dependence on diffuse Hα emission from branch assignment decisions.

We note that the spatial resolution of the ground-based Hα images ($\sim$70 pc at the typical 15 Mpc distance of PHANGS-HST galaxies) available for all 38 galaxies currently limits our ability to unambiguously associate individual clusters with Hα emission in some cases (see Section 4.5 and Appendix B, Figure 31). This situation will be improved in the future by always using high-resolution narrowband Hα imaging from HST, instead of the ground-based data set. Three HST programs (GO-17126, PI: R. Chandar; GO-17502, PI: D. Thilker; GO-17457 PI: F. Belfiore) are obtaining Hα narrowband imaging for the entire PHANGS sample. In the present paper, we include SED-TreeFix processing based on HST Hα for 17 galaxies.

We explain how we set the $S(\mathrm{H}\alpha)_{\mathrm{bkgdgsub}}$ threshold in Appendix B.4 (Figure 32), uniformly for ground-based Hα decision tree work but variably for HST Hα decision tree processing. To further motivate the fixed ground-based value of the $S(\mathrm{H}\alpha)_{\mathrm{bkgdgsub}}$ threshold, Figure 5 presents the *UBVI* color–color diagrams of individual galaxies with points color coded above a trial $S(\mathrm{H}\alpha)_{\mathrm{bkgdsub}}$ threshold choice. Such figures were produced for several surface brightness thresholds and all galaxies. The chosen $\mathrm{S}(\mathrm{H}\alpha)_{\mathrm{bkgdsub}}$ threshold (Table 1 and Appendix B.4) was found to provide a reasonable distinction between young ionizing clusters and contaminants. Higher threshold values progressively appeared to miss more bona fide ionizing clusters than they eliminated contaminants. This being said, even our adopted threshold was intentionally conservative (high) to avoid overassignment of objects to the YNO branch.

The precision with which we can associate immediately localized Hα emission to individual objects is superb for HST Hα images, given the parsec-scale resolution. For this reason, any candidate YNO according to HST is automatically taken to be a confirmed YNO without further assessment (bypassing the other YNO-related decision points). However, we note that due to morphological evolution (expansion of shell/bubble-like H II regions beyond the PHANGS-HST photometric aperture), objects that have spatially extended, structured nebulae are not always identified as candidate YNOs. This is not a problem, as the general pipeline grid still permits SED fits with very young ages (they are not exclusive to the YNO grid), and in fact, objects having Hα shells beyond the aperture should be modeled without nebular contributions.

In the YNO branch, for runs based on ground-based Hα imaging rather than HST narrowband data, the next node divides potential YNO objects by morphological class (shown in Figure 3 as a yellow circle labeled "Class 1 or 2?"). Preference is given to the human classification versus the ML classification in cases of disagreement. Class 3 objects (compact associations) with local Hα are fully accepted as members of the YNO population at this decision point, given their low probability of being evolved, whereas Class 1 or 2 clusters are further evaluated (next paragraph) in order to prevent any false positive YNO assignments for intermediate-age or globular clusters (GCs) that occupy areas of structured H II emission purely by chance.

The final node along the YNO branch (upper red circle labeled "YNO c-c?") checks if the Hα-emitting source satisfies the following *UBVI* color criteria, either $V-I \geqslant 1.4$ or $(U - B \leqslant 0.64 * V - I - 1.0)$ (i.e., a maximum allowed $U - B$ at a given $V-I$ blueward of $V-I=1.4$) to prevent contamination by objects whose colors are inconsistent with a reddened SSP with age $\leqslant$5 Myr. This *UBVI* YNO color–color zone lies above/right of the dashed blue line segments indicated in Figure 5. The vertical portion of the *UBVI* YNO color–color zone boundary allows for YNO branch inclusion of some highly reddened Hα bright clusters, which sometimes lie below the diagonal boundary if it were extended to beyond $V-I \geqslant 1.4$ (e.g., see several examples in the NGC 1365 and NGC 3627 panels). If an object cannot be evaluated in *UBVI* color–color space, due to a nondetection or missing data, we instead use *BVI*-based YNO color zone criteria: $V - I \geqslant 1.4$ or $(B - V \geqslant 0.73 * (V - I) - 0.65)$. Candidate YNO objects that fail the YNO color–color node, i.e., Class 1 or 2 clusters outside the YNO color–color zone that have apparent Hα via ground-based imaging, are disqualified and assigned to the general pipeline grid.

Objects eventually assigned to the YNO branch are fit with $Z = Z_{\odot}$ SSP models with ages between 1 and 5 Myr, including nebular contributions and requiring $E(B - V) \leqslant 1.5$ mag. For YNO objects, the age corresponding to the best mode of the resulting probability distribution function for the "young model" grid is adopted.

For a few galaxies with very dusty areas (e.g., NGC 1365), examination of the age-reddening diagram showed a ceiling of young objects at the maximum $E(B - V)$ of 1.5 mag. For these specific sources ($E(B - V) \geqslant 1.45$ and age $\leqslant$7 Myr), we increase the maximum $E(B - V)$ to 3.0 mag. This allowance for extra reddening is also considered for sources our decision tree assigns to the general pipeline model grid. Overall, in the ML C1+C2 catalog, about 0.05% (17) of the 36,180 clusters are affected, whereas the percentage is smaller for ML Class 3, with only 0.007% (29) of 59,610 compact associations qualifying for a higher reddening of >1.5 mag during SED fitting.

4.4. The OGC Branch: Improvements to Old Cluster Ages

Objects that do not meet the criteria for localized Hα emission (failing the blue decision point/node in Figure 3) provisionally enter the OGC branch for possible fitting with

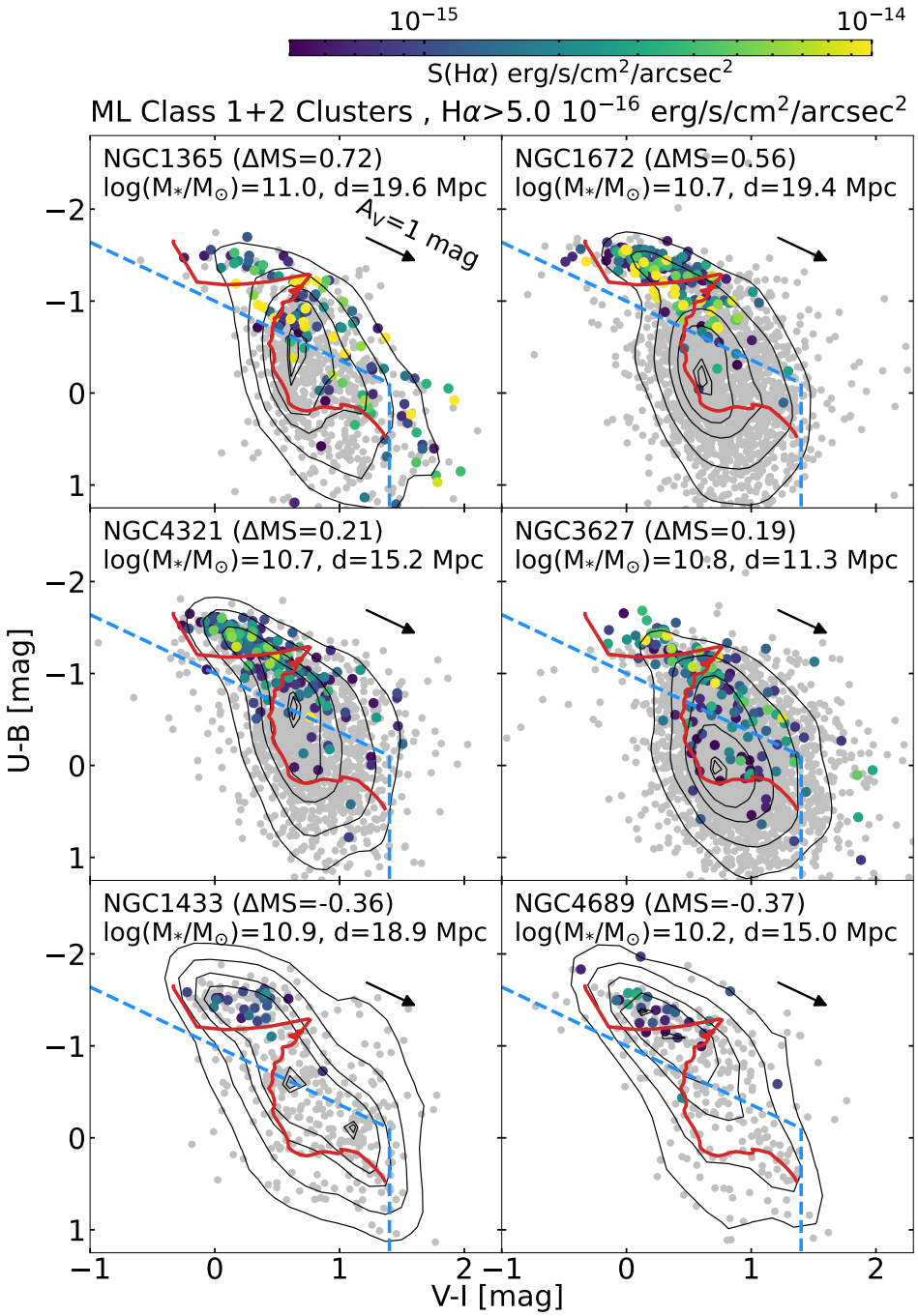

Figure 5. Location of ML C1+C2 clusters in the *UBVI* color–color diagram with ground-based Hα surface brightness higher than 5×10^{-16} erg s^{-1} cm^{-2} arcsec^{-2} (colored points). Dashed blue line segments mark the boundary of the *UBVI* YNO color–color zone (extending above and to the right) used for the final check of the YNO branch of the decision tree in its ground-based implementation (Figure 3). Six representative galaxies are shown from the full sample. Panels are ordered top to bottom according to decreasing ΔMS, the SFR offset from the star-forming galaxy MS. A color bar indicates the Hα surface brightness. Clusters not meeting the *S* (Hα) threshold (indicated near the top of the plot) are shown in gray. Contours indicate the density of all ML C1+C2 clusters in the diagram. The red line is a BC03 $Z = Z_\odot$ evolutionary track.

one of our two metal-poor ($Z_\odot/50$ or $Z_\odot/5$), low-reddening CIGALE model grids.

The second node of the OGC branch excludes Class 3 compact associations (yellow circle labeled "GC class?" in Figure 3) since they are expected to be young (e.g., A. Adamo et al. 2017, Paper I), and only allows Class 1 and 2 star clusters to proceed if conditions of this paragraph are met. As such, this node of the OGC branch filters out a subset of asymmetric clusters having an enhanced probability of formation over the last several hundred million years based on their proximity to spiral arms. Regions identifying the spiral arms based on the work of M. Querejeta et al. (2021) are used, and further description is given in Appendix C. Only Class 2 clusters are tested in this way. Class 1 clusters pass this node regardless of whether they fall in the spiral arm regions. We adopted this approach since Paper I demonstrated that Class 1 clusters exhibit a distinct overdensity in the UVBI color–color diagram corresponding to the OGC population (Paper I, Figure 8), whereas Class 2 did not. As in the YNO

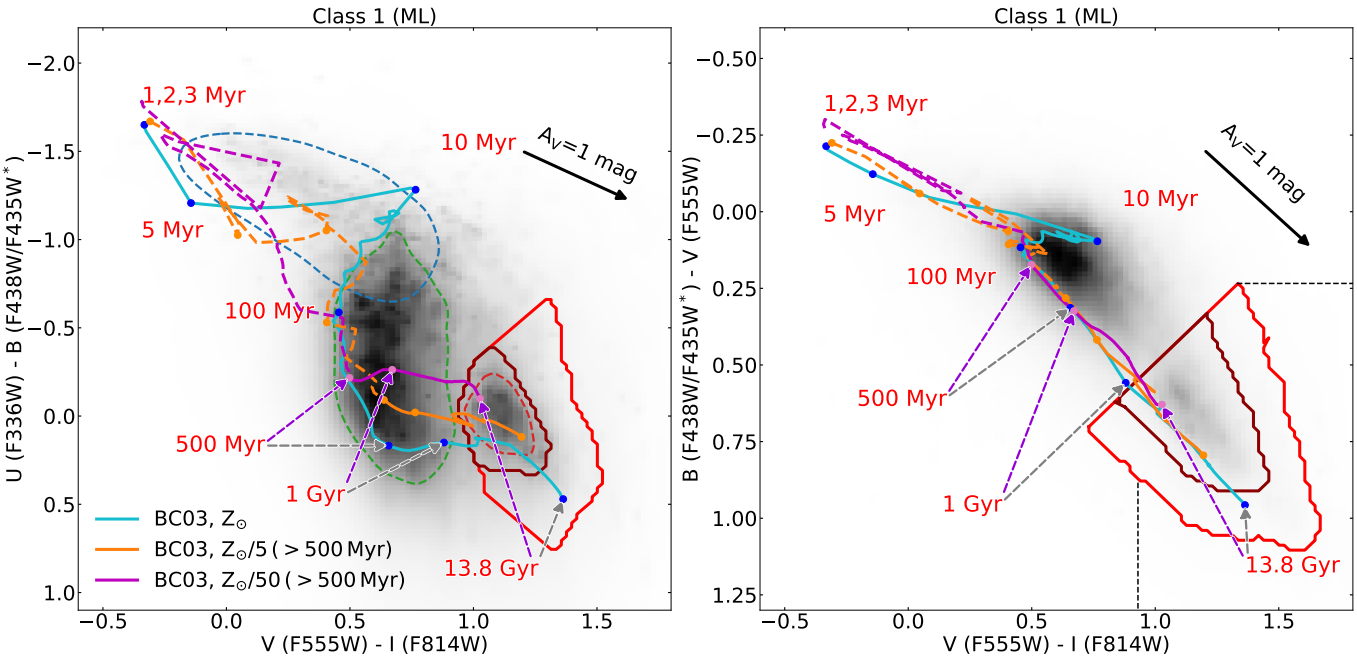

Figure 6. Polygons containing the GC clump as seen in the *UBVI* ($V-I$, $U-B$) and *BVI* ($V-I$, $B-V$) color–color diagrams. In each panel, we show the underlying color–color diagram of Class 1 clusters for all 38 PHANGS-HST galaxies, as presented in Paper I, representing each cluster with an elliptical Gaussian corresponding to its photometric uncertainties along each axis. The resulting density distribution was segmented and deblended in order to isolate the GC clump enhancement from the bulk of the younger/higher metallicity population. The GC segment was then used to generate our SED-TreeFit restrictive and inclusive OGC color–color regions (dark and medium red solid lines, respectively). Results for (left) *UBVI* color–color space, (right) *BVI* color–color space, both evaluated for ML Class 1. In the *BVI* color–color diagram, we also mark with straight lines the extension of the *BVI* color–color region added in order to provide the tolerance needed to admit the very reddest (rare) objects to the OGC branch, as they would otherwise be excluded. Such objects also must either have a nondetection/missing U measurement, have $U-B \geqslant 0.0$ if $V-I < 1.3$, or have $U-B$; $\geqslant -0.66$ if $V-I \geqslant 1.3$ to qualify as a potential OGC. On the left plot (presenting the *UBVI* color–color diagram), the blue, green, and red dashed polygons are the YCL, MAP, and OGC zones from Paper I, respectively.

branch, if there is a disagreement between the neural network and human classifications, the latter are adopted for branch assignment purposes.

The final node implements color criteria (lower red circles labeled "*UBVI* GC c-c?" and "*BVI* GC c-c?" in Figure 3), which capture the OGCC. These criteria are enforced as color–color regions determined based on the observed density distribution of machine-classified Class 1+2 objects in J. C. Lee et al. (2025, in preparation) and Paper I. The regions are shown as the red polygons in the $U-B-V-I$ (left) and $B-V-I$ (right) color–color diagrams in Figure 6. The $B-V-I$ color–color diagram is used to evaluate clusters that do not have robust U band photometry (red circle labeled "*BVI* GC c-c?" in Figure 3). There are two options for OGC qualification in each of the color spaces, a tighter, more restrictive color–color region (dark red polygon) and a larger, more inclusive zone (medium red polygon, plus all area included by the vertical/horizontal line segments in the right panel) to allow for photometric uncertainties on top of intrinsic color spread for OGCs. Experimentation during SED-TreeFit development showed that the restrictive option allowed 36%–38% fewer OGC branch objects than the inclusive color–color region (many of those missed were independently judged as viable candidate GCs, Section 5.1.2), and inspection of the OGC branch clusters selected inclusively demonstrates only minimal contamination by non-GC objects (see next section), leading us to adopt the inclusive region as default.

It is possible that intermediate-age, non-GCs could in some cases occupy dusty enough locations that they fall within our OGC color–color region. We have no means of individually identifying such contaminants with our current SED-TreeFit criteria. However, we argue that this subset of objects will be minor because the MAP and OGCC populations are clearly separated enhancements in the *UBVI* color–color diagram, as first shown by D. Maschmann et al. (2024) and illustrated by the green and red dashed polygons of Figure 6 (left panel). This separation indicates that at ages of $\log\, t\ \mathrm{yr}^{-1} \gtrsim 8$ the typical amount of reddening is insufficient to cause frequent intrusion of the OGC color–color region by intermediate-age, non-GC objects. Certainly there are some dusty contaminants, but they will not dominate the true globular population. Our best estimate of contamination (obtained by fitting two-component models to reddening-vector-aligned crosscuts of the *UBVI* color–color distribution for objects satisfying the first two OGC branch decision points) is between 5% and 10%.

In Figure 7, we provide fully independent support for our adoption of OGC color–color regions based on the Milky Way GC population. We adopted the clusters of the W. E. Harris (2010) catalog as a benchmark due to their very well-determined age, metallicity, Milky Way perspective extinction, and absolute integrated magnitude (determined from resolved color–magnitude diagrams of their stellar population or high-dispersion spectroscopic observations). For all W. E. Harris (2010) GCs having tabulated Johnson–Cousins *UBVI* photometry, we used these measurements to synthesize a predicted HST color–color distribution. Stages of this process are depicted in Figure 7, along with eventual comparison to our OGC color–color regions. We first transformed the photometry into the WFC3/UVIS system ($U\rightarrow$F336W, $B\rightarrow$F438W, $V\rightarrow$F555W, $I\rightarrow$F814W) using object-specific

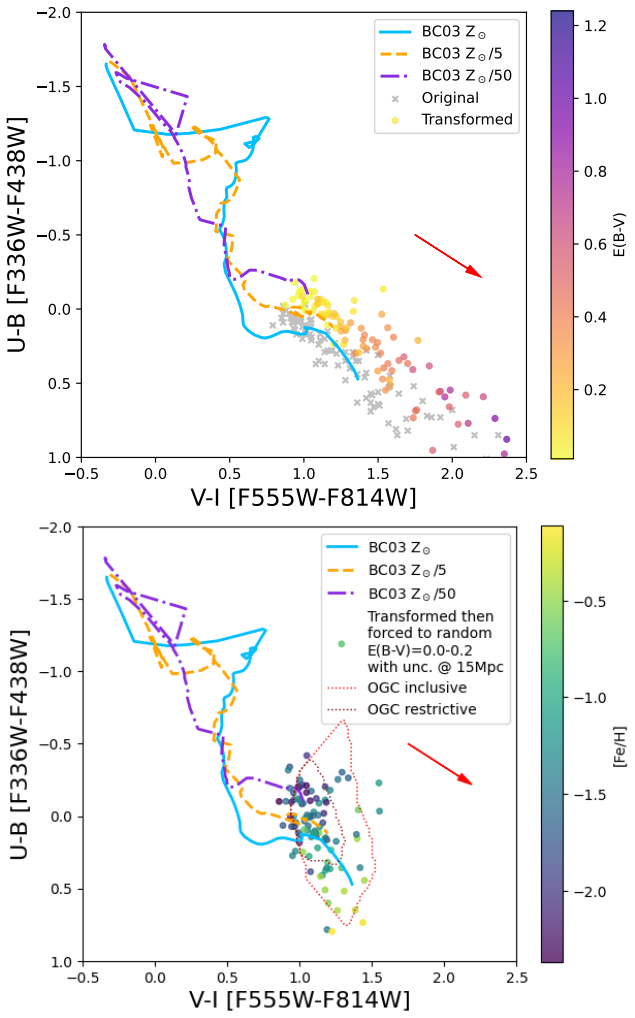

Figure 7. Color–color properties of Milky Way GCs from the compilation of W. E. Harris (2010), used as a means of validating our SED-TreeFit OGC color–color selection regions. Lines in each panel indicate BC03 tracks for $Z_{\odot}$ (cyan), $Z_{\odot}/5$ (orange), $Z_{\odot}/50$ (purple). (Top) Grey x markers show the original Johnson–Cousins photometry (U, B, V, I_c). Circles show the photometry after transformation of the $U-B$ and $V-I$ colors to the HST WFC3/UVIS system (F555W-F814W and F336W-F438W). Symbols are colored according to the tabulated Milky Way perspective $E(B-V)$ from W. E. Harris (2010). We use these $E(B-V)$ to correct the transformed photometry to intrinsic colors (not shown) before producing the bottom panel. (Bottom) The filter transformed intrinsic photometry of Milky Way GCs after rereddening to be consistent with the PHANGS-HST population of intermediate-age non-GC objects (random $E(B-V) = 0.0$–0.2 mag) with application of random photometry errors appropriate to the population as if it were observed at a distance of 15 Mpc by PHANGS-HST. Color coding in this panel indicates the known [Fe/H] from W. E. Harris (2010). The OGC color–color selection regions (restrictive: dark red, inclusive: red) are shown, and are an excellent match to the Milky Way GC population.

representative spectra to derive color terms (Figure 7 top). The HST-corrected colors were next dereddened according to the $E(B-V)$ given by W. E. Harris (2010) to obtain intrinsic (dust-free) colors (not shown). Fully dereddening the Milky Way GC shifts their distribution blueward beyond the observed PHANGS-HST OGCC. The last steps shown in Figure 7(bottom) were to reredden, allowing a randomized $E(B-V)$ value per cluster (0.0–0.2 mag) and apply photometric scatter to the Milky Way data points consistent with objects of the absolute magnitude as they would be measured by PHANGS-HST at a distance of 15 Mpc. This amount of reddening was implemented since it is consistent with typical values determined for the oldest "general grid" clusters in PHANGS-HST. See Section 5.3 and Figure 24 for details. We then added the SED-TreeFit *UBVI* OGC color–color regions to the plot for comparison. We find excellent agreement between the selection regions and the Milky Way GCs. The majority of the W. E. Harris (2010) clusters fall in the restrictive region, but a significant fraction require the inclusive region and even the extra allowance for the very reddest objects (see Figure 6). Some have $V-I$ color slightly blueward of our OGC color–color region—this is reflective of the fact that the color boundary in question was determined conservatively with respect to intermixed MAP and OGC populations in this part of the *UBVI* color–color diagram. That is, the OGC color–color region does not extend fully to the MAP population boundary in the left panel of Figure 6 in order to minimize the number of moderately reddened intermediate-aged objects being classified as belonging to the OGC population.

Color bimodality is a well-known characteristic of GCs, with redder colors linked to increasingly higher Z objects (J. P. Brodie & J. Strader 2006; W. E. Harris 2023; K. Hartman & W. E. Harris 2024), enabling a means to categorically pick between our allowed BC03 metallicity options. In Figure 8, we establish a two-color index (TCI) used for the assignment of metallicity for OGC fitting. We used the transformed, partially dereddened photometry of the Milky Way GC to constrain a best-fit line (solid black line in the upper panels of Figure 8). In practice, lines for both the *UBVI* color–color space and for the BVI color–color space are determined (for *UBVI*: $(U-B) = 1.48(V-I) - 1.66$; for *BVI*: $(B-V) = 1.15(V-I) - 0.55$). The TCI is then defined as the distance from the y-intercept location to the closest point on the line (in either space) for each cluster. TCI is a proxy for metallicity, as shown in the remaining panels of Figure 8. Calibrating expected values with respect to the spectroscopically measured [Fe/H] of W. E. Harris (2010) clusters, we find TCI threshold values that optimally separate those objects into two groups, "closer" to each of the SED-TreeFit OGC metallicity choices. These thresholds are used as follows: we adopt $Z = 0.0004$ ($Z_{\odot}/50$) if $\mathrm{TCI}_{UBVI} < 2.16$ or if $\mathrm{TCI}_{BVI} < 1.83$ (when only *BVI*-detected), otherwise $Z = 0.004$ ($Z_{\odot}/5$). Of course, varied-per-object reddening (in the PHANGS-HST OGC objects) is a concern and could cause clusters to be assigned erroneously, but the bulk of this effect is mitigated by using the $E(B-V) = 0.1$ fitted lines.

Sources which pass all nodes on the OGC branch are fit with a low metallicity ($Z = Z_{\odot}/50$ or $Z = Z_{\odot}/5$ depending on *TCI*), low-reddening ($E(B-V) \leqslant 0.2$ mag) restricted CIGALE model grid. A small amount of reddening is allowed since GCs sometimes intermix with some of the interstellar medium (ISM) of the parent galaxy, even if there is little dust within the cluster itself. In some cases, multiple-age solutions occur, even within this reduced parameter space. In these cases, we adopt the most likely PDF mode, which is frequently 13.75 Gyr.

What would have been the SED-TreeFit result if we only allowed a single OGC metallicity? In Figure 9, we illustrate the significant impact that the choice of OGC metallicity has on age and mass determination. Plots in the left column show the OGC age–mass distribution if we had fit all GC using $Z_{\odot}/50$ (top) or $Z_{\odot}/5$ (middle) exclusively, and the outcome assigning Z based on TCI per object (bottom). The right

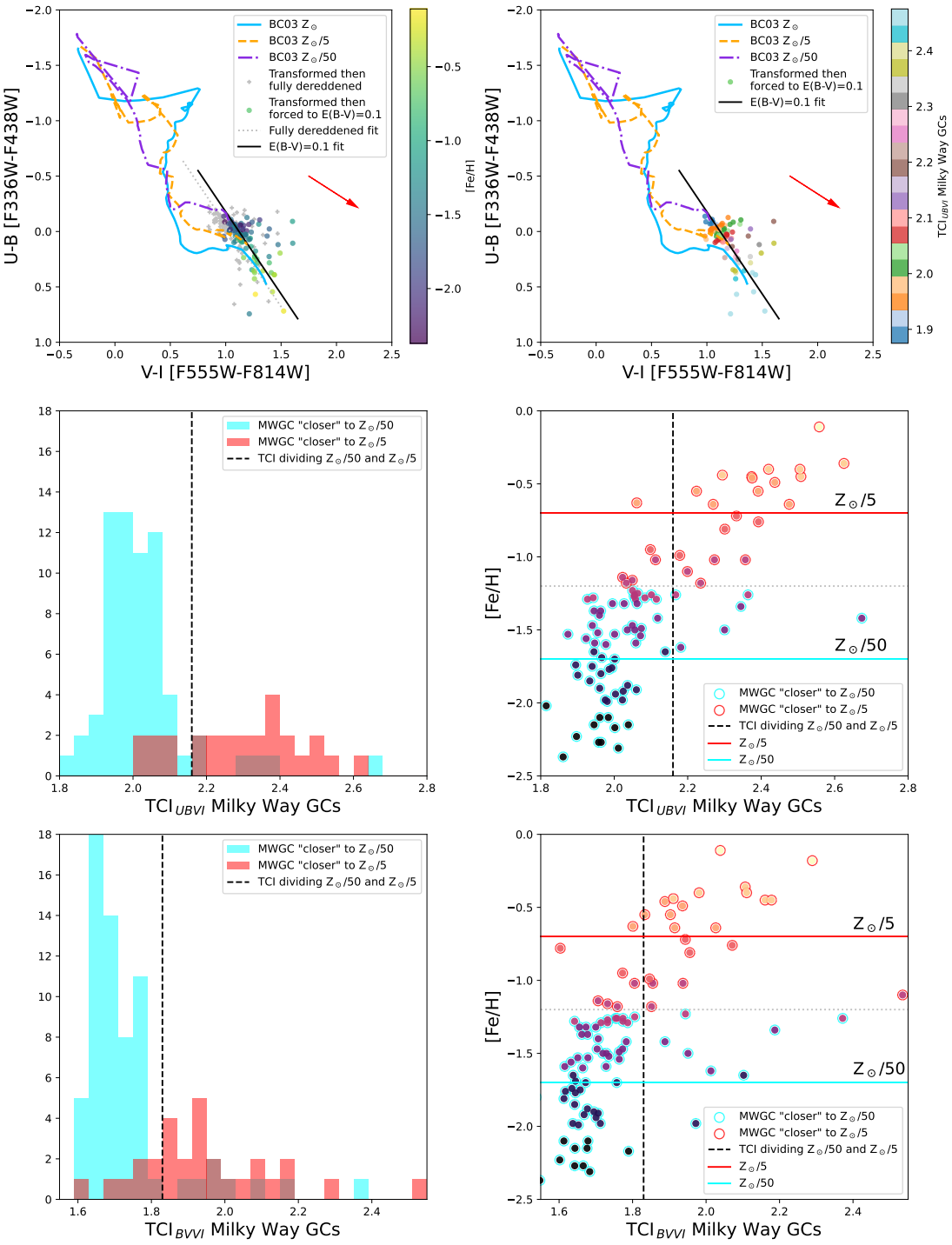

Figure 8. Illustration of our Milky Way GC-based criteria for determining which of the two SED-TreeFit "low-Z" choices should be used for PHANGS-HST objects assigned to the OGC branch. (Top left) The photometry of W. E. Harris (2010) GCs as presented in the bottom panel of Figure 7, but assuming $E(B-V) = 0.1$ and no additional noise, is then overplotted with best-fit lines to the color–color distribution. (Top right) As at left, but now color coding the points by their *UBVI* TCI (TCI_{UBVI}) computed relative to the best-fit line for Milky Way GCs slightly reddened ($E(B-V) = 0.1$) by minimal dust. (Middle left) The distribution of TCI_{UBVI} for Milky Way GCs; (cyan bins) closer to $Z_{\odot}/50$, (red bins) $Z_{\odot}/5$. The dashed vertical line indicates our chosen threshold value, most cleanly assigning clusters based on their known [Fe/H]. (Middle right) The correlation between TCI_{UBVI} and [Fe/H] for W. E. Harris (2010) clusters, with the two SED-TreeFit OGC metallicity choices marked (cyan and red horizontal lines) in addition to our TCI_{UBVI} threshold (dashed vertical line) used for the PHANGS-HST objects. The dotted gray line running horizontally is to guide the eye in terms of which Milky Way GCs are guide the eye in terms of which Milky Way GCs are alternatively closer to $Z_{\odot}/50$ or $Z_{\odot}/5$. (Bottom panels) As in the middle row, except here for TCI_{BVI}.

column zooms in to the high-mass end and includes upper and lower limits for a few exceptionally massive GCs. We see that any choice of Z produces artificial enhancements in the inferred OGC age distribution due to the specific evolutionary path of the SSP models in our filter system. The overpopulated ages vary systematically with Z, but the trend is for clusters to be dated older when forcing $Z_{\odot}/50$ rather than $Z_{\odot}/5$. A significant population of apparent OGC ages less than 1 Gyr

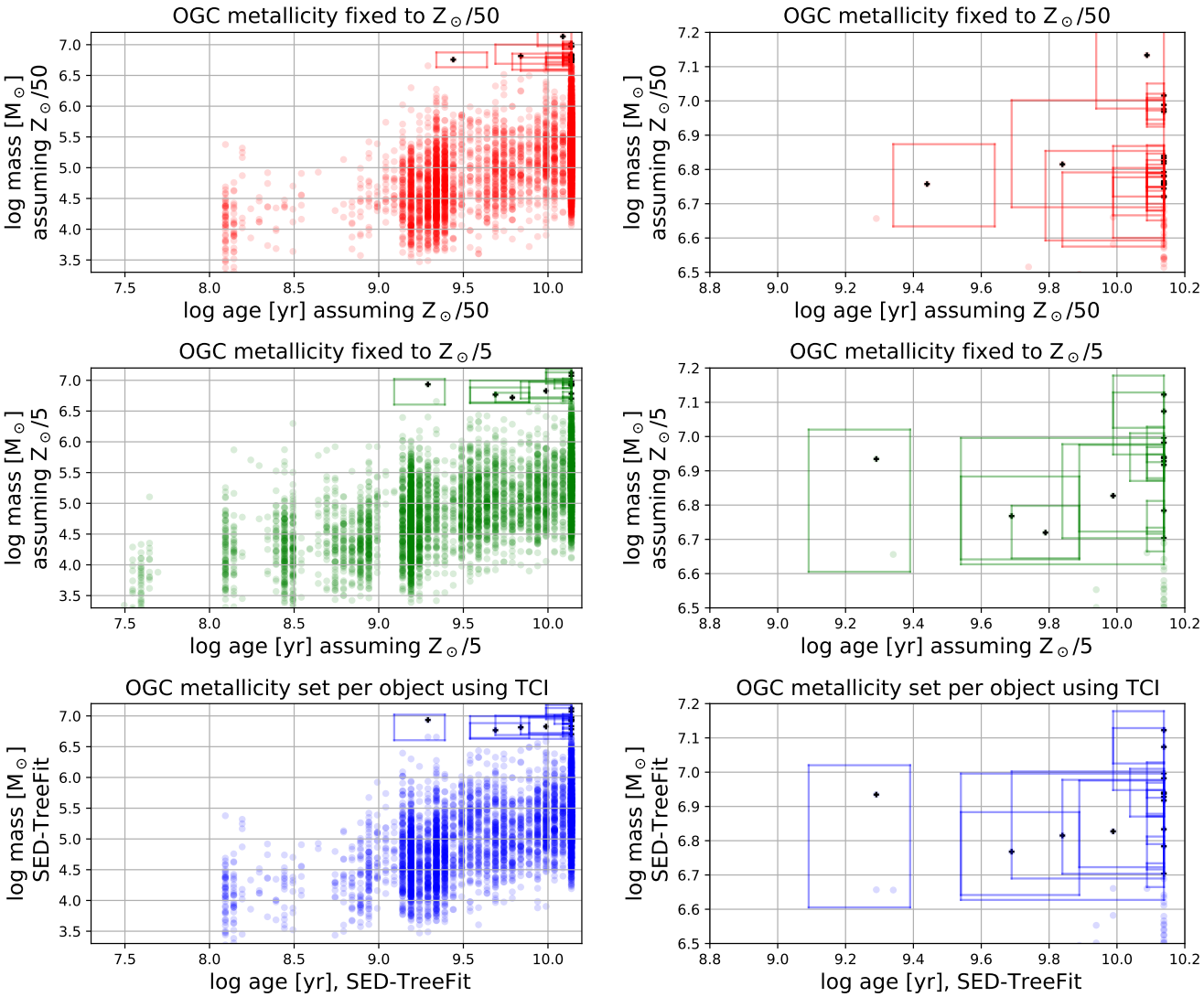

Figure 9. Age–mass diagrams for objects assigned to the OGC branch, according to three assumptions for metallicity. The plots include clusters from all 38 PHANGS-HST galaxies, as processed for the ground-based Hα SED-TreeFit analysis. Clusters with log $M_c/M_\odot \geqslant 6.7$ are marked with a black cross and a box indicating upper and lower limits for the estimated properties. The top, middle, and bottom rows are for $Z_\odot/50$, $Z_\odot/5$, and object-by-object TCI-assigned Z assumptions, respectively. The left column shows the entire distribution, whereas the right column presents a zoomed area related to the most massive OGC objects.

occurs in $Z_\odot/5$ fits, but the number of clusters assigned an age of 13.75 Gyr is inflated in $Z_\odot/50$ fits. The bottom panels show that allowing TCI-driven choice of metallicity object-by-object results in a smoother distribution of age older than ∼1.5 Gyr and less clusters assigned to either age extreme (<1 Gyr or 13.75 Gyr). The right column panels of Figure 9 demonstrate that our TCI approach induces small changes in the massive end of the GC population, but neither the low Z grid (or their combination) is responsible for the SED-TreeFit result of very high OGC masses in a small number of objects (see Section 5.2).

4.5. Reliability of YNO and OGC Branch Assignment

The scientific benefit of our SED-TreeFit method hinges on the accuracy with which we can assign sources to the YNO and OGC branches. How reliable is this operation? We show below, both with detailed visual inspection and with measurements using other non-HST PHANGS data sets, that our decision tree criteria yield correct branch assignments in the vast majority of cases. We emphasize that branch assignment often has a very significant impact on estimated age, mass, and reddening for individual objects, and the accuracy of assignment is optimized by using high-resolution HST Hα imaging for our decision tree.

Figure 10 presents (I, V, B) color cutouts for a random subset of Class 1 and 2 ML clusters drawn from the OGC and YNO branches, using branch assignments based on HST Hα imaging. Each of the OGC branch clusters was closely scrutinized by coauthor B.C.W. using an interactive viewer,[39] allowing for inspection of all bands of PHANGS-HST NUV-*U*-*B*-*V*-*I* imaging and careful control of display parameters, and following the methods described in B. C. Whitmore et al. (2023a). This includes the use of the software tool to estimate symmetry, color (using *BVI* and *UVI* images color images with various contrast levels to evaluate both the cluster and any evidence for dust in the surroundings), neighboring objects and

[39] Such interactive viewer tools are available for each galaxy in our sample at the PHANGS HLSP website (https://archive.stsci.edu/hlsp/phangs; doi:10.17909/t9-r08f-dq31) and are based on the Hubble Legacy Archive (B. C. Whitmore et al. 2016) software.

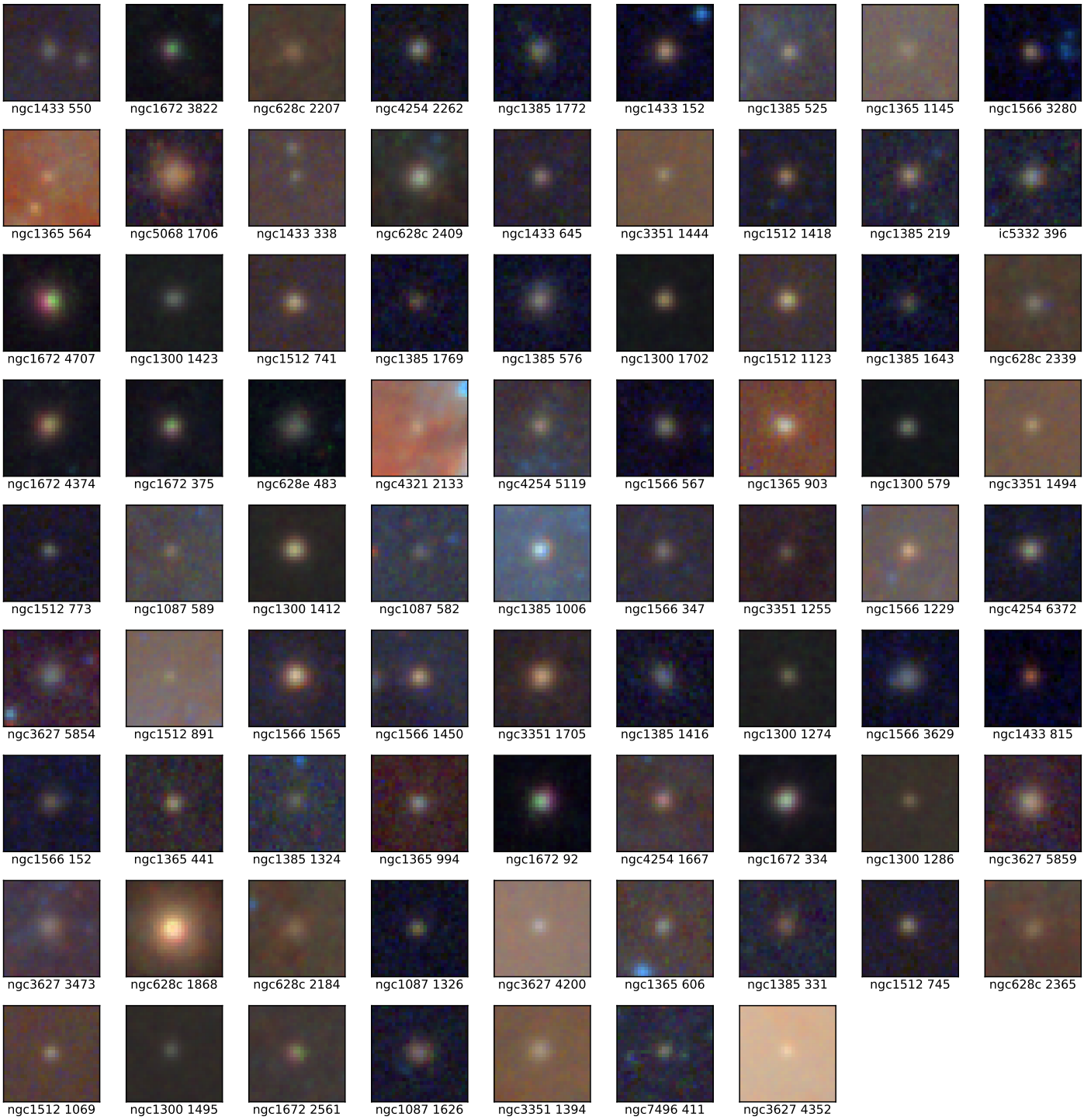

Figure 10. Random subsamples of OGC (top) and YNO (bottom) ML Class 1 and 2 objects used for branch assignment validation via visual inspection. Each cluster is displayed as a color image using (I, V, B) as (R, G, B). These cutouts were not the basis of actual validation—each cluster was interactively displayed, with access to the full suite of PHANGS-HST imaging.

degree of isolation, smoothness, and uniformity of color. In questionable cases, several other color images are also examined, including Hα, PAH bands, and higher resolution NIRCam observations (i.e., F200W). Author D.A.T. inspected each of the randomly selected YNO branch objects in our HST Hα imaging, looking for either close positional alignment of H II region peak and cluster, or clear morphological indications (an enclosing bubble or nebulosity wrapping around the cluster), as confirmation of YNO assignment. See S. Hannon et al. (2019, 2022) for a detailed analysis of HST-based H II region morphological classification.

We find that, of the random subsamples, 90% (71/79) of the OGC branch clusters and 99% (90/91) of the YNO branch clusters appear correctly processed through the decision tree when HST Hα is employed for branch assignment. Examples of likely misclassified OGCs (due to dust) include objects 2184 and 2365 in NGC 628 (i.e., in the second-to-bottom row in the top mosaic of Figure 10). When the same experiment

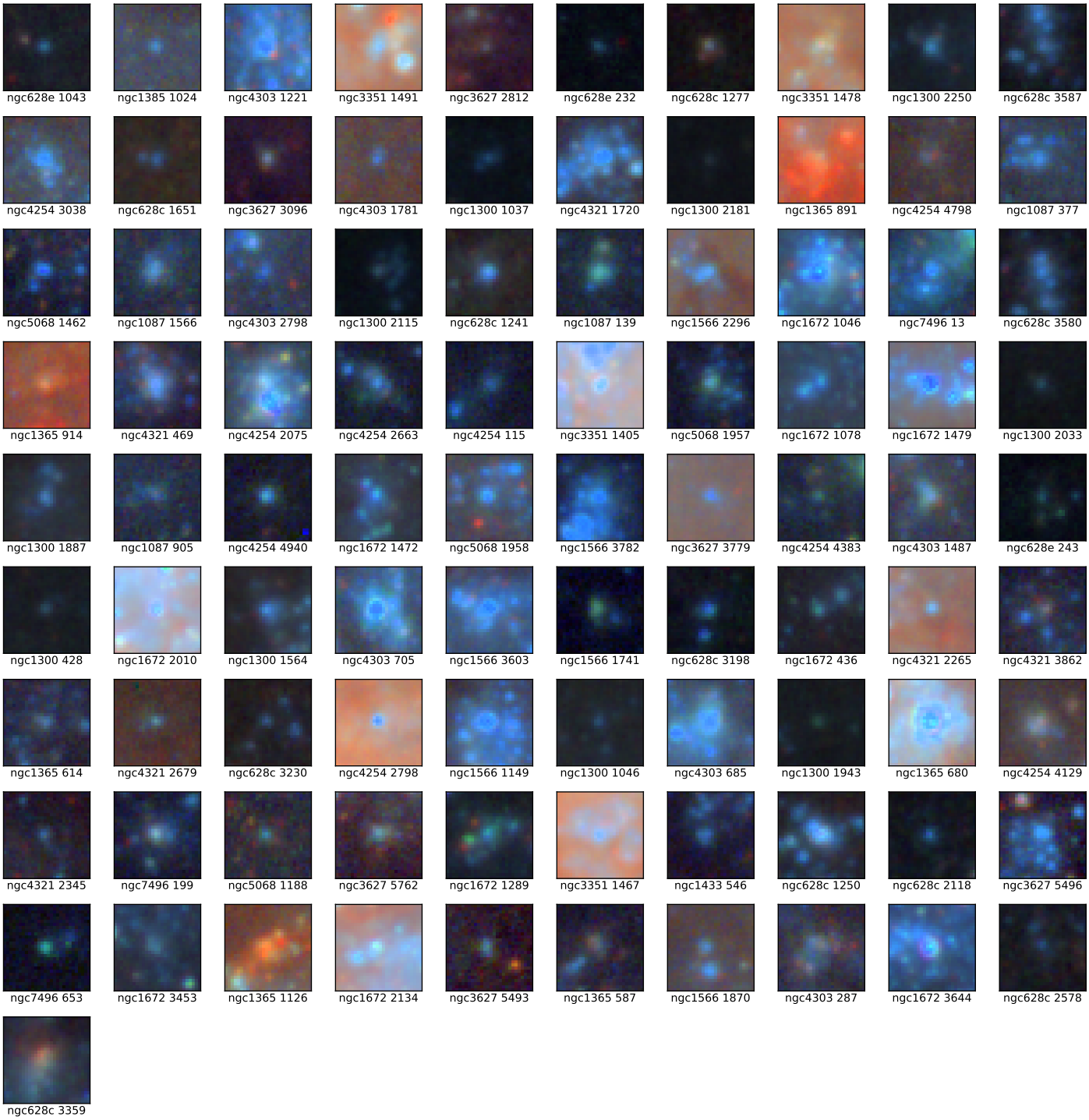

Figure 10. (Continued.)

was repeated on the basis of ground-based Hα branch assignment, the percentages dropped slightly to 85% (76/89 for OGC) and 96% (87/91 for YNO). In both contexts, our assessment can be considered representative of typical environments and their resident cluster populations in PHANGS-HST. Some of the misclassified OGCs are likely young, dusty clusters that are low mass and do not contain an ionizing star. Such objects would fail our first decision tree node (localized Hα emission), yet conceivably pass subsequent OGC branch criteria that assign them erroneously as a GC.

In addition to inspection of the randomly selected clusters in Figure 10, we undertook visual inspection for a focused subsection of NGC 3351 (in particular its star-bursting central ring) where the SED-TreeFit method modifies a much higher fraction of fitted ages.

Figure 11 shows the central region in NGC 3351 chosen as a case study. Coauthor B.C.W. assessed whether the changes in age resulting from the new SED-TreeFit procedure are likely good (green color coding), bad (red), or ambiguous (magenta). Figure 11 presents (left) the outcome according to SED-TreeFit based on ground-based Hα imaging and (right) the

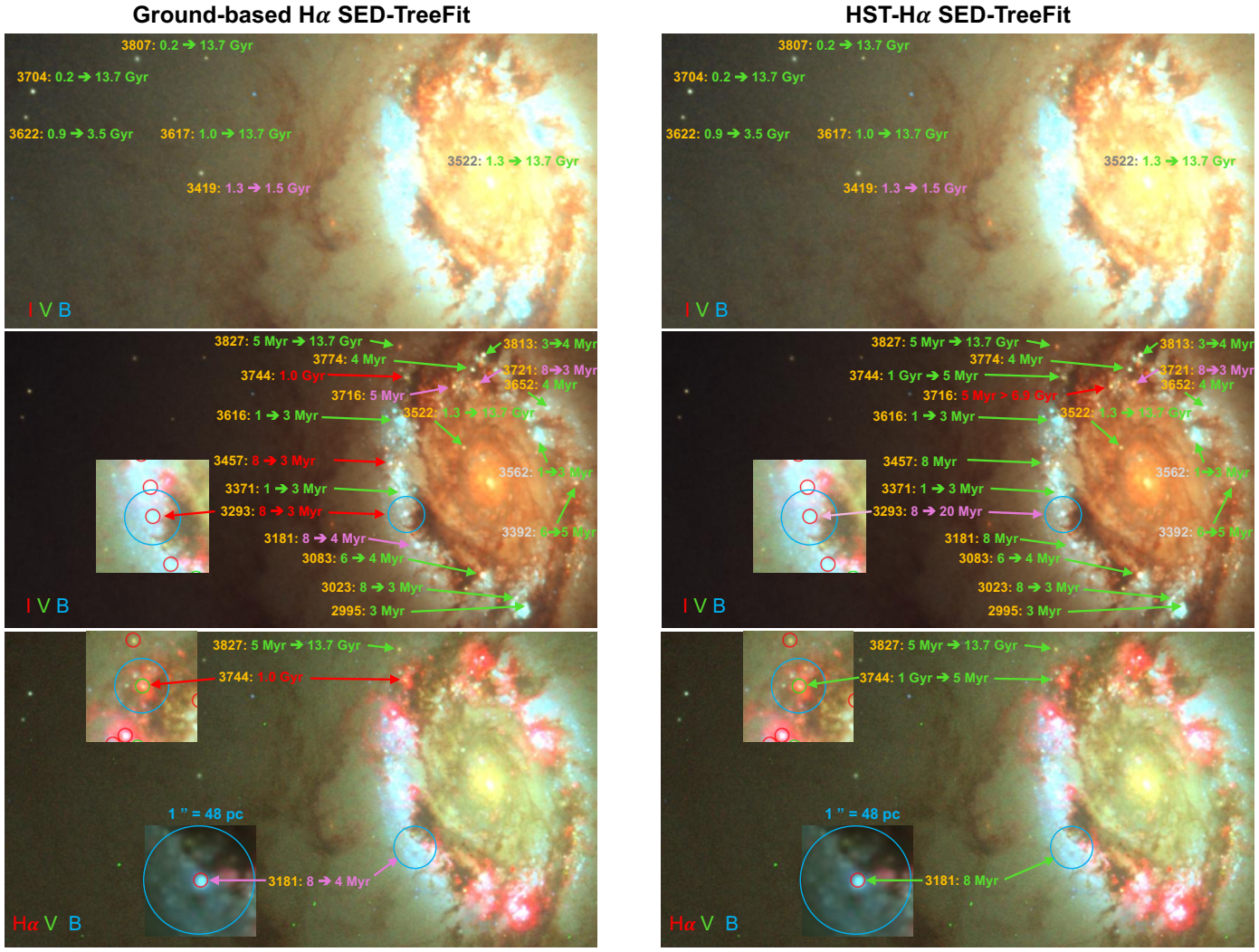

Figure 11. Region in NGC 3351 to illustrate examples of cluster ages that stay the same (one value) or change (two values) when the SED-TreeFit procedure is used. A manual examination incorporating the position in the color–color diagram, whether any nearby Hα appears to be associated with the cluster, and the presence of dust, is used to determine cases where the changes are good (green), bad (red), or ambiguous (magenta). The left panel shows the outcome when using ground-based Hα for the SED-TreeFit decisions, whereas the right panel shows the improvement from switching to HST Hα imaging for the decision tree. Only a representative set of the brighter C1 and C2 clusters is shown. In each panel, the top image uses the *BVI* filters, with a contrast to show the OGCs in the bulge most clearly; the middle plot uses the same filters but a contrast set to show the clusters in the ring most clearly; the bottom figure includes the HST Hα image in red, to show the youngest regions.

outcome of SED-TreeFit HST Hα processing. To minimize labeling confusion, only a representative set of the brighter C1 and C2 clusters is shown: the total number of clusters in the region, according to neural network classifications, is roughly twice as large. If only one age is listed for a cluster in the figure, no change was made to the age by the SED-TreeFit procedure (from the minimum χ^2 best-fit age following J. A. Turner et al. 2021). On the other hand, if a change is made, two numbers are listed; first using Turner's previous method and then the SED-TreeFit decision tree and PDF mode method.

We first note that OGCs in the top panels of Figure 11 appear to have all been reassigned a plausible age in this particular region, even cluster 3522 located near the center, although cluster 3419 is marginally too young. The ground-based and HST Hα SED-TreeFit results are identical for these objects. However, in the more crowded regions of NGC 3351's ring, some disagreement between the runs is seen. Overall, considering objects marked in the middle panel as well, we see that 70% (16/23) of the clusters appear to have unambiguous "good" ages (green) for ground-based Hα, and 83% (19/23) for HST Hα SED-TreeFit. The fraction increases to 87% (20/23; ground-based) and 96% (22/23; HST-based) if the ambiguous objects (magenta) are included as "good" ages. In this particular region, the ages are changed by the SED-TreeFit procedure for the majority of the objects (18/23 = 78% of the time) using either source for the Hα imaging. This is atypical (by intent, since we deliberately picked a complicated and active environment) as Table 3 shows that only ∼14% of ages (2012 + 5229 + 5726 = 12,967 of 36,180 + 59,610 = 95,790) across the entire 38 galaxy PHANGS-HST sample are changed due to SED-TreeFit assignment to either the YNO or OGC branches (specifically 5.6% of C1+C2 as YNO, 16% of C1 +C2 as OGC, 9% of C3 as YNO). When reliant on lower resolution ground-based Hα imaging, the SED-TreeFit YNO branch occasionally results in underestimates of the age due to

the presence of nearby Hα, which appears to be associated with a given cluster based on the ground-based image, but does not on the HST image. In the particular region shown in Figure 11 only one object (ID 3181) is clearly assigned too young an age for this reason, while two other clusters (IDs 3293 and 3721) that shifted to younger age are morphologically challenging cases (i.e., it is unclear whether the Hα is associated with the object, even with the HST image). Such cases are the exception rather than the rule. Three objects (IDs 3083, 3023, 3392) are reassigned a correct younger age by SED-TreeFit ground-based Hα analysis, as subsequently confirmed with HST (e.g., IDs 3083 and 3392 are centered on especially compact and strong Hα flux). Isolating only the 13 clusters conceivably thought to be younger than $\sim$5 Myr (green + magenta labels of 1–5 Myr, plus cluster 3716), we identify 12 as 1–5 Myr with SED-TreeFit, implying a success rate for YNO changes in this region of $\sim$92%.

We also note that there are other cases where apparently incorrect ages are given by both the prior and SED-TreeFit methods (e.g., object 3744, where a cluster has strong Hα and hence should be young, but is given an age of around 1 Gyr by both J. A. Turner et al. (2021) and ground-based Hα SED-TreeFit analysis. This object is correctly dated using HST Hα to identify it as a YNO.

In summary, while cases of YNO branch object misinterpretation are relatively rare, with a YNO success rate of 92% in the center of NGC 3351, it should be kept in mind that there are still various "failure" modes, even in the SED-TreeFit method. We return to this in Sections 4.6 and 6.

Shifting focus to old clusters, as briefly discussed above, Figure 11 includes a population of GCs in the bulge of NGC 3351, which were originally given far too young an age (due to the age–reddening degeneracy) but are given improved ages by the SED-TreeFit procedures. However, one of these (3419) was assigned an age of 1.5 Gyr, a minimal change from 1.3 Gyr and likely still not old enough. Hence, the success rate is $6/7 = 86$ % for this small sample of OGCs.

An important caveat to keep in mind for very young objects is that, at the level of few Myr differences, there are age-dating biases directly linked to: (1) the specific 1–3 Myr path of the young blue tip of the general grid BC03 track, and (2) our choices of model grid assumptions when nebular contributions are included for the case of YNOs. In the first situation, the tendency is to underestimate the ages, in particular to give them an age of 1 Myr. This is true for young low-mass, non-ionizing objects without Hα, clusters within ring-like H II regions, and even for the age-dated clusters from J. A. Turner et al. (2021) as well. This is primarily due to the fact that the 1, 2, and 3 Myr points in SED space (thus also in the color–color diagram) are almost identical—see Figure 1—but the 1 Myr point is very slightly higher (more negative $U - B$) in the *UBVI* color–color diagram, allowing it to most closely match the photometry of objects that are offset from the track in the same general direction, even if the difference between fit quality is essentially the same for 1, 2, and 3 Myr models. The second situation noted above (sensitivity to nebular model grid assumptions) has somewhat of the opposite effect, concentrating YNO branch objects at ages of $\sim$3 Myr when they are often actually younger. The effect can be clearly seen in the right-hand panel of Figure 11, with no clusters given SED-TreeFit ages of 1 or 2 Myr, six given an age of 3 Myr, four given an age of 4 Myr, and two given an age of 5 Myr. We return to discussion of both these effects later when describing "isochronal color–color diagrams" like those of Figure 13 in Section 4.6, the cluster age–mass diagram for an example galaxy featured as part of Figure 14 in Section 4.7, and in Section 6, which is devoted to reiterating caveats of SED-TreeFit catalog use.

As noted at the start of this subsection, we can also garner insight regarding the success of branch assignment by turning to other data such as the local distribution of molecular gas or dust tracing emission with respect to clusters, via PHANGS-ALMA (A. K. Leroy et al. 2021) and PHANGS-JWST (J. C. Lee et al. 2023), respectively. Note that B. C. Whitmore et al. (2023a) compared the utility of such information in a pilot study that led to the present paper, finding that Hα was the preferred indicator of youth, with the other data sets working only slightly worse. Each indicator probes a different component of the ISM, but all are closely related to star formation activity. We emphasize that ALMA- and JWST-based assessment has the advantage of being able to consider the YNO, OGC, and general branch objects in full equivalently, rather than focusing decisions on the subset of H II-linked sources. We measured the surface brightness of CO(2–1) and F770W (7.7 μm PAH) emission at the position of all objects in our cluster and compact association catalogs (Paper I). Figure 12 shows the median surface brightness of each indicator (S(CO), S(F770W), $S(\mathrm{H}\alpha)_{\mathrm{bkdgsub}}$) as a function of *UBVI* color–color location, with separate plots for YNO, general, and OGC branch objects. More attention should be given to the CO and F770W rows, as $S(\mathrm{H}\alpha)_{\mathrm{bkdgsub}}$ directly sets branch assignment, subject to cluster morphology and color–color influences, within the decision tree. In the left column, the YNO clusters show distinctly elevated molecular gas and PAH emission compared to general and OGC objects. The same plots demonstrate a trend of increasing CO/PAH intensity as a function of presumed color–color displacement along the YCL due to reddening (by about an order of magnitude from the YCL's blue tip to red tail). In the center column, we see that clusters remaining in the general branch are characterized by relatively constant median intensity (of CO and F770W) over most of the *UBVI* color–color space, and that this typical level is less than even the lower end of the range of values measured for YNO clusters. The right column of Figure 12 demonstrates that OGC branch assigned clusters characteristically have much fainter CO/PAH surface brightness than YNO clusters in the same portion of the color–color diagram, by perhaps as much as $>100\times$ in general. Conversely, we note that the median OGC measurements are only slightly less than for general branch clusters at the corresponding color–color position. This is not surprising given that both the GCs and intermediate-age solar metallicity clusters (the later dominate general branch populations) are spatially decoupled from the environment of their birth, with the slightly fainter median values for OGCs perhaps due to some significant fraction of such objects found completely outside areas of the galaxy undergoing active star formation.

4.6. Isochronal Color–Color Diagrams: Distribution in UBVI SED Space versus SED-TreeFit Age

Even though actual fitting takes place in SED space, it is instructive to visualize the color–color location of clusters given different ages by the SED-TreeFit processing. Figure 13 shows a collection of *UBVI* color–color diagrams designed for

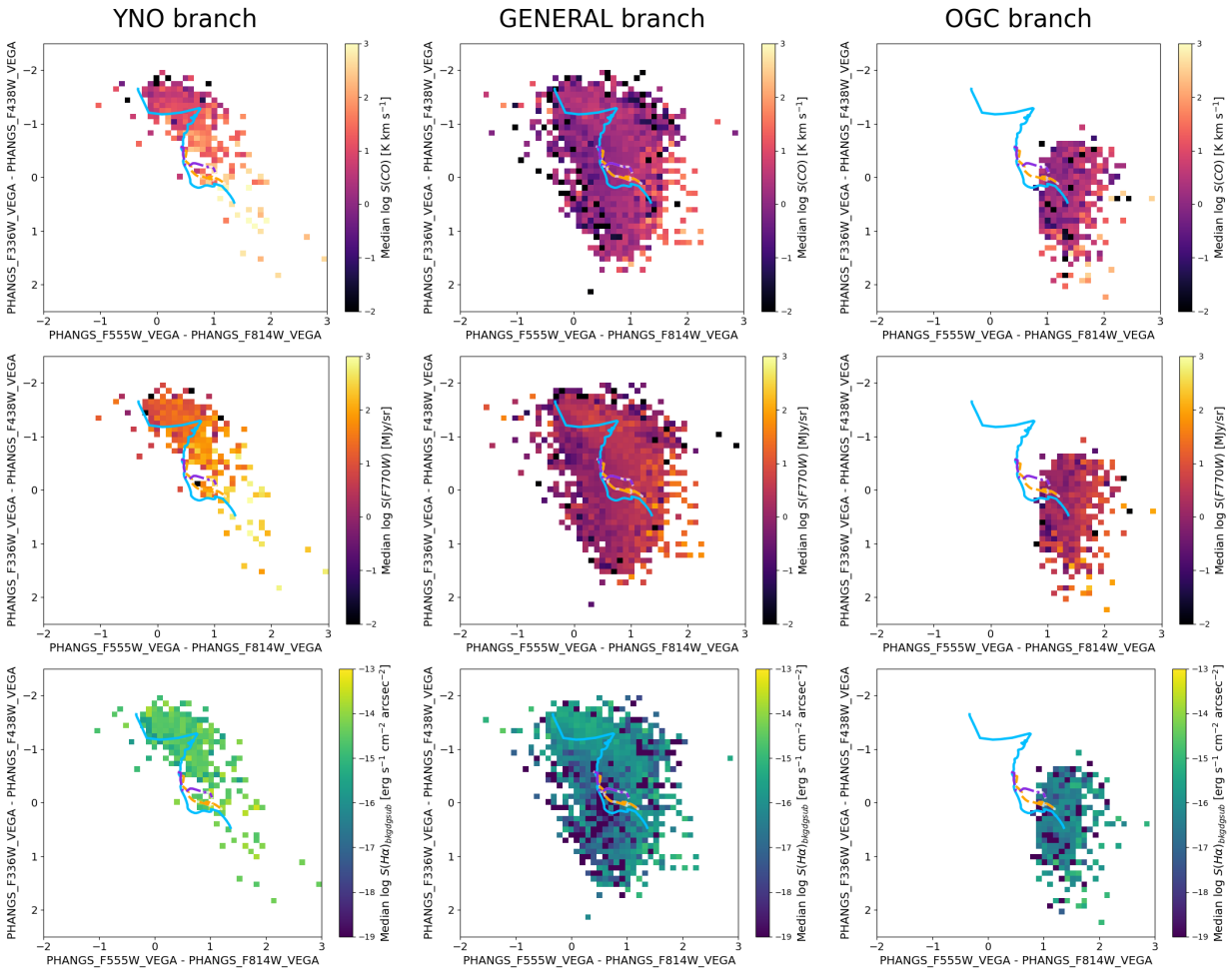

Figure 12. Binned color–color diagrams showing median (top row) log S(CO), (middle row) log S(F770W), and (bottom row) log $S(\mathrm{H}\alpha)_{\mathrm{bkgdsub}}$ for the populations belonging to the three SED-TreeFit branches: (left column) YNO; (middle column) general; (right column) OGC branch.

this purpose. Each panel in the figure shows only clusters having a specific age. We call these isochronal color–color diagrams. They help make clear the trade-offs between age and reddening being made in higher-dimensional space during SED fitting. For panels occupied by either YNO or OGC branch objects in addition to general model grid clusters (green markers), we use a different color to distinguish the YNOs (blue) and OGCs (red). With Figure 13, we illustrate various key points:

1. Parallel loci are seen at the youngest ages, oriented along the reddening vector, with one locus due to YNOs and another comprised of general grid objects. Jointly, they make up the YCL feature identified in Paper I. The offset between loci is unsurprising because "same age" objects with significant H II in the aperture are expected to have shifted color (see Figure 4). Nevertheless, the nearly exclusive division between the loci is artificial (see 2 Myr especially), owing to our specific adopted values of f_{esc} for each decision tree branch. Our expectation is that if nebular morphology could be used to estimate f_{esc} on a cluster-by-cluster basis, then revised SED fits would yield YNO + non-YNO (general grid) distributions blending continuously in the color–color diagram. As discussed in the different contexts of Sections 4.5 and 4.7, our specific choices of f_{esc} also lead to bias in the most frequently assigned ages for YNOs and their non-nebular counterparts.
2. Certain young-to-intermediate model ages (e.g., 1, 5, 10, and ∼349 Myr) clearly "sweep up" areas of color–color space when (i) the data are not a good match to anything (due to stochasticity, comparatively low signal-to-noise ratio (SNR) and/or genuine disagreement between predicted and observed SEDs) and (ii) there is a nearby elbow, or extremum, in the model tracks. One can conceptualize this as an object backtracking up the reddening vector but not hitting a solution on the track, then grabbing the nearest model point. The 1 Myr instance of this effect for general grid clusters was already noted above. Objects belonging to such groups should be carefully studied (as they have the potential to guide our understanding), but also cautiously considered if taken at face value. The 5 and 10 Myr instances are particularly apparent in Figure 13. This sweep-up effect was first shown in Figures 8 and 9 in B. C. Whitmore et al. (2020), with nearly all stochastic objects with red supergiants (RSGs) that fall in the upper right of a *UBVI* color–color diagram being given ages of 10 Myr.
3. We find an unusual population of 5 Myr, elevated $E(B-V)$ YNOs with reddening much higher than most

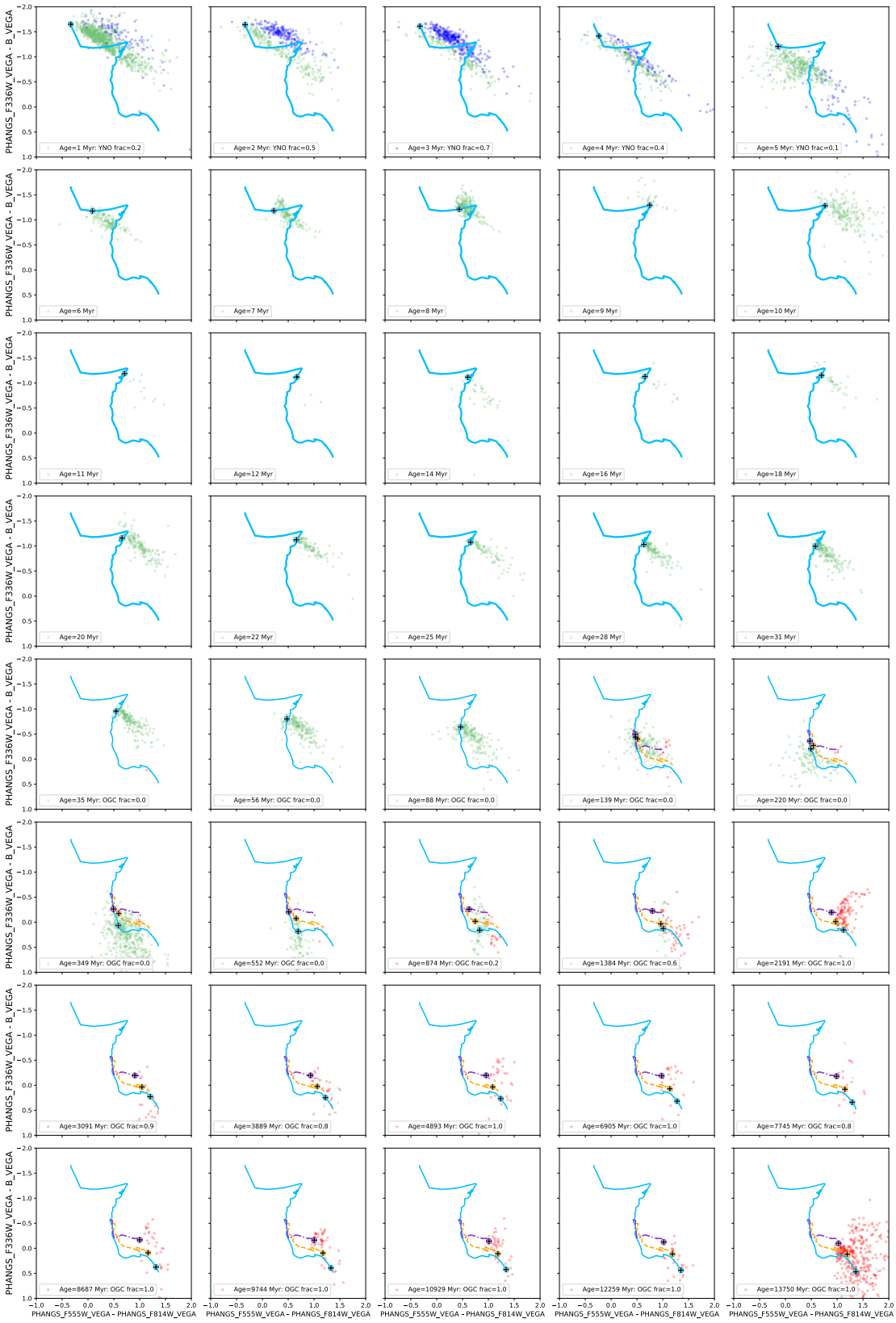

Figure 13. Isochronal color–color diagrams for clusters (ML C1+C2) with certain values of SED-TreeFit age (drawing from the adopted CIGALE choices, Table 1), showing how clusters with various ages are distributed with respect to the BC03 model tracks in the *UBVI* color–color diagram. We differentiate between objects in the general branch (green dots, all ages), the YNO branch (blue dots, age $\leqslant$5 Myr), and the OGC branch (red dots, old ages). SED-TreeFit branch assignment for this figure used HST Hα imaging, so only 17 galaxies contribute to the plot. BC03 SSP tracks for $Z_{\odot}$ and $Z_{\odot}/50$ metallicity are indicated with blue and purple lines, respectively. Small black crosses on these tracks mark the color–color position corresponding to the specific age of each panel. Cross positions for 1, 2, and 3 Myr are nearly the same, but not exactly the same (with consequences described in the text). For ages less than 35 Myr we include a panel for each CIGALE age value, afterward transitioning to only display a representative subset of older ages. We provide two animations cycling through the panels of this static figure: one for the first 100 Myr, the other for the entire age grid.

other YCs (i.e., are in the bottom-right direction of the panel). This seems like an unphysical result. Upon investigation, it appears that most of these are NGC 1365 clusters. Examination of the environment where they are found suggests the large $E(B-V)$ may be appropriate for these, but their age is probably younger in truth. This is actually a special case of the previous item; the color–color position of the young, very dusty clusters is essentially inconsistent with reddened YNO 1–4 Myr models and only partially agreeing with the 5 Myr model (see YNO appropriate predictions in Figure 4), so the objects glob onto 5 Myr as the closest match. We suspect that they may actually be cases in which the log U and n_e values we assume are substantially too low, that they are better explained by high ionization parameter, high density nebulae (log $U \sim -2$, $n_e \sim 10^3$ cm^{-3}).

4. We note that the animation of Figure 13 provides a graphic demonstration of SED-fitting behavior (relative assignment of neighboring ages) near the looping BC03 models noted in Section 3 and the resulting 10–30 Myr age gap (see Section 5.1.3).
5. The population of general branch objects shows evidence for limited cases of unfixed degenerate age solutions. This is evident due to an "extra" cluster population positioned just starting at (and redward of) an older degenerate model downstream along the reddening vector in some isochronal color–color diagrams. Another piece of evidence is that they tend to have higher $E(B-V)$ than the full range of $E(B-V)$ for YNOs of the age in question. The effect is noticeable for $t = 1$–4 Myr and possibly 6–7 Myr, but is most obvious for the 2–3 Myr panels. These problematic clusters should be given ages in the approximate range of 10–80 Myr. We confirmed that such ordinary age–reddening degeneracy "failure mode" objects have low S(F770W) despite being given solutions of high $E(B-V)$. In future revisions of the SED-TreeFit analysis, this could be remedied by removing the possibility of, e.g., 1–7 Myr with $E(B-V) \geqslant 0.5$ or 0.6 from the general pipeline grid, which is reasonable since such dusty clusters would generally also have centrally concentrated Hα (and be YNOs) if massive enough for an ionizing star(s). Ongoing work by K. F. Henny et al. (2025, Paper III) suggests that inclusion of PHANGS-JWST NIRCam photometry into CIGALE SED-fitting could potentially improve this issue in a direct manner.
6. OGC branch objects are seen at ages of $\sim$2 and $\sim$10 Gyr. They are systematically those OGC branch objects that have *UBVI* color most well matched to the (unreddened) old end of the $Z_\odot/50$ track (particularly the $\sim$10 Gyr subset). Minute differences in measured SED shape distribute objects among the OGC-relevant models. The $\sim$2 Gyr OGC branch objects have systematically brighter F275W at fixed F555W, versus the $\sim$10 Gyr and $\sim$13.75 Gyr cases. This, plus similarity with the color–color distribution of slightly younger/older general branch clusters, suggests that the $\sim$2 Gyr OGC branch population may have higher than normal contamination from non-GCs. The OGCs branch objects given an age of 13.75 Gyr are redder, and counter-intuitively shift in the direction of the old end of the $Z_\odot$ track in a manner ascribed to reddening. The predominance of 13.75 Gyr ages given to clusters assigned to the OGC branch is also a bias owing to the precise terminus of the $Z_\odot/50$ track with respect to the photometry, in a manner analogous to the artificial 1 Myr general grid population enhancement. This effect is exacerbated by our single choice of $Z_\odot/50$ rather than also permitting $Z_\odot/5$ for GCs and will be addressed in the future (see Section 6.2). Lastly, we note that GCs given an age of 13.75 Gyr should not have their age (equal to the age of the Universe) interpreted in an exact sense, but rather that they have SEDs consistent with the oldest of our $Z_\odot/50$ models and a small amount of dust. Clearly, they were not formed immediately after the Big Bang. At these large ages, the predicted SEDs for low Z clusters are very similar, so the age could equally well be several Gyr younger than 13.75 Gyr; this is reflected in our lower limits for these object ages. The median lower limit age for OGCs given 13.75 Gyr age is about 8–9 Gyr, with some reaching $\sim$ 2 Gyr. We retain the 13.75 Gyr ages in our catalog for purposes of retaining a precise link to the CIGALE model grid.

4.7. Demonstration of Method for One Galaxy

In Figure 14, we illustrate the results of applying our SED-TreeFit pipeline to NGC 4321. The top panels show color–color diagrams of all human and ML Class 1+2 clusters, highlighting those considered YNOs (blue) or OGCs ($Z_\odot/5$ OGCs (fuchsia), $Z_\odot/50$ OGCs (red)) based on our decision tree algorithm. General branch objects are shown in gray. While, in general, the YNOs nicely trace the YCL in the color–color diagram, some are beyond the region unambiguously occupied by YCs. That is, these more extreme YNOs are found at colors redder than (down and to the right of) the portion of the BC03 model track between 5 and 10 Myr. Similarly, a handful of GCs are outside of the individual OGC regions, because they can be selected using either color–color plane.

In the second set of panels, we see that the YNOs closely follow the spiral arms and star-forming ring, whereas the OGCs are much more evenly distributed throughout the galaxy, including a central concentration which may be associated with the bulge. As shown in Paper I, in some galaxies, this difference in spatial distributions is even more distinct. The right-hand panel, which is color coded by integrated CO(2–1) intensity, demonstrates the strong spatial correlation between the YNOs and bright CO intensity, again consistent with their youth. Indeed, Paper I showed that the population in the YCL was coincident with CO twice as often as objects of the MAP or OGCC, and reflected the structure of the ISM from which they were born.

Age–reddening diagrams are shown in the third set of panels, before (left) and after (right) applying our SED-TreeFit procedure. Before our new categorical prior strategy, very few GCs had correct ages, with nearly all of the red points originally assigned ages younger than 1 Gyr and a number younger than 10 Myr with high reddening (third row, left panel). After our procedure, essentially all have ages older than 1 Gyr, and the majority have ages closer to 10 Gyr. For YNOs, most previously had an artificially enhanced best-fit age of 1 Myr (as discussed in Section 4.5), although some sources associated with Hα were fit with ages >5–6 Myr originally. This has been partially improved for the YNOs with the inclusion of nebular contributions in the model library.

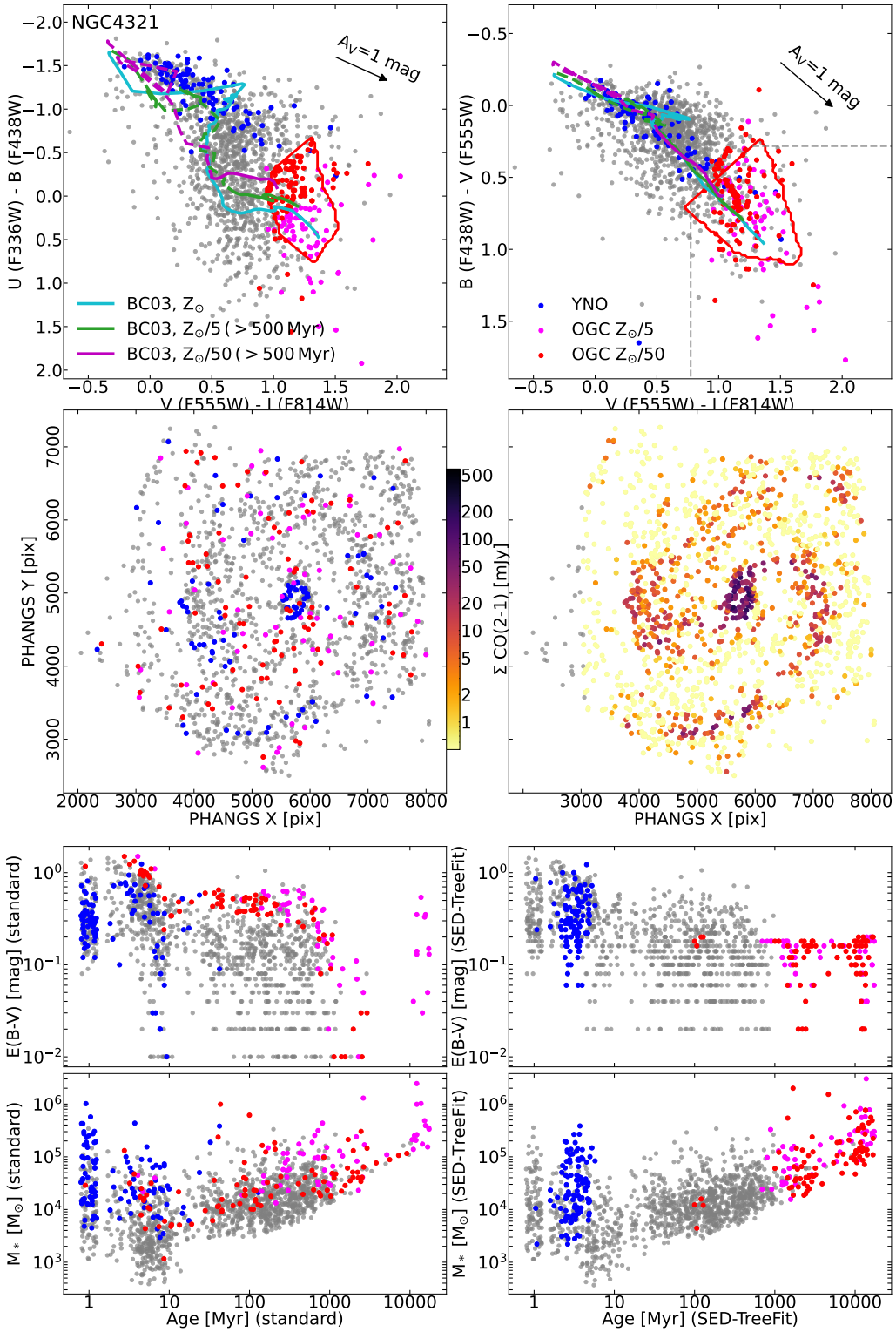

Figure 14. Plots demonstrating application of the SED-TreeFit method to NGC 4321. (Top left) *UBVI* color–color diagram showing YNOs (blue), $Z_\odot/5$ OGCs (fuchsia), and $Z_\odot/50$ OGCs (red), in comparison to all other Class 1 and 2 clusters in gray. We indicate the OGC color–color region and BC03 Solar metallicity track. (Top right) The same, but for *BVI*. (Second row left) Spatial distribution with the identical color coding as before. Second row right) Spatial distribution with points colored according to the ALMA CO(2–1) integrated intensity with strict masking. (Third row left) Age–$E(B-V)$ diagram before any changes were made to the pipeline product. (Third row right) Age–$E(B-V)$ diagram after SED-TreeFit processing was completed. (Bottom left) Age–mass diagram before changes. (Bottom right) Age–mass diagram after SED-TreeFit analysis. Note that in the last four panels, the ages have been slightly scattered to increase visibility.

The age–mass plot in the bottom-right panel of Figure 14 shows that the OGCs have been concentrated at ≈10–13.7 Gyr, with some a few times younger, and the YNO population at 2–4 Myr, appropriate (but not completely as it should be) for ionizing clusters. That is, the precise age distribution for YNOs is linked to our choice of $f_{\rm esc} = 0.5$ and

Table 2
PHANGS Star Cluster and Compact Association Catalog Contents: Physical Properties

Column Name	Unit	Description
INDEX	int	Running index from 1 to N for each individual target.
ID_PHANGS_CLUSTER	int	PHANGS cluster ID for each individual object classified as class 1, 2, or 3, ordered by increasing Y-pixel coordinate.
ID_PHANGS_CANDIDATE	int	ID in the PHANGS-HST candidate catalog for each individual target, for cross identification.
ID_PHANGS_ALLSOURCES	int	ID in the initial PHANGS-HST "all-source" detection catalog for each individual target, for cross identification.
PHANGS_X	pix	X coordinates on HST X-pixel grid (0...$n-1$). Scale = 0.03962 arcsec pixel^{-1}.
PHANGS_Y	pix	Y coordinates on HST Y-pixel grid (0...$n-1$). Scale = 0.03962 arcsec pixel^{-1}.
PHANGS_RA	deg	J2000 Right ascension, ICRS frame, calibrated against selected Gaia sources.
PHANGS_DEC	deg	J2000 decl., ICRS frame, calibrated against selected Gaia sources.
PHANGS_DM	mag	Distance modulus of the host galaxy used for SED-TreeFit analysis.
PHANGS_DMPC	Mpc	Distance of the host galaxy used for SED-TreeFit analysis.
PHANGS_DERR	Mpc	Uncertainty on distance.
PHANGS_GALAXY	str	Name of host galaxy or specific target field.
PHANGS_SED_AGE	Myr	Age corresponding to SED-TreeFit analysis.
PHANGS_SED_EBV	mag	Reddening $E(B-V)$ corresponding to SED-TreeFit analysis.
PHANGS_SED_MASS	$M_\odot$	Stellar mass corresponding to SED-TreeFit analysis.
PHANGS_SED_AGE_LIMLO	Myr	Lower limit on age corresponding to SED-TreeFit analysis.
PHANGS_SED_EBV_LIMLO	mag	Lower limit on reddening $E(B-V)$ corresponding to SED-TreeFit analysis.
PHANGS_SED_MASS_LIMLO	$M_\odot$	Lower limit on stellar mass corresponding to SED-TreeFit analysis.
PHANGS_SED_AGE_LIMHI	Myr	Upper limit on age corresponding to SED-TreeFit analysis.
PHANGS_SED_EBV_LIMHI	mag	Upper limit on reddening $E(B-V)$ corresponding to SED-TreeFit analysis.
PHANGS_SED_MASS_LIMHI	$M_\odot$	Upper limit on stellar mass corresponding to SED-TreeFit analysis.
PHANGS_YNO_GRID_FLAG	bool	Boolean flag indicating if the object was assigned to the YNO branch.
PHANGS_OGC_GRID_FLAG	bool	Boolean flag indicating if the object was assigned to the OGC branch.
PHANGS_GENERAL_GRID_FLAG	bool	Boolean flag indicating if the object was assigned to the General pipeline branch.
PHANGS_HIGH_EBV_GRID_FLAG	bool	Boolean flag indicating if the object was fit specifically allowing for higher $E(B-V)$.
PHANGS_HALPHA_EVAL_FLAG	bool	Boolean flag indicating if the object could be evaluated for localized Hα emission.
PHANGS_GLOBULAR_FLOYD24	bool	Boolean flag for objects that have been selected as GCs in M. Floyd et al. (2024).

Note. SED-TreeFit physical parameters are only provided if there are four or more bands available as detections (or three and associated Hα emission), otherwise, the related columns are blanked to a value of −999.

would vary ±1 Myr for other plausible values (older if we instead assumed $f_{\rm esc} = 0.25$, younger if we adopted $f_{\rm esc} = 0.75$). The population of non-YNO but-still-very-young objects are quite frequently given an age of 1 Myr, owing to the SEDs of 1, 2, and 3 Myr being highly degenerate in the case of no nebular emission (Figure 1) with the 1 Myr model marginally bluer in $U-B$/redder in $V-I$ than 2 and 3 Myr, allowing for it to "sweep up" as described in Section 4.6.

4.8. SED-TreeFit Catalog Contents and Uncertainty of Physical Parameters

The physical properties of star clusters and compact associations identified via our census of the PHANGS-HST 38 galaxy sample are provided as part of PHANGS-HST Data Release 4/Catalog Release 3 (DR4/CR3) hosted at MAST.[40] The corresponding observed quantities (photometry, morphological classification) are provided in companion catalogs[41] from DR3/CR2. Following the convention utilized for the companion observational catalog release, we provide four distinct SED-TreeFit catalogs using ground-based Hα per galaxy: Human C1+C2, ML C1+C2, Human C3, and ML C3. For targets having HST Hα imaging already, we provide an analogous set of four catalogs.

All sources with available SED constraints from at least three bands are processed via our SED-TreeFit decision tree analysis, but we only release physical parameters for the subset of sources having detections in four or five bands in the observed catalogs (Paper I). This decision is implemented by requiring (PHANGS_NON_DETECTION_FLAG + PHANGS_NO_COVERAGE_FLAG < 2) in order to publish SED-TreeFit outcomes; otherwise, blanking the SED-TreeFit columns with −999. An exception is made for any sources having three detections and linkage to localized Hα emission as described in Appendix B (i.e., Hα emission counts as a detection). All figures and tables in the remainder of this paper use only the sources allowed in this manner. Note that we do not remove sources from the catalogs when they are blanked with respect to the SED-TreeFit results, so that they may be further investigated in the future (e.g., with JWST for very red sources, since often it is the blue bands that are not available).

The quantities provided in the DR4/CR3 physical parameter catalogs include:

1. persistent IDs to facilitate cross identification between catalogs, and positional information (object IDs, R.A., decl., image x, y);
2. SED-TreeFit physical parameter information (flags indicating assigned SED-TreeFit branch; SED-TreeFit age, mass, $E(B-V)$, and upper/lower limits for each physical parameter);

[40] https://archive.stsci.edu/hlsp/phangs/phangs-cat; doi:10.17909/jray-9798

[41] Our independent release of observed and interpreted quantities was motivated by the expectation that the physical quantities may continue to evolve, in particular with the addition of JWST photometry, while the observed properties (from HST) will remain fixed.

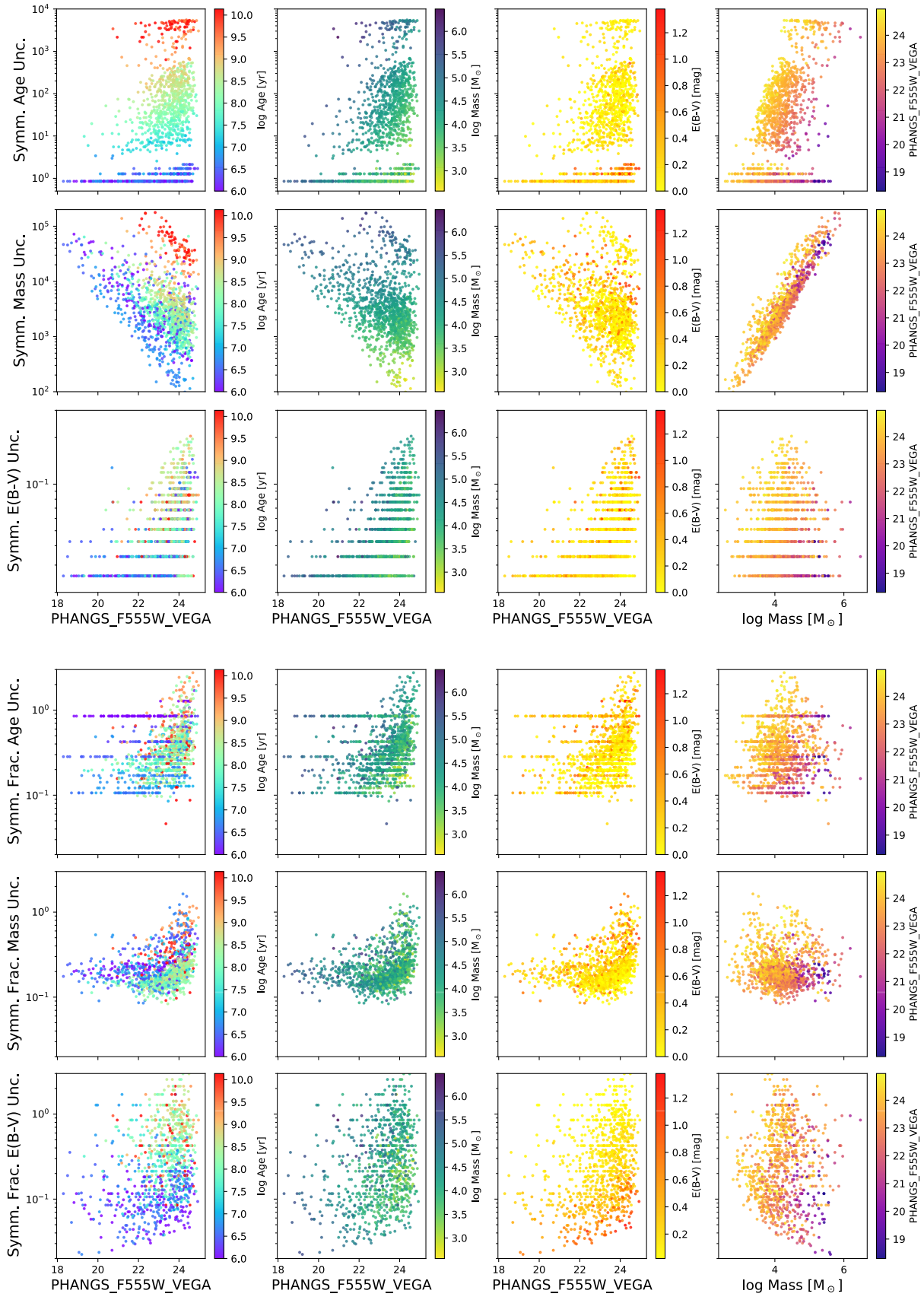

Figure 15. Symmetrized statistical uncertainty of physical parameters vs. PHANGS_F555W_VEGA (first three columns) and log M_c (fourth column) in PHANGS-HST galaxy NGC 4321, which is near the median distance of our sample. The top panel presents uncertainty in absolute terms, and the bottom panel shows fractional uncertainty. Rows are for age, mass, and $E(B-V)$ determinations (from top to bottom), respectively. Points are color coded as indicated by the color bars pertaining to each column. The values shown result from the HST Hα SED-TreeFit processing.

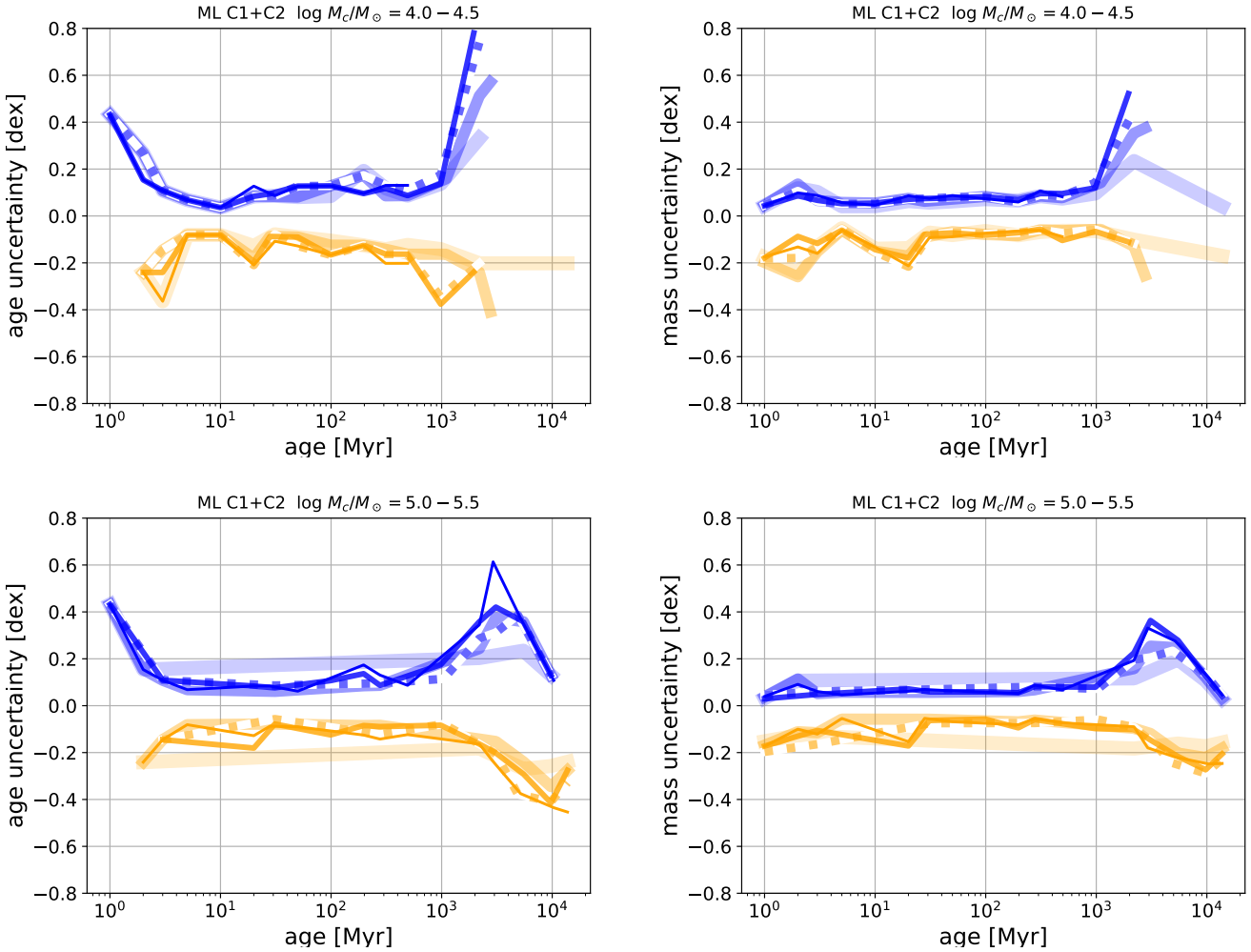

Figure 16. Median age and mass 1σ uncertainty as a function of age for ML Class 1+2 clusters, evaluated for five ranges in galaxy distance and two intervals of cluster mass (log $M_c/M_\odot = 4.0$–4.5 (top) and 5.0–5.5 (bottom)). Blue lines indicate deviation to higher values, whereas gold lines indicate deviation to lower values. In each panel, the line thickness and transparency indicate the particular quintile of galaxy distance plotted (wider and more transparent means higher distance). The dotted line indicates the central quintile outcome described in the text. Note that truly ancient clusters are only fairly represented in the more massive interval shown in the bottom row.

3. adopted PHANGS-HST distance and distance uncertainty (G. S. Anand et al. 2021; J. C. Lee et al. 2022).

A listing of these quantities is provided in Table 2, while a full description can be found in the documentation accompanying the DR4/CR3 release at MAST.

We conclude this section with a series of plots in Figures 15 and 16 intended to illustrate the level of uncertainty for our SED-TreeFit estimated physical parameters. The plots of Figure 15 show the approximate uncertainty of each parameter estimate, in both an absolute and fractional sense, versus F555W (V-band) magnitude and log(M_c). Because our method of determining upper and lower limits to SED-TreeFit physical parameters accounts for covariance and nonlinear behavior between age and $E(B-V)$, as described in Appendix A (Figure 29), the upper and lower limits are generally not symmetric (see Figure 30 in Appendix A) about the parameter value. Therefore, for readers wanting a more traditional measure, we define a quantity akin to a 1σ uncertainty by taking the difference of the upper limit minus the lower limit and dividing by 2.35 to obtain an equivalent symmetrized standard deviation. The factor of 2.35 is appropriate since, as described in Appendix A, our limits correspond to the 50%-of-peak-likelihood model space (e.g., FWHM). This symmetrized standard deviation is adopted as our uncertainty (statistical only, and in absolute units: top panel of Figure 15), then used to calculate the fractional uncertainties (bottom panel) in the figure. It is important to realize that such values are a lower limit to the true uncertainty, as our estimate does not account for systematic uncertainty linked to the assumptions made for CIGALE model parameters, overall accuracy of the cluster evolutionary tracks, and SED-TreeFit methodology-related choices, such as many of the details listed in Table 1.

Figure 16 condenses the detailed view of uncertainties in Figure 15 into a simpler takeaway presentation of the key trends. As our main focus in this paper is age improvement, we considered subsets of clusters (ML C1 and C2 only) belonging to 18 age bins spanning the entire range. Because uncertainties may depend on distance to the target galaxy, we evaluated them for five bins corresponding to the quintiles of distance in our 38 galaxy PHANGS-HST sample. Two cluster mass ranges, $M_c = 1$–$3 \times 10^4\,M_\odot$ and 1–$3 \times 10^5\,M_\odot$, were considered. See the results depicted in Figure 16.

Not surprisingly, the median age uncertainty in a bin depends on the object's age. For the central distance quintile and common

cluster masses (14.9–16.2 Mpc, M_c = 1–3 × $10^4 M_\odot$—dotted line in top panels of Figure 16), we find:

1. Very young clusters (VYCs; $t \lesssim 3$ Myr) have 1σ age uncertainty +(0.1–0.4) dex and −(0.0–0.2) dex.
2. From several Myr to several hundred Myr, age uncertainty increases slightly from a minimum of 0.05 dex to a maximum of 0.15 dex (scattered both higher and lower).
3. Clusters older than 1 Gyr have the largest age uncertainty, +(0.4–0.7) dex and ≈−0.2 dex.

In this distance range, mass uncertainty has a similar dependency on age:

1. Clusters with $t \lesssim 3$ Myr have 1σ mass uncertainty +(0.05–0.1) dex and −(0.15–0.2) dex.
2. In the several Myr to several hundred Myr age range, mass uncertainty is +(0.05–0.1) dex and ≈−0.1 dex (somewhat more for 10–20 Myr).
3. Clusters with age ⩾1 Gyr have estimated mass uncertainty of +(0.15–0.4) dex and −(0.05–0.3) dex, with the uncertainty rising to older ages.

Among the cluster subsamples analyzed here, increasing distance has little (if any) influence on the median age and mass uncertainties. In Figure 16, the thickness and transparency of the line indicate distance. We expected a dependence since intrinsically equivalent objects will be fainter, but it seems the available clusters in higher distance bins were slightly more massive, counteracting this effect in our plots.

The trends described above are largely due to the SED shape becoming nearly constant for the youngest and oldest portions of our model tracks, with additional variation attributable to age–reddening degeneracy caused by the complexity of the evolutionary tracks.

5. Results

The uniformity of PHANGS-HST imaging, and of our object identification, photometry, and SED-fitting methods, enables particularly robust analysis of physical properties (age, mass, reddening) for clusters and compact associations. In this section, we provide a high-level description of these properties in all 38 galaxies, but leave more detailed analysis to future topically focused studies. We present three key diagnostics: (1) the age–mass diagram, (2) the globular cluster mass function (GCMF), and (3) the age–reddening diagram. For each diagnostic, we highlight differences between results from previous SED-fitting (J. A. Turner et al. 2021) and from the SED-TreeFit decision tree-based methodology. Lastly, we explore the dependence of the cluster population in age–mass space with respect to galaxy evolutionary state as quantified by SFR offsets (ΔMS) from the star-forming galaxy main sequence (MS), analogous to the analysis based on color–color diagrams in Paper I.

We emphasize to readers principally interested in the physical properties of GCs that from the start our study was not intended to firmly constrain the estimated age or mass of GCs in a rigorous manner, but rather to improve our characterization of young-to-intermediate-age cluster populations by eliminating contamination from misinterpreted GCs as cleanly as possible given the current observational data and models. Although the properties of GCs identified by our work are acceptable to first order (and far better than if we had not included an OGC SED-TreeFit branch), they should be considered in light of this cautionary statement.

5.1. Age–Mass Diagrams and YMC/OGC Populations

The broad-brush star formation histories of galaxies can be inferred from the color–color diagrams of their star clusters and the relative demographic strength of the YCL, MAP, and the OGC populations (D. Maschmann et al. 2024, Paper I; J. C. Lee et al. 2025, in preparation). A key strength of color–color diagrams for clusters and compact associations is that they are a purely observational metric of galaxy evolution. However, cluster colors alone do not provide quantitative determinations of age and mass, which are required to gain insight into issues like cluster disruption timescales, the possibility of mass function cutoffs, the evolution of reddening with age, and other related topics.

5.1.1. Aggregate SED-TreeFit-based Age–Mass Diagram

A key theme of this section is to study how the new SED-TreeFit ages affect our interpretation of the cluster population. In Figure 17 (top) we present the aggregate age–mass distribution for Class 1+2 clusters from the ML catalogs after our improved SED fitting in all 38 PHANGS-HST galaxies (hence using ground-based Hα for the decision tree), and track the number of changes for GCs and YCs. Rather than plotting individual clusters as discrete points in a scatter plot, we construct an image of cluster number density by representing each object as a 2D Gaussian sized to match its age/mass uncertainty. Each galaxy includes clusters to a different magnitude cutoff dictated by its distance, internal structure (e.g., dust, confusion), and specifics of the data. A luminosity limit of $M_V = -7.5$ mag translated to the age–mass plane is shown as the teal dashed curve, and is appropriate for the NGC 4654 and NGC 2775 cluster catalogs (two of the least sensitive in the galaxy sample, both at $d > 20$ Mpc; see Figure 20). This curve is computed assuming an evolving mass-to-light ratio based on the CIGALE SSP models of our general grid; it demonstrates how clusters fade as they age, and the decrease in completeness for older, lower mass clusters.

Figure 17 shows a significant redistribution of clusters in the age–mass diagram for our SED-TreeFit results compared with those when using the earlier method. The mass-limited counts of YCs with $M_c \geqslant 5 \times 10^4\, M_\odot$ and of GCs with $M_c \geqslant 10^5\, M_\odot$, which move between the different age–mass regions, are indicated in the top panel. The percentage of total GCs in our SED-TreeFit catalog attributed to revision of age, mass is quite high (93%), whereas the analogous percentage of previously mis-fit YCs is moderate (24%). SED-TreeFit analysis also significantly alters the population of intermediate-age clusters, because the vast majority of flux into [or out of] YC and GC categories is taken from [added to] such ages. Hence, this part of the diagram is also "polluted" in the earlier SED-age dating, as demonstrated in Figure 16 of B. C. Whitmore et al. (2023a). Table 3 provides more specific object redistribution counts for the entire survey and for individual galaxies. Tallies in the Table indicate the number of objects that have estimated ages which change by more than a factor of 5× (10×). Corresponding fractions relative to the total population in each selection box (C1+C2+C3 for YC $\Rightarrow t \leqslant 10$ Myr, $M_c \geqslant 5 \times 10^4\, M_\odot$ and C1+C2 for GC $\Rightarrow t \geqslant 10$ Gyr, $M_c \geqslant 10^5\, M_\odot$) after SED-TreeFit processing are also given.

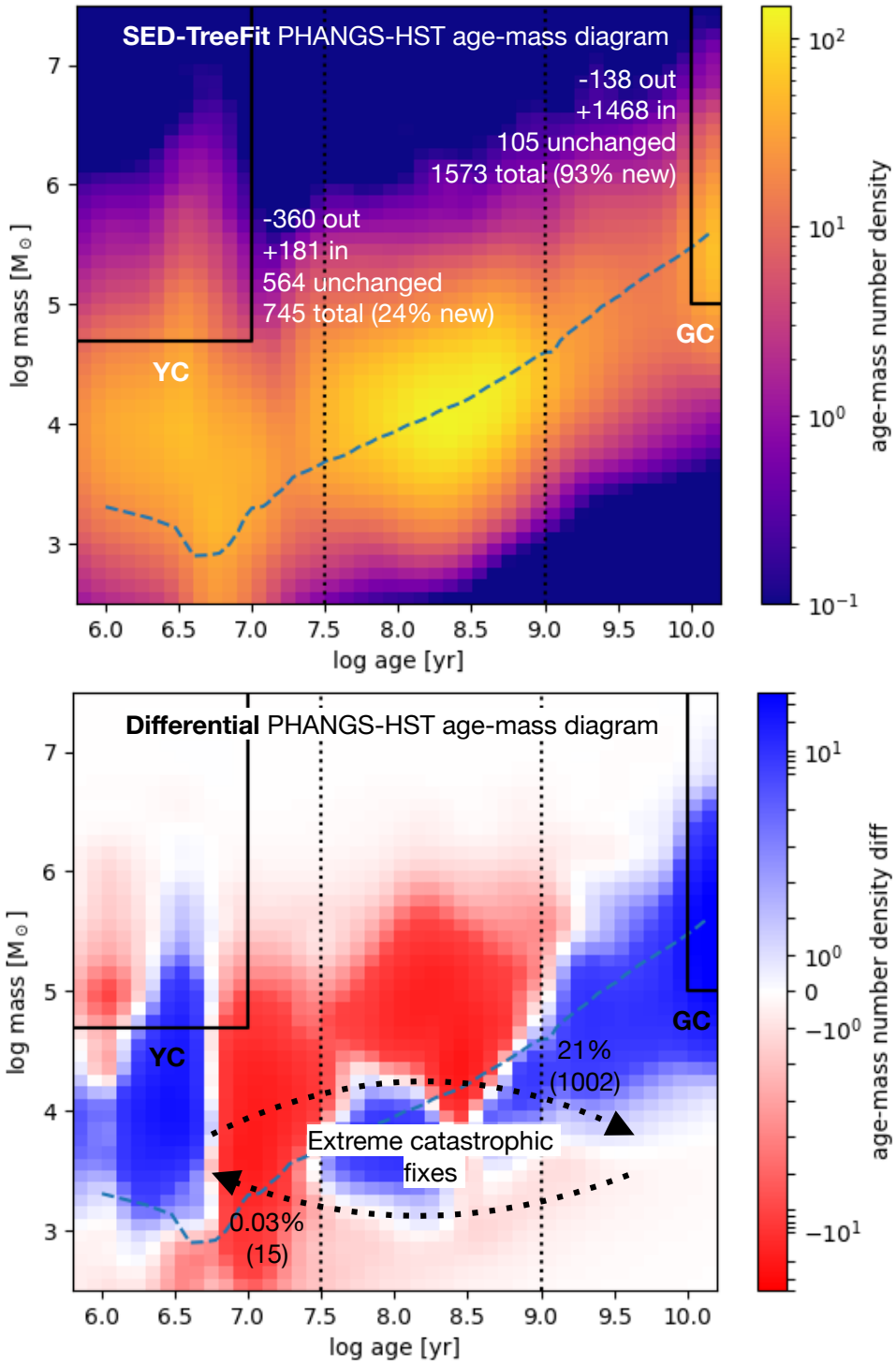

Figure 17. (Top) Aggregated age–mass diagram for the full PHANGS-HST sample of C1+C2 clusters following SED-TreeFit correction, with diagnostic bins corresponding to mass-limited YCs ($t \leqslant 10$ Myr, $M_c \geqslant 5 \times 10^4\ M_\odot$) and GCs ($t \geqslant 10$ Gyr, $M_c \geqslant 10^5\ M_\odot$). The pixel values indicate the density of clusters in each 0.1×0.1 dex age–mass pixel, after representing each object as a 2D Gaussian sized to match the age/mass uncertainty. We provide object counts leaving and entering each population bin, the number with bin membership unchanged, and the total number of clusters in each category after corrections. The percentage of objects entering relative to the total population is also given. We overplot a notional luminosity-based mass limit corresponding to $M_V = -7.5$ with a teal dashed line —see the text for details. (Bottom) Differential age–mass diagram created by subtracting the age–mass distribution based on our initial SED fitting (J. A. Turner et al. 2021) from the SED-TreeFit results. Although rare, we highlight objects that interchange between age extremes (e.g., $\log t\ \mathrm{yr}^{-1} < 7.5$ to $\log t\ \mathrm{yr}^{-1} > 9$, and vice versa) next to the curved arrows.

Dropping the mass and age limits linking objects to the high completeness YC and GC subpopulations, we find more generally that as a result of SED-TreeFit ground-based Hα processing 15% (11%) of ML C1+C2 clusters and 6% (3%) of the ML3 compact associations change age by more than 5× (10×).

Table 3
Summary of C1+C2 Clusters Significantly Redistributed in Age–Mass

Galaxy	ML		YNO Branch	OGC Branch	$E(B-V)$ Fixed	$N_{\rm intoYC}$	$f_{\rm intoYC}$	$N_{\rm intoGC}$	$f_{\rm intoGC}$	$N_{\rm old\text{-}to\text{-}young}$	$N_{\rm young\text{-}to\text{-}old}$
	C1+C2	C3				Having Age Changed by a Factor $\geqslant 5\times$ ($10\times$)				$\log t > 9 \rightarrow < 7.5$	$\log t < 7.5 \rightarrow > 9$
			C1+C2 [C3]	C1+C2	C1+C2 [C3]						
IC 1954	210	647	24 [71]	18	0 [0]	0 (0)	0.0 (0.0)	3 (3)	0.6 (0.6)	0	3
IC 5332	182	416	22 [58]	24	0 [0]	0 (0)	⋯ (⋯)	4 (3)	0.67 (0.5)	0	4
NGC 0628c	1735	1953	89 [196]	183	0 [0]	2 (0)	1.0 (0.0)	28 (21)	0.97 (0.72)	1	23
NGC 0628e	522	540	21 [55]	60	0 [1]	0 (0)	⋯ (⋯)	5 (5)	1.0 (1.0)	0	22
NGC 0685	231	672	10 [20]	28	0 [0]	0 (0)	0.0 (0.0)	5 (2)	0.62 (0.25)	0	8
NGC 1087	569	1091	60 [139]	67	0 [0]	1 (0)	0.05 (0.0)	10 (7)	0.71 (0.5)	0	12
NGC 1097	1809	1962	25 [9]	391	0 [0]	2 (0)	0.03 (0.0)	77 (54)	0.66 (0.47)	0	70
NGC 1300	1654	680	57 [23]	208	0 [0]	1 (0)	0.2 (0.0)	69 (60)	0.99 (0.86)	1	41
NGC 1317	50	128	7 [15]	13	0 [0]	0 (0)	⋯ (⋯)	2 (1)	0.5 (0.25)	0	6
NGC 1365	796	900	76 [157]	162	9 [6]	18 (16)	0.16 (0.14)	55 (45)	0.85 (0.69)	10	22
NGC 1385	552	1129	54 [257]	96	0 [0]	7 (0)	0.19 (0.0)	24 (15)	0.73 (0.45)	0	18
NGC 1433	381	463	17 [9]	96	0 [0]	0 (0)	0.0 (0.0)	24 (19)	0.77 (0.61)	0	17
NGC 1512	569	648	25 [47]	90	0 [0]	0 (0)	0.0 (0.0)	25 (20)	0.93 (0.74)	0	20
NGC 1559	1496	3181	84 [169]	227	0 [1]	10 (0)	0.11 (0.0)	67 (55)	0.97 (0.8)	0	26
NGC 1566	1297	2619	87 [258]	127	0 [1]	2 (0)	0.04 (0.0)	36 (25)	0.82 (0.57)	0	16
NGC 1672	2057	2855	96 [172]	316	0 [0]	2 (2)	0.02 (0.02)	100 (99)	0.99 (0.98)	0	82
NGC 1792	756	1683	43 [161]	229	0 [0]	0 (0)	0.0 (0.0)	53 (43)	0.7 (0.57)	0	30
NGC 2775	214	138	0 [0]	99	0 [0]	1 (0)	0.11 (0.0)	29 (23)	0.67 (0.53)	0	9
NGC 2835	479	1134	48 [125]	23	0 [0]	0 (0)	0.0 (0.0)	4 (4)	0.67 (0.67)	0	5
NGC 2903	1690	3687	21 [23]	303	0 [0]	4 (1)	0.05 (0.01)	63 (46)	0.75 (0.55)	0	51
NGC 3351	777	878	45 [63]	97	0 [2]	0 (0)	0.0 (0.0)	22 (16)	0.81 (0.59)	0	16
NGC 3621	2952	4895	263 [665]	631	2 [4]	1 (1)	0.25 (0.25)	54 (47)	0.96 (0.84)	0	148
NGC 3627	2828	3287	88 [439]	583	4 [5]	6 (2)	0.11 (0.04)	127 (111)	0.87 (0.76)	2	79
NGC 4254	2213	4824	139 [581]	223	0 [3]	8 (1)	0.1 (0.01)	44 (33)	0.8 (0.6)	1	42
NGC 4298	494	760	9 [15]	104	0 [0]	1 (0)	0.12 (0.0)	31 (25)	0.86 (0.69)	0	30
NGC 4303	1824	3813	188 [414]	140	0 [0]	7 (0)	0.06 (0.0)	28 (26)	0.8 (0.74)	0	17
NGC 4321	1486	2563	107 [289]	156	0 [1]	6 (2)	0.08 (0.03)	30 (24)	0.75 (0.6)	0	24
NGC 4535	506	833	31 [62]	57	0 [0]	0 (0)	0.0 (0.0)	19 (15)	0.86 (0.68)	0	9
NGC 4536	741	1106	10 [5]	107	0 [1]	1 (0)	0.04 (0.0)	27 (21)	0.77 (0.6)	0	21
NGC 4548	206	242	5 [5]	77	0 [0]	0 (0)	0.0 (0.0)	34 (23)	0.74 (0.5)	0	11
NGC 4569	504	322	2 [11]	114	0 [1]	1 (0)	0.08 (0.0)	39 (33)	0.8 (0.67)	0	15
NGC 4571	146	377	1 [2]	32	0 [0]	0 (0)	0.0 (0.0)	13 (10)	0.72 (0.56)	0	8
NGC 4654	640	1079	48 [82]	111	0 [1]	8 (0)	0.08 (0.0)	34 (25)	0.81 (0.6)	0	19
NGC 4689	313	582	15 [12]	46	0 [0]	0 (0)	0.0 (0.0)	18 (15)	0.72 (0.6)	0	2
NGC 4826	122	514	9 [56]	51	1 [1]	0 (0)	0.0 (0.0)	6 (3)	0.6 (0.3)	0	6
NGC 5068	643	2286	52 [222]	73	0 [1]	0 (0)	⋯ (⋯)	4 (3)	0.8 (0.6)	0	16
NGC 5248	738	1192	50 [130]	135	1 [0]	7 (0)	0.15 (0.0)	37 (26)	0.74 (0.52)	0	19
NGC 6744	1515	3079	33 [131]	192	0 [0]	0 (0)	⋯ (⋯)	21 (16)	0.78 (0.59)	0	27
NGC 7496	283	452	51 [81]	37	0 [0]	1 (0)	0.1 (0.0)	6 (4)	0.46 (0.31)	0	8
Total	36,180	59,610	2012 [5229]	5726	17 [29]	97 (25)	0.07 (0.02)	1277 (1026)	0.81 (0.65)	15	1002

Note. We present the numbers of Class 1+2 and Class 3 clusters for each target according to ML classification, and the total number of Class 1+2 YNO branch, OGC branch, and high $E(B-V)$ allowance objects. These columns are followed by information regarding the ML C1+C2 mass-limited (limits shown in Figure 17) of YCs and GCs having SED-fix ages differing significantly from the conventional PHANGS pipeline output. We tally the number and fraction of "redistributed" objects in these categories, changing by factors of at least $10\times$ for both YCs and GCs. Fractions are provided in comparison to the total (mass and age-limited) ML C1+C2+C3 and ML C1+C2 samples, respectively, for the YC and GC populations. Entries of "⋯" are given for targets having no YCs with $M_c \geqslant 5 \times 10^4 M_\odot$ identified, even with SED-TreeFit methods. The last two columns provide the absolute number of objects interchanging between age extremes (e.g., $\log t < 7.5$ to $\log t > 9.0$, and vice versa—the catastrophic fixes in Figure 17) without imposing mass limits.

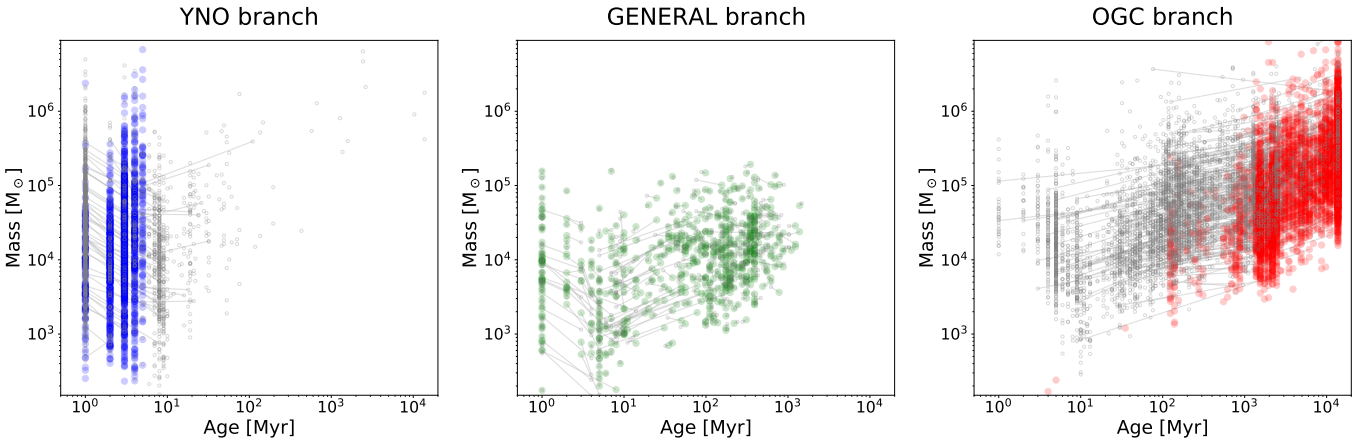

Figure 18. Comparison of previous age–mass determination (method of J. A. Turner et al. 2021, gray dots) to SED-TreeFit age–mass determination (colored circles) for subsets of objects assigned to the YNO-fix model grid (top left panel, blue), general pipeline model grid (top right panel), and OGC-fix model grid (bottom left panel, red) branches of the decision tree. Some lines are shown to connect results for the same source. For YNO and OGC populations, we show all objects on the branch as points, but only display a line for every 20th object. For the more numerous population of objects in the general grid, we only display every 40th object, but include a connecting line for each one of these.

The bottom panel of Figure 17 shows the differential age–mass diagram to aid in visualizing differences between the results from SED-TreeFit analysis and from our previous method of SED-fitting. Blue areas gained objects from the SED-TreeFit procedure, red areas lost objects, and white areas had little or no change. The young and old regions of the age–mass diagram show significant increases resulting from fairly uniform depopulation of the intermediate-age region between $7 < \log\, t\ \mathrm{yr}^{-1} < 9$ at cluster masses greater than $\log(M_c/M_\odot) = 4.5$. Even for objects assigned to the general model grid, we assign physical parameters based on modes in the CIGALE PDFs rather than adopting the single best fit. This permits variation of cluster age, mass, and $E(B-V)$ totally unrelated to our decision tree in comparison to the J. A. Turner et al. (2021) minimum χ^2 outcome. Such changes manifest in the differential age–mass diagram as the enhancement of comparatively low-mass objects at $7.5 < \log\, t\ \mathrm{yr}^{-1} < 8.3$ (32–200 Myr) and again at $8.7 < \log\, t\ \mathrm{yr}^{-1} < 8.9$ (∼500–800 Myr), often taking them from minimum χ^2 ages of 5–10 Myr. The most catastrophically incorrect age from previous SED-fitting (objects switching between extremes of $\log\, t\ \mathrm{yr}^{-1} < 7.5$ to $\log\, t\ \mathrm{yr}^{-1} > 9$) are almost unidirectional in the sense of age correction, with 1002 C1+C2 previously YCs given a new age older than 1 Gyr, but only 15 previously ancient clusters now identified to be younger than ∼32 Myr ($\log\, t\ \mathrm{yr}^{-1} < 7.5$). Table 3 breaks down the catastrophic failures fixed by our work on a galaxy-by-galaxy basis.

Figure 18 further illustrates the flow of objects belonging to specific branches of our SED-fitting decision tree, and Table 3 reports the number of objects assigned to YNO/OGC branches. Objects categorized as YNOs generally had previous ages of 1–4 Myr (already), 7–9 Myr, or (with less frequency) up to $\lesssim$100 Myr. As noted by B. C. Whitmore et al. (2023a), most of the revised ages for newly recovered GCs start in one of two regimes (4–10 Myr or ∼30 Myr to a few 10^8 yr). The objects kept on the general model grid (center panel in Figure 18) typically shift (age, mass) position as described in the previous paragraph, although some are also found to shift to modestly younger ages from within the 1–10 Myr range and others remain in close agreement with their earlier age determination.

5.1.2. Exceptional Clusters: Young Massive Cluster and OGC Populations

Young massive clusters (YMCs) are of particular interest because they may be young analogs of ancient GCs (e.g., B. C. Whitmore et al. 1993; R. W. O'Connell et al. 1994; A. J. Barth et al. 1995; G. Oestlin et al. 1998; S. S. Larsen & T. Richtler 1999; B. C. Whitmore et al. 1999). Meanwhile, OGCs reveal insight pertaining to the early history of PHANGS-HST galaxies. Table 4 provides the galaxy-by-galaxy count of YMC candidates[42] and OGCs in our SED-TreeFit catalogs, tabulating each in multiple ways to permit different working definitions for YMCs ($M_c \geqslant 10^6\, M_\odot$ and $10^5\, M_\odot$, both for age $\leqslant$10 Myr) and to assess our systematic uncertainty for OGCs.

Our SED-TreeFit results from ground-based Hα decision tree processing show that only about one-eighth of the PHANGS-HST galaxies have formed YMC candidates that reach $10^6\ M_\odot$, with only a few per galaxy (NGC 1097, NGC 1365, NGC 1672, NGC 2903, NGC 3627, which have 3, 9, 3, 2, and 2, respectively, see Table 4). A total of 19 objects (13 C1 + 6 C2) younger than 10 Myr with masses $\geqslant 10^6\ M_\odot$ are found in our 38 galaxies (of these 7/19 are estimated as 1–3 Myr old). The count of such exceptional YMC candidates decreases to 15 according to our HST Hα SED-TreeFit work, but this count only considers 17 of 38 galaxies. We find very young clusters with masses $\approx 10^5\, M_\odot$ are common, and form in the majority of PHANGS-HST galaxies except the lowest mass and most quiescent. The population of YMCs in PHANGS-HST galaxies in relation to the environments in which they form will be the focus of a dedicated upcoming study (J. C. Lee et al. 2025, in preparation).

Although PHANGS-HST cluster age distribution analysis is also reserved as the focus of a future study (e.g., when HST Hα imaging is available for our full galaxy sample), we currently find that the most massive YMC candidates ($M_c \geqslant 10^6\ M_\odot$) are generally very short-lived. For instance, in the age interval from 100 Myr to 1 Gyr we only identify a total of three such C1 + C2

[42] We are currently undertaking a detailed, holistic inspection of the YMC candidates in our catalogs, based on the full suite of PHANGS data from HST/JWST/ALMA/MUSE, in order to confirm these exceptional clusters. This is the reason we refer to them as YMC candidates herein.

Table 4
Summary of Detected YMCs and OGCs in ML Catalogs

Galaxy	N_{YMC} SED-TreeFit $M_* \geqslant 10^6\ M_\odot$	N_{YMC} SED-TreeFit $M_* \geqslant 10^5\ M_\odot$	N_{GC} SED-TreeFit $M_* \geqslant 10^5\ M_\odot$, age $\geqslant 10$ Gyr	N_{GC} SED-TreeFit OGC Branch	N_{GC} B. C. Whitmore et al. (2023a)	N_{GC} M. Floyd et al. (2024)
IC 1954	0	0	5 (6)	18	⋯	⋯
IC 5332	0	0	6 (8)	24	⋯	⋯
NGC 0628c	0	0	29 (41)	183	65	236 (70 + 166)
NGC 0628e	0	0	5 (1)	60	⋯	incl. with NGC 0628c
NGC 0685	0	2	8 (16)	28	⋯	⋯
NGC 1087	0	5	14 (18)	67	⋯	⋯
NGC 1097	3	40	116 (99)	391	⋯	⋯
NGC 1300	0	1	70 (42)	208	⋯	⋯
NGC 1317	0	0	4 (7)	13	⋯	⋯
NGC 1365	9	69	65 (75)	162	55	⋯
NGC 1385	0	9	33 (42)	96	⋯	⋯
NGC 1433	0	0	31 (29)	96	46	94 (54 + 40)
NGC 1512	0	3	27 (46)	90	⋯	⋯
NGC 1559	0	23	69 (59)	227	⋯	173 (73 + 100)
NGC 1566	0	14	44 (40)	127	⋯	176 (139 + 37)
NGC 1672	3	50	101 (25)	316	⋯	293 (27 + 266)
NGC 1792	0	43	76 (69)	229	⋯	196 (181 + 15)
NGC 2775	0	4	43 (72)	99	⋯	115 (115 + 0)
NGC 2835	0	0	6 (15)	23	⋯	⋯
NGC 2903	2	41	84 (48)	303	⋯	⋯
NGC 3351	0	12	27 (35)	97	50	105 (62 + 43)
NGC 3621	0	2	56 (36)	631	⋯	⋯
NGC 3627	2	13	146 (35)	583	⋯	521 (61 + 460)
NGC 4254	0	22	55 (17)	223	⋯	⋯
NGC 4298	0	2	36 (35)	104	⋯	⋯
NGC 4303	0	36	35 (10)	140	⋯	94 (15 + 79)
NGC 4321	0	32	40 (30)	156	⋯	238 (66 + 172)
NGC 4535	0	7	22 (29)	57	⋯	72 (56 + 16)
NGC 4536	0	12	35 (36)	107	⋯	⋯
NGC 4548	0	0	46 (55)	77	⋯	86 (85 + 1)
NGC 4569	0	5	49 (57)	114	⋯	⋯
NGC 4571	0	0	18 (22)	32	⋯	41 (41 + 0)
NGC 4654	0	44	42 (54)	111	⋯	91 (80 + 11)
NGC 4689	0	1	25 (30)	46	⋯	⋯
NGC 4826	0	0	10 (14)	51	⋯	42 (42 + 0)
NGC 5068	0	0	5 (7)	73	⋯	⋯
NGC 5248	0	20	50 (54)	135	⋯	132 (94 + 38)
NGC 6744	0	0	27 (32)	192	⋯	⋯
NGC 7496	0	5	13 (21)	37	⋯	⋯
Total	19	517	1573 (1367)	5726	216	2705

Note. The definition of a YMC varies in the literature (A. Adamo et al. 2017), so we tabulate the population for two mass limits, $10^6\ M_\odot$ and $10^5\ M_\odot$, both for age $t \leqslant 10$ Myr and Classes 1, 2, and 3 from the ML catalog. We also consider two definitions of GC as determined from our SED-TreeFit catalogs: (i) Class 1 and 2 clusters with mass $\geqslant 10^5\ M_\odot$ and $t \geqslant 10$ Gyr, (ii) objects successfully attributed to the OGC branch regardless of mass or age. B. C. Whitmore et al. (2023a) only analyzed human-classified Class 1 and 2 clusters and used an age limit of $\log(t) = 9.5$, so their GC counts are difficult to compare against in the context of this table where our mass- and age-limited GC totals (third column) refer to the ML-classified populations older than $\log(t) = 10.0$. To ease comparison with B. C. Whitmore et al. (2023a), we provide analogous tallies as numbers in parentheses. GC counts from M. Floyd et al. (2024) are provided in the last column, listing their ML catalog results with subdivision according to their bright and faint categories.

objects, compared to 15 with $t \leqslant 10$ Myr. Due to the increased reliability of our HST Hα decision tree branch assignments, we use those outcomes here. Assuming massive YMCs formed at a roughly constant rate over the last Gyr, it seems they are subject to relatively extreme disruption, perhaps to be expected if their formation tends to occur in particularly dynamic, high-pressure environments. There are also a number of internal processes that can disrupt clusters with masses $\geqslant 10^6\ M_\odot$. Clusters of all masses can be born unbound (have positive energy). After gas leftover from formation is pushed out due to stellar feedback, bound clusters continue to lose mass due to stellar evolution. Simulations show that clusters that are weakly bound and subject to the tidal field of their host galaxy can be disrupted on fairly short timescales (D. F. Chernoff & M. D. Weinberg 1990). Massive clusters can also be disrupted due to tidal interactions with molecular clouds (L. Spitzer & R. Harm 1958), particularly in dense galactic environments like star-forming rings. In future work, we will characterize environmental conditions related to the birth sites of YMCs in our sample, using the local physical conditions tabulated by J. Sun et al. (2022).

Our PHANGS-HST cluster catalogs include a large number (∼4900, estimated as ≃85% bona fide GCs of 5726 OGC objects) of likely GCs, a dramatic increase in the number of GCs known in spiral galaxies. However, the specific total

depends critically on the decisions made for counting, as demonstrated in Table 4, where we tally in two different ways (objects meeting GC-representative age and mass cuts, versus objects assigned to the OGC branch of our SED-TreeFit decision tree). Note that imposing a lower limit for GC age (as done in the third column of Table 4) has a particularly large impact on counts. Though not listed in the "total" line of the table, a limit of log t y$^{-1} \geqslant 10.0$ (9.5) imposed on the OGC branch population represented in the fourth column brings the OGC tally down to 1916 (2934) objects from 5726.

In Table 4, we compare our results on the GC population with the outcome of B. C. Whitmore et al. (2023a), who conducted a concept study for much of the SED-TreeFit method using four PHANGS-HST galaxies. In that study, PHANGS-MUSE Hα imaging was used to identify and reject reddened young clusters from the population of candidate GCs. The number of identified GCs is somewhat different between the two studies, with counts from SED-TreeFit being ∼60%–70% of those of B. C. Whitmore et al. (2023a) for NGC 1433, NGC 3351, and NGC 628 but more comparable in NGC 1365 (35% increase for SED-TreeFit), using the mass- and age-limited tallies from our work. The tendency for our counts to be less than those of Whitmore is partially a consequence of B. C. Whitmore et al. (2023a) using a single $Z_{\odot}/50$ model grid, whereas we allow $Z_{\odot}/50$ and $Z_{\odot}/5$.

Another study that can be used for comparison is that of M. Floyd et al. (2024), who conducted a search for candidate GCs that was independent of the PHANGS pipeline's determined ages. They relied instead upon inspection of a cluster sample selected to have $B - V \geqslant 0.5$ mag and $V - I \geqslant 0.73$ mag, assessing each object and its environment directly in the NUV-*U*-*B*-*V*-*I* images. They also allow both C1 + C2 clusters as potential candidate GCs, without the rejection of C2 clusters in spiral arms, which we impose. Table 4 provides the candidate GC counts from M. Floyd et al. (2024) in the far right column. Comparing their combined (bright and faint) counts to our tally of SED-TreeFit OGC branch objects shows that they generally include from 0.75 to 1.25× as many objects as candidate GCs as we do, using our inclusive OGC color–color region (see Figure 6). Two galaxies out of this range with substantially more OGC branch objects are NGC 1559 and NGC 4303, for which they include 1.3–1.5× as many candidate GCs. At the other extreme, two galaxies with considerably fewer OGC branch objects than M. Floyd et al. (2024) GC candidates are NGC 1566 and NGC 4321, for which they include 0.66–0.72× as many as our SED-TreeFit outcome.

The statements above regarding B. C. Whitmore et al. (2023a) and M. Floyd et al. (2024), combined with the knowledge that the more restrictive OGC color–color region we tested during SED-TreeFit development cuts our OGC branch population by 38% (HST Hα) and 36% (ground-based Hα), we conclude that the inclusive OGC color–color region does not yield many erroneous OGC branch assignments. This is also supported by the inspection of random samples described in Section 4.5.

We note that Floyd's slightly bluer than typical $V - I$ color limit for GCs, and their broader inclusion of asymmetric clusters, led to the initial discovery of an additional, slightly younger population of understudied faint clusters originating in the disk (ages a few to several Gyr). M. Floyd et al. (2024) find that the ensemble of these clusters has a more extended spatial profile than the brighter GC candidates. Our results are generally in line with those of M. Floyd et al. (2024) with respect to the existence of faint GC candidates, but we have not yet examined their location within our 38 PHANGS-HST galaxies.

5.1.3. Regarding the 10–30 Myr and Other "Age Gaps"

A noticeable dearth of clusters at ages from ∼10 to ∼30 Myr is a known artifact of SED-fitting (R. Chandar et al. 2010; B. C. Whitmore et al. 2023a) due to the inherent degeneracy of the SSP model at these ages where clusters have very similar colors for an extended period of time (see Figure 1). Indeed, the BC03 track crisscrosses itself multiple times from 12 to 25 Myr, taking the form of a bow tie in the *UBVI* color–color diagram. In practice, this feature compresses the SED space for which clusters can be attributed to each of these degenerate models (see the animated version of Figure 13 for a graphical understanding), leaving neighboring portions of the track which are slightly younger or slightly older to be preferentially associated with clusters having colors that fall just beside a reddening vector extended from the bow tie. The problem is accentuated further by additional model degeneracies with the 8 Myr and 1–3 Myr positions of the BC03 track (see Figures 1 and 2).

The full sample aggregated C1+C2 age–mass diagram of Figure 17 (top panel) shows this nonphysical artifact as a deficit (or age "gap") found just to the younger side of the left vertical dotted line. The SED-TreeFit methodology does not improve upon the previous fitting outcome in this respect (nor was it intended to). However, we can see that compared to ordinary scatter plot representations of the age–mass distribution, the 10–30 Myr gap is minimized in terms of appearance owing to our technique of rendering the age–mass density with specific accounting for age and mass uncertainty. Looking ahead to the galaxy-specific plots of Section 5.1.4, one can see that without the smoothing attribute of such a presentation, the 10–30 Myr gap is more apparent.

For now, we simply point out this characteristic of the age–mass diagrams. Work is ongoing to determine a statistical fix for the issue based on the SED-fitting outcome for an ensemble of synthetic clusters having a flat age distribution, mass above the completeness limit, and a plausible distribution of reddening. Such a correction could be directly applied to density age–mass distributions, such as shown in Figure 17.

Another deficit in the apparent cluster population can be seen between 1 Gyr and 10 Gyr. This is probably due to a combination of two effects. The first is that we are only using three metallicities in our SED-TreeFit procedure (i.e., $Z_{\odot}$, $Z_{\odot}/5$, $Z_{\odot}/50$), while the true metallicities will gradually change during the first several billion years. The second effect is the fact that the BC03 models are roughly parallel to the reddening vector in this portion of the BC03 models, making the "cross section" smaller for age estimates between 1 and 13 Gyr (see Figure 1). For these and other related reasons (e.g., the dimming of brightness as a function of age; very long-term cluster disruption), the 1–10 Gyr range has been largely unexplored in the study of age–mass diagrams. We note in passing that our SED-TreeFit processing has lessened the severity of the 1–10 Gyr underpopulation.

5.1.4. Galaxy-specific Age–Mass Diagrams

Figures 19 and 20 show the age–mass diagrams of Class 1, 2, and 3 objects for all 38 PHANGS-HST galaxies. The diagrams include representative uncertainty crosses for clusters at two example masses, determined as for Figure 16 in Section 4.8. The panels are plotted in order of decreasing offset (ΔMS) from the

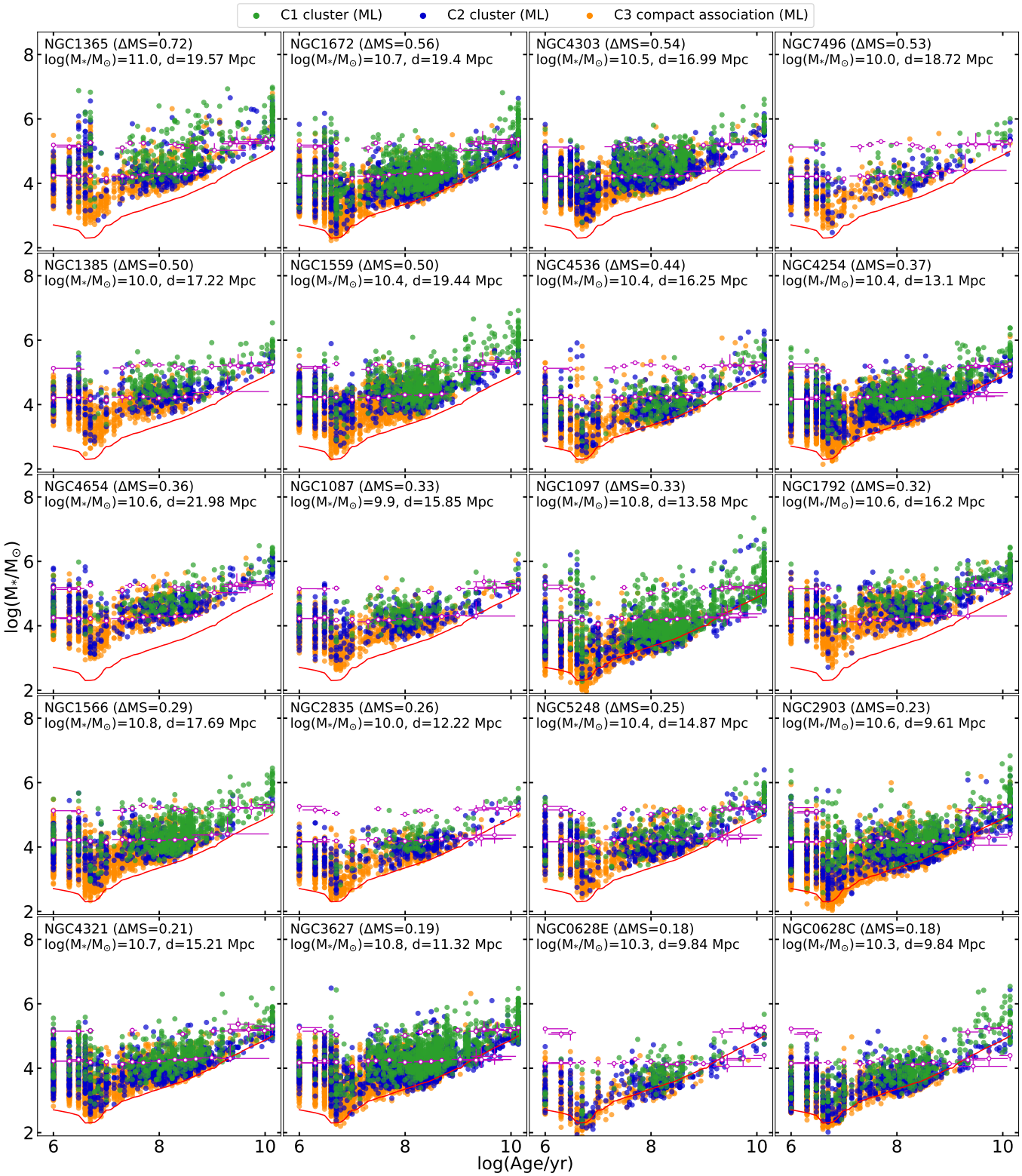

Figure 19. Distribution of stellar mass and age for all 38 PHANGS-HST galaxies, plotting ML-classified clusters of Class 1 (green) and 2 (blue) plus compact associations of Class 3 (orange). With crosses (purple) we indicate the median $+/-1\sigma$ uncertainty of representative clusters at the approximate distance of each galaxy (evaluated as described at the end of Appendix A). Cross position indicates the median age and mass of the clusters considered for each median uncertainty estimate, and no marker is shown if the number of such clusters drops too low in the associated age/mass/distance bin. The panels are presented in order of decreasing ΔMS. With a red line, we display the detection limit corresponding to $M_V = -6$ mag. Figures 19 and 20 are interactive, allowing one to examine C1+C2 +C3 objects jointly (as in the static figure); plus C1-only, C2-only, and C3-only views.

(An animation of this figure is available in the online article.)

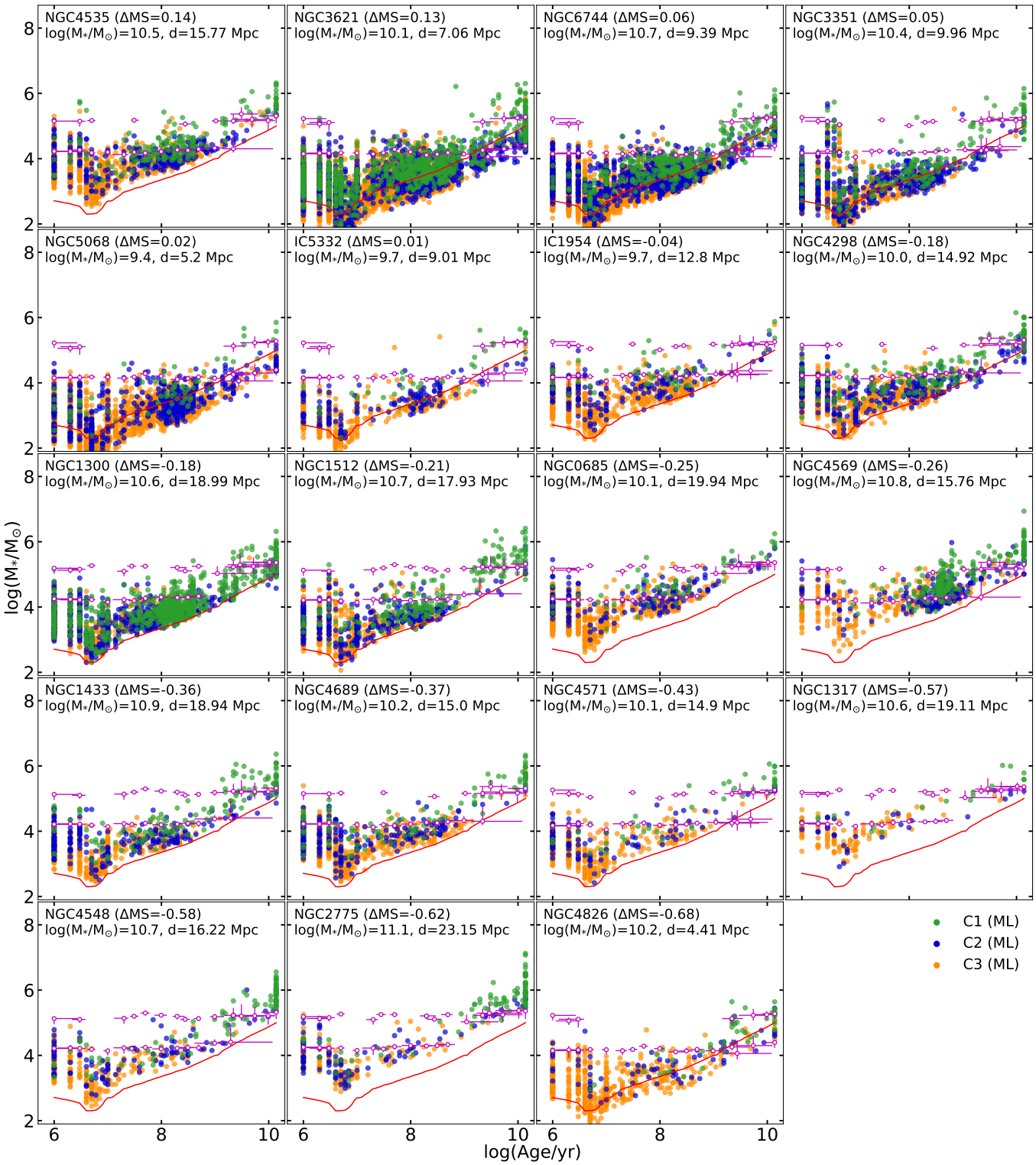

Figure 20. Continuation of Figure 19, with its own animation.
(An animation of this figure is available in the online article.)

star-forming MS. We overplot a fixed notional completeness curve ($M_V = -6$) in all panels, illustrating the decline in mass sensitivity with distance. Galaxies comparatively nearby have detected (faint/lower mass) objects below the red curve, whereas our catalogs for galaxies at the distant end of our sample do not even recover clusters with $M_V = -6$.

These age–mass diagrams give us powerful insight into the star formation history (SFH) and evolution of each galaxy. Some results are (1) the relative number of OGCs versus young-intermediate-age clusters varies significantly, (2) Class 1, 2, and 3 objects systematically exhibit different trends in their age distribution, (3) SFH bursts and other longer-term

changes are seen as enhancements or trends in the object count versus age.

In the past, the study of the relative ratio of OGC to younger clusters has been complicated by the lack of systematic correction for the age–metallicity degeneracy that we address in our work. As an illustration that the ratio varies and provides information on the galaxy history, we compared the results for IC 1954 to NGC 4571, both at a similar distance with comparable sensitivity. (Note that, in general, for any two galaxies, completeness limits would need to be considered before selecting mass ranges for comparison. The same is true for comparing different age ranges within a single galaxy.) NGC 4571 has several times more OGCs than IC 1954, despite IC 1954 having many more intermediate-age clusters than NGC 4571, likely reflecting a very different SFH (and CFH = cluster formation history) over cosmic time.

It is also obvious that the OGC population is larger in the massive galaxies of the sample, as one expects on the basis of previous specific frequency studies. However, the PHANGS-HST imaging does not cover the full extent of each galaxy, making a detailed study of this correlation less valuable with the observations in hand. We look forward to complete coverage of galaxy disks and inner halo using the Nancy Grace Roman Space Telescope.

The varied age distribution of Class 1, 2, and 3 objects was already apparent in the directly observable color–color diagrams of Paper I, immune from SED-fitting methodological concerns, but now can be investigated more quantitatively using the ages coming from our SED-TreeFit approach. Nearly all the galaxies in our sample of 38 show clear trends in this regard, with the C1 (green) clusters piling up at intermediate and older ages and the C3 (orange) compact associations found in abundance at young ages ($\log t\ \mathrm{yr}^{-1} \lesssim 8$). This is generally true for a diverse range of galaxies in the PHANGS-HST sample, from the first (quite active) galaxy in Figure 19 (NGC 1365) to the last (largely quiescent) galaxy in Figure 20 (NGC 4826). The decline of Class 3 versus age is not an indication that these star formation events cease to be a significant structured population in the overall census of star formation products, but rather that they morph and merge into spatially larger complexes having a more prolonged and complex history.[43] C1 clusters are preferentially found to have older ages consistent with the idea that they are the accumulated population of (still-)bound clusters.

Several galaxies show remarkable enhancements or deficits in their age–mass diagrams, indicative of major events in their past. These events often correlate with a galaxy's position in the galaxy MS, which will be discussed in Section 5.4. For instance, in terms of star formation bursts, NGC 1365 shows a prominent enhancement of high-mass clusters at ages $\lesssim 5$ Myr, often occurring in the central star-bursting ring of the galaxy studied by B. C. Whitmore et al. (2023b). An examination of several other galaxies in Figures 19 and 20 (e.g., NGC 1097, NGC 1672, NGC 3351) shows similar starbursts at young ages. Long-term deficits in SFH are also quite evident in our cluster age–mass diagrams. NGC 4569 is a nice example as it is a Virgo cluster member which has been recently ram pressure stripped of its ISM (A. Boselli et al. 2006), causing a relative deficit of clusters and compact associations with ages less than 100 Myr.

[43] e.g., PHANGS-HST multiscale stellar associations, such as described by K. L. Larson et al. (2023).

5.2. GC Mass (and Luminosity) Functions

Figure 21 (top) shows the PHANGS-HST GCMF from our SED-TreeFit analysis[44] (red histogram and thick red kernel density estimation (KDE) distribution) for GCs selected as ML C1 or C2 objects attributed to the OGC branch and assigned ages of 10 Gyr or more. The form of the GCMF is thought to be shaped by the preferential destruction of lower mass objects (S. M. Fall & Q. Zhang 2001; A. Jordán et al. 2007) such that it is expected to have a turnover or peak near $10^5\ M_\odot$. In Figure 21 (top), we see a peak near $\log M_c/M_\odot \sim 5.4$ when aggregating over all PHANGS-HST targets, although this should be considered an upper limit because of incompleteness in the more distant galaxy sample. For the purpose of illustration, the thin red line shows a KDE-smoothed GCMF for only those PHANGS-HST galaxies closer than 15.5 Mpc (yielding $\sim$ half the total GC population in our census) and the peak shifts by $\sim$0.1–0.2 dex downward. Thus, the depth of our catalogs is sufficient to recover the upper end of the GCMF, but artificially biases the apparent peak of the GCMF to higher masses due to sample incompleteness at larger distances (see the range of GC mass limits galaxy-by-galaxy in Figures 19 and 20—in each target the incompleteness is significant at a factor of a few higher than the lowest mass GC recovered).

Nevertheless, we compare our results with the observed Milky Way GCMF from the studies of H. Baumgardt & M. Hilker (2018) and M. Hilker et al. (2020), shown as the black and gray dashed curves in Figure 21 (and Figure 22). Comparison should be made at relatively high masses only, owing to differing incompleteness characteristics of all catalogs. We see that the fully aggregate sample (Figure 21, red thick curve and histogram) shows tentative evidence of a small number of clusters significantly more massive ($\log M_c/M_\odot \gtrsim 6.7$–7.1) than exist in the observed Milky Way population.[45] Comparison of the thin red line (for galaxies with $d < 15.5$ Mpc) shows the majority of these candidate very massive GCs are in the more distant half of our sample for which our target galaxies become increasingly more massive (in Figure 22 we return to this issue), and that the nearby half agrees more closely with the observed Milky Way upper GCMF, and indeed with the majority of the GCMF down to $\log M_c/M_\odot \sim 4.7$. We note that the objects at the extreme high-mass end of the PHANGS-HST GCMF could be considered possible analogs to Omega Cen ($\log M_c/M_\odot \sim 6.6$, R. D'Souza & H.-W. Rix 2013) and thus might each harbor an intermediate-mass black hole (albeit controversial even for Omega Cen, e.g., Astronomical Society of South Africa (ASSA) 2008; E. Noyola et al. 2008, 2010; J. Anderson & R. P. van der Marel 2010; R. P. van der Marel & J. Anderson 2010; H. Baumgardt et al. 2019b; M. Häberle et al. 2024; A. Bañares-Hernández et al. 2025). Though unlike our PHANGS disk galaxies, the supergiant elliptical M87 GC system has objects as massive as $\log M_c/M_\odot \sim 6.8$–7.0 (B. C. Whitmore et al. 1995; H.-X. Zhang et al. 2018), even specifically excluding ultracompact dwarfs. At the very least,

[44] Recall that M. Floyd et al. (2024) have also compiled a list of PHANGS-HST GC candidates, independently of SED-fitting outcomes. We have included a flag in our tables indicating objects that they called GCs.

[45] For the GC-specific analysis of Section 5.2, we inspected all age-selected GCs with $\log M_c/M_\odot \geqslant 6.7$ (the point at which PHANGS-HST OGC populations begin to exceed the Milky Way population) in the manner of Section 4.5 and excised any objects that appear to have received spurious old ages, that are likely not older than 10 Gyr. Three objects were removed: NGC 1097 2001, NGC 1097 2008, and NGC 4321 2243.

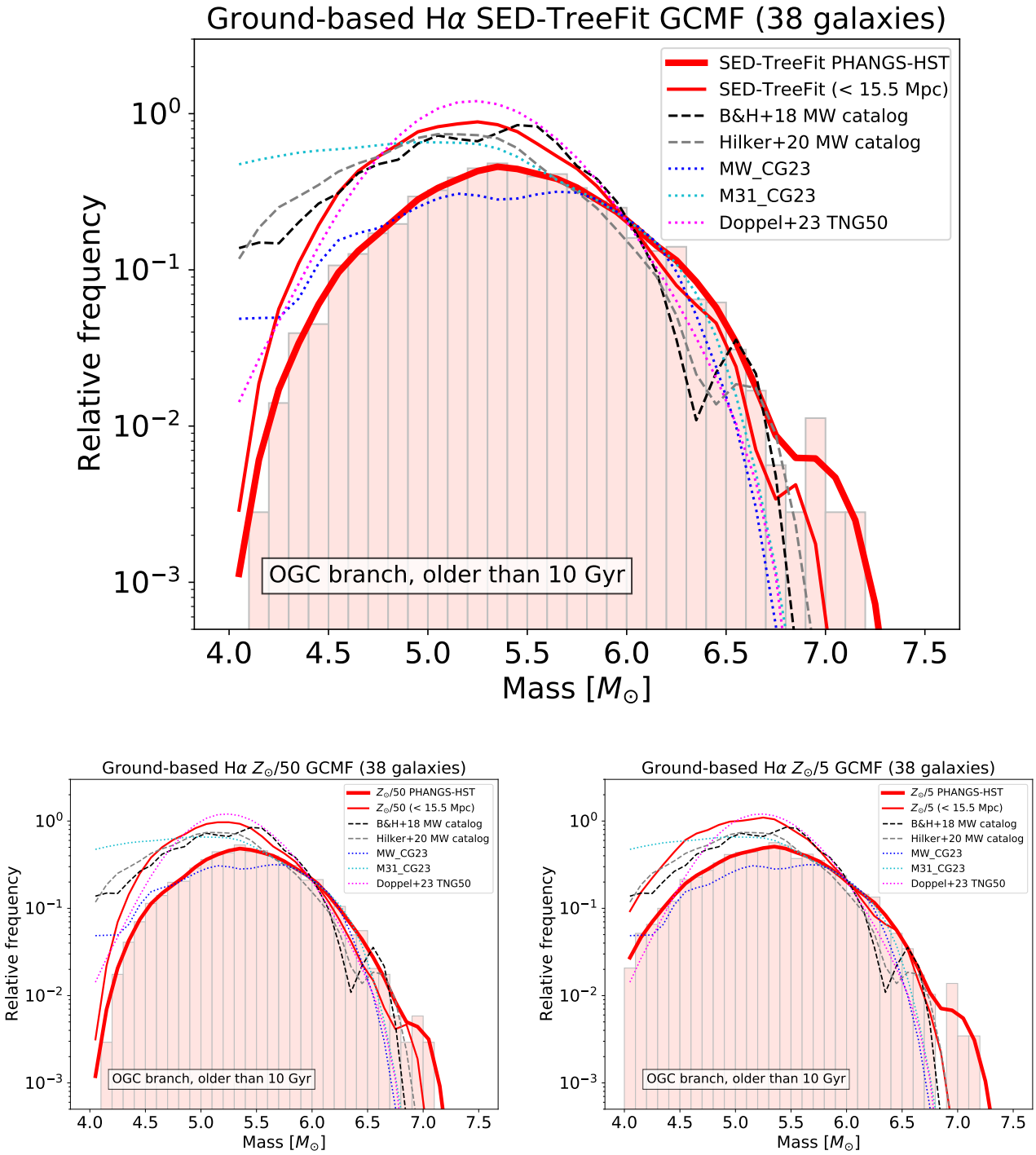

Figure 21. Mass function for GCs in all 38 PHANGS-HST galaxies (red histogram and thick red KDE curve): (top) final SED-TreeFit catalog, (bottom left) if we had assumed $Z_\odot/50$ for all OGCs, (bottom left) if we had assumed $Z_\odot/5$ for all OGCs. In each panel, we also show the SED-TreeFit GCMF for the subset of galaxies at distances less than 15.5 Mpc (thin red curve). The black dashed curve shows the mass function of Milky Way observed GCs from H. Baumgardt & M. Hilker (2018), who analyzed objects taken from the W. E. Harris (2010) GC catalog. The gray dashed curve shows the M. Hilker et al. (2020) Galactic census. The blue and cyan dotted curves are simulated GCMFs for Milky Way and M 31 analogs, respectively, taken from Y. Chen & O. Y. Gnedin (2023) showing only clusters determined to be formed in situ. In magenta, we show the $\sim$ 200,000 simulated GCs (occupying 39 massive host halos at $z = 0$) from J. E. Doppel et al. (2023), identified within the TNG50-1 simulation. All curves have been normalized to the Milky Way observed population for $5.8 < \log(M_c/M_\odot) < 6.3$.

an improved census of such very massive GCs should help efforts aimed at understanding their origin (possibly as cores of accreted dwarf galaxies).

Future works focused specifically on the PHANGS-HST GCs will thoroughly compare the observed GCMF to model GC populations. For the present paper, Figure 21 shows the PHANGS-HST GCMF in comparison to three simulation predictions. In blue and cyan dotted lines, we plot the GCMF predicted by Y. Chen & O. Y. Gnedin (2023) for Milky Way and M31-like analogs, respectively, restricting the sample to only clusters thought to be formed in situ. With the magenta line, we indicate the GCMF aggregated over 39 halos in the TNG50-1 simulation by J. E. Doppel et al. (2023). The PHANGS-HST GCMF (especially for our more nearby

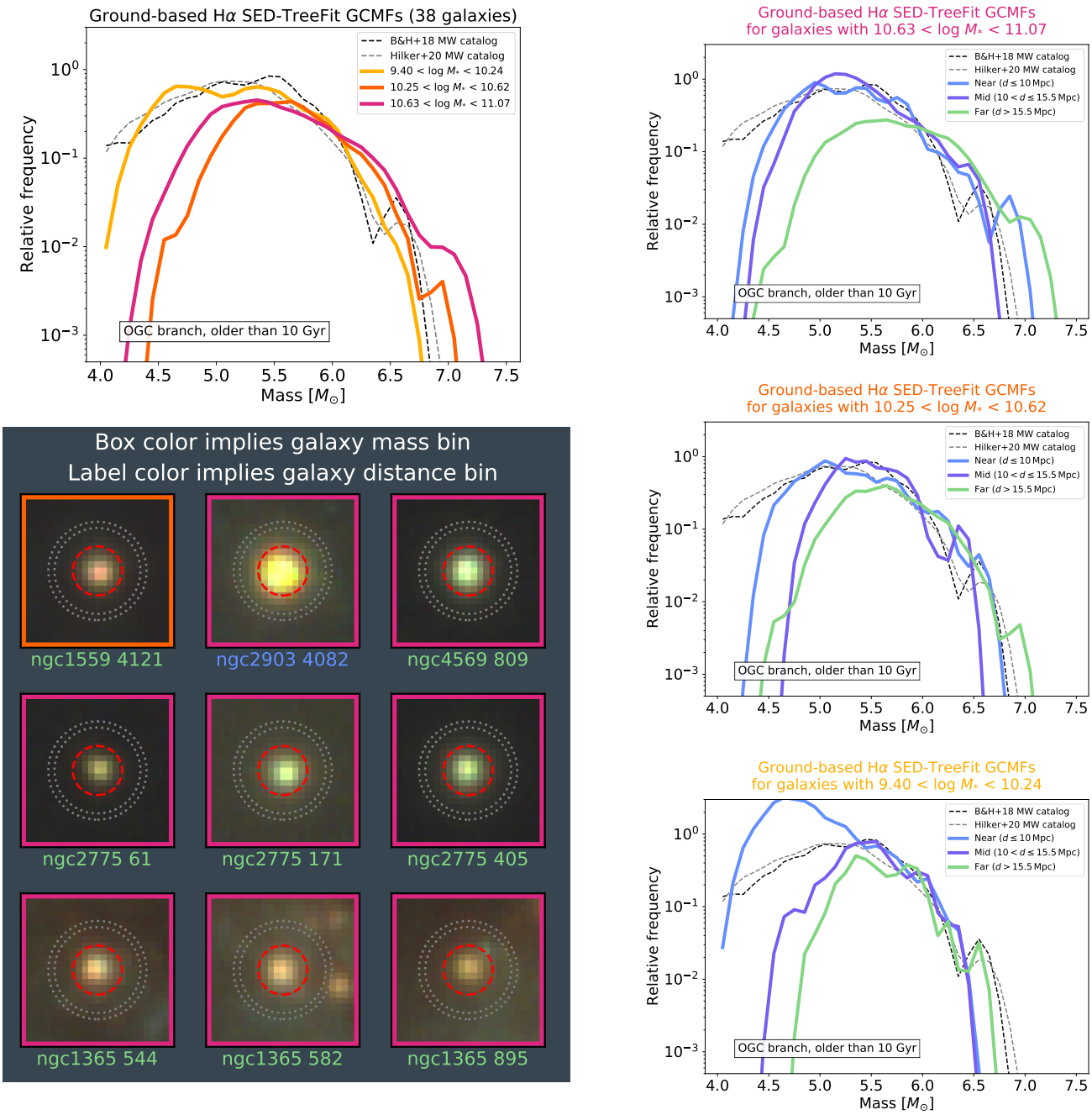

Figure 22. (Top left) Mass functions for OGCs (OGC branch objects assigned SED-TreeFit ages of 10 Gyr or more) in all 38 PHANGS-HST galaxies, subdividing the sample into three bins of total stellar mass (M_*) per galaxy. (Right column) GCMFs created by further subdividing each M_* subset into three bins of distance. Each plot shows all three distance bins for a particular M_* interval: (top) higher galaxy masses; (middle) mid-range galaxy masses; (bottom) lower mass galaxies. (Bottom left) Montage of image cutouts (*IVB* as RGB) for each OGC branch cluster more massive than log $M_c/M_\odot = 6.7$ represented in the GCMFs. The cutout box frame color corresponds to the galaxy mass bin to which the cluster belongs (i.e., see titles of the right column plots, and the legend of the top left GCMF plot). The label color indicates which distance bin contains the cluster (i.e., which curve in the right column plots; for bin intervals, see any right column legend). In each cutout, the dashed red circle shows the photometric aperture, whereas the annulus used for sky estimation is marked with dotted silver circles. The angular size of each cutout is 1″. NGC 2903 cluster 4082 looks larger because NGC 2903 is $\gtrsim$2× closer than most of the other galaxies hosting candidate very massive OGCs.

targets) is in basic agreement with the model M31 GC mass distribution of Y. Chen & O. Y. Gnedin (2023) and more generalized TNG50-1 GCMF predictions, but we are insensitive to the low-mass tail of the predicted population. The Y. Chen & O. Y. Gnedin (2023) simulated Milky Way GCMF deviates substantially from our nearby subset of PHANGS galaxies and the two Galactic catalogs (H. Baumgardt & M. Hilker 2018; M. Hilker et al. 2020).

The bottom two panels of Figure 21 illustrate that the form of the PHANGS-HST GCMF above log $M_c/M_\odot \sim 5$ is relatively insensitive to the choice of metallicity (between $Z_\odot/5$ and $Z_\odot/50$), and that the candidate very massive GCs are not a consequence of the particular metallicity assignment for those objects.

Returning to the most massive GCs in a slightly different context, Figure 22 investigates this further by plotting the

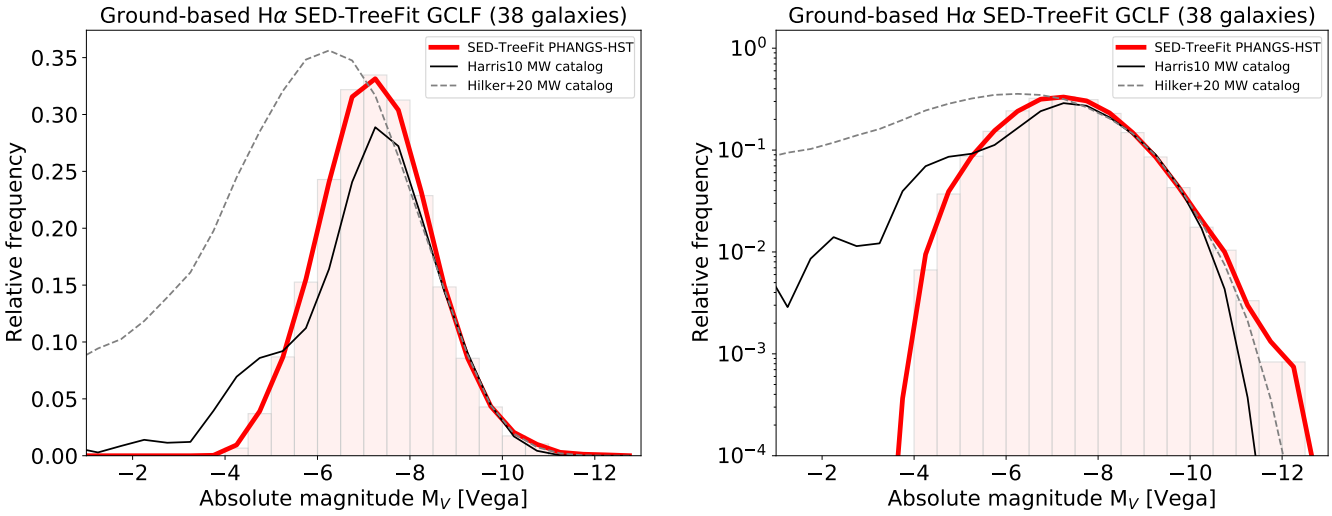

Figure 23. Absolute magnitude (M_V) distribution for GCs in all 38 PHANGS-HST galaxies (red histogram and thick red KDE curve), compared to the analogous distribution for Milky Way GCs (black dashed, unshaded histogram, and black KDE curve) compiled by W. E. Harris (2010). The thin gray dotted curve additionally shows the M. Hilker et al. (2020) sample, which is significantly more inclusive of faint clusters (some nearly invisible against the field). Normalization for the figure uses clusters having $-9.5 < M_V < -8.5$. (Left) Linear y-axis. (Right) Log y-axis, to make differences at the bright end noticeable.

observed GCMF for three bins of galaxy stellar mass (top left), and subsequently for secondary bins of distance within each galaxy mass interval (right column). A montage (lower left) displaying each candidate's very massive GC completes Figure 22. The image cutouts show that these clusters have a very similar color/SED and are confident GCs. We find that all but one of the candidate very massive GCs with log $M_c/M_\odot \geqslant 6.7$ are contained in the most massive disk galaxies (red curve) of the PHANGS-HST sample. The remaining object (NGC 1559 cluster 4121, log $M_c/M_\odot \approx 6.9$) belongs to the intermediate-mass disk galaxy subset (orange curve). The Milky Way (log $(M_*/M_\odot) \sim 10.7$, T. C. Licquia & J. A. Newman 2015) lies effectively between the two higher mass subsets in Figure 22. Thus, the host galaxies of the most massive GCs are typically massive themselves. However, Figure 21 already demonstrated (and the right column of Figure 22 reiterates) that they are also almost exclusively in the more distant PHANGS-HST galaxies. The only nearby ($d < 10$ Mpc) candidate very massive GC is in NGC 2903 (a high-mass galaxy) at a distance of 9.6 Mpc. Since we find a preference for massive and distant hosts, caution in interpretation is warranted, as it is easy to imagine photometric bias linked to increased distance/reduced spatial resolution.

We looked into possible photometric bias carefully. Two main factors could be culprits. First, the aperture size ($r = 4$ WFC3/UVIS pixels) is spatially large at the typical distance of the candidate very massive GCs ($r \approx 15$ pc at $d = 20$ Mpc). Second, environmental confusion affecting the background determination (e.g., via contamination or gradients) is plausible at the sky measurement scale (silver dotted annuli in Figure 22 cutout images). Based on Figure 15 in S. Deger et al. (2022), and inspection of Figure 22, showing that nearby neighbors are not inadvertently included in the aperture, we conclude that aperture size is unlikely to systematically boost the flux for the candidate very massive GCs. The cutouts demonstrate that each aperture (red dashed circle) isolates a single cluster. Although the size of the aperture is fixed in angular extent, our aperture corrections already account for this (S. Deger et al. 2022; J. C. Lee et al. 2022; D. A. Thilker et al. 2022; D. Maschmann et al. 2024), being determined individually per galaxy and decreasing with distance. Five of the nine candidates even contributed specifically to the aperture correction estimate for their host galaxy (except NGC 1365 and NGC 1559). Figure 15 in S. Deger et al. (2022) does reveal random scatter in the aperture corrections at the $\lesssim$0.15 mag level. The possible impact of uncertain background estimation is less significant yet. We recomputed cluster photometry adopting intentional $\pm 3\sigma$ perturbations from our measured sky values, finding that this only produced changes in cluster mass at the few percent level. The objects of interest are bright enough to dominate the sky contribution.

In summary, there is evidence for candidate very massive GCs appearing preferentially in more distant hosts *and* in more massive hosts. We cannot now confidently conclude which galaxy property is responsible, and whether this is just an effect of changing resolution or a real physical trend, although our argument above leans against possible photometric bias. In any case, we stress that the number of objects is small and does not statistically support quantifying any apparent differences between the upper end of the GCMFs presented here. However, a seeming excess linked to higher galaxy mass could be explained either due to size of sample considerations (B. C. Whitmore et al. 2007) (i.e., even if one assumes a universal GCMF shape, lower mass galaxies simply do not contain enough GCs to reliably populate the upper GCMF) or because massive spirals would be expected to have accreted more dwarf galaxies of the variety that could yield Omega Cen analogs. An extensive analysis with more galaxies will be required in the future before a more definitive result can be obtained.

The previous results were all dependent on our SED-fitting outcomes. It is worthwhile to also consider a model-independent perspective (e.g., in terms of absolute magnitude), though we still may optionally rely on fitted ages for GC selection. In Figure 23, we show the distribution of M_V for PHANGS-HST GCs and for the Milky Way population (W. E. Harris 2010). The takeaways from this figure are that the exceptionally massive (bright here) GC objects are still

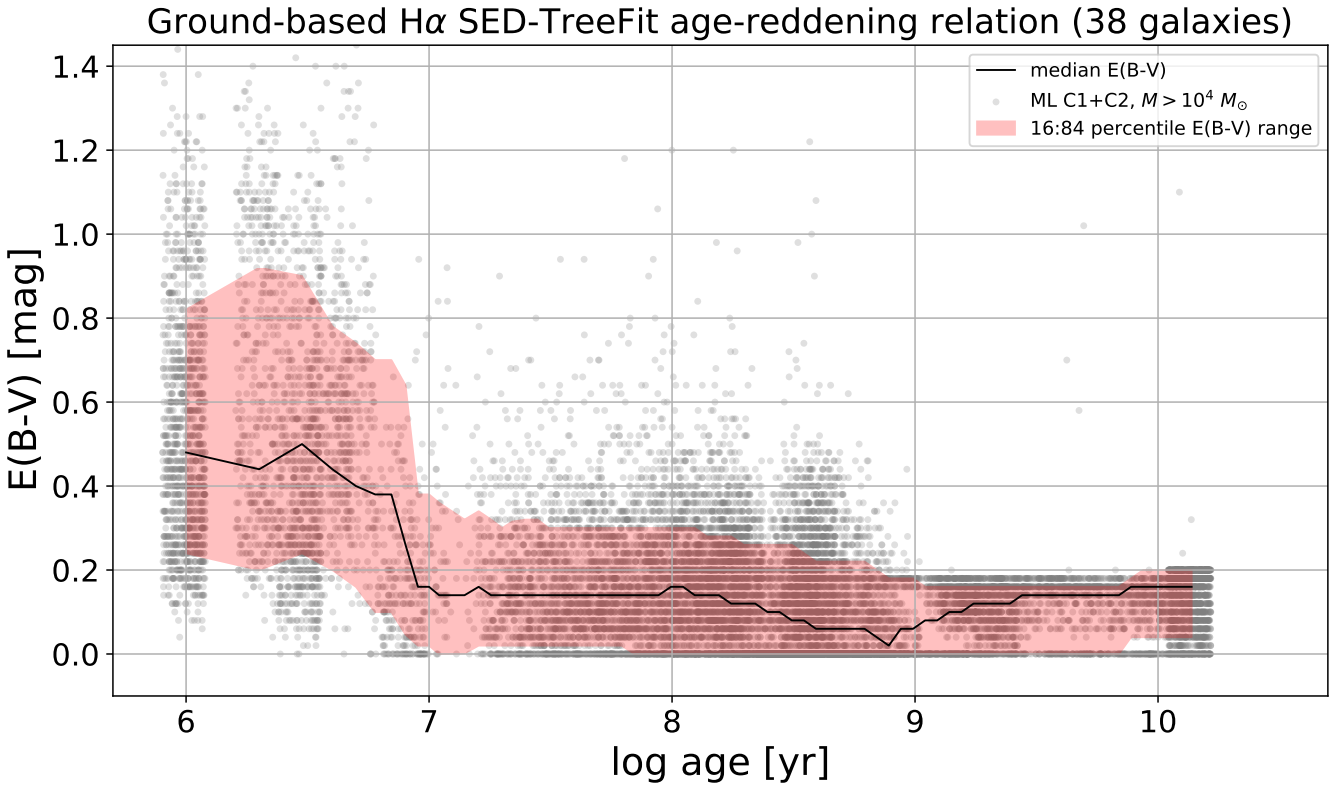

Figure 24. The distribution of reddening, $E(B-V)$, vs. cluster age for all PHANGS-HST galaxies, considering only C1+C2 clusters with mass $\geqslant 10^4\ M_\odot$. In transparent gray, we indicate the 16th–84th percentile range. The median is also shown in black. For visualization purposes, a small amount of random scatter has been applied to the cluster ages. Percentiles were computed before this step.

notable, and that to fairly compare to the Milky Way GC population fainter than the GCLF distribution peak we would need to obtain imaging about $\lesssim$1–2 mag more sensitive for the range of typical distances in the PHANGS-HST sample (though not shown here, this would be especially true if only OGC objects with age $t \geqslant 10$ Gyr were considered).

5.3. Age–Reddening Diagrams

5.3.1. The Decrease of Reddening with Cluster Age

In this section, we quantify the typical reddening $E(B-V)$ as a function of age by aggregating over the entire PHANGS-HST galaxy sample. In Figure 24, we demonstrate that the typical $E(B-V)$ to which C1 and C2 clusters are subject declines from $0.50^{+0.35}_{-0.25}$ mag, at ∼1–4 Myr, to $0.14^{+0.20}_{-0.12}$ mag, by ∼20 Myr, and eventually plateaus at $0.10^{+0.15}_{-0.10}$ mag by the time they are several hundred Myr old. The acceleration of the $E(B-V)$ decline near ∼7–10 Myr is likely related to the artificial age gap that occurs shortly afterward (see Section 5.1.3). When studying Figure 24, remember we impose $E(B-V) \leqslant 0.2$ mag for OGC branch objects that constitute the majority population at $\log t\ \mathrm{yr}^{-1} > 9$. This is justified by the plateauing outcome for General branch objects a bit younger than this. The slight uptick in median $E(B-V)$ with age for OGCs may be caused by our lack of finely sampled metallicity choices in the SSP model library. Similar trends are found whether using age–reddening results from our initial (DR3) SED fitting (not shown) or the new SED-TreeFit (shown in the Figure). The trend of a decreasing $E(B-V)$ with age is also comparable for Class 3 compact associations.

The plot shows slightly lower 84th percentile reddening for 1 Myr versus 2–4 Myr clusters but this is nonphysical and we do not expect the result to be actually true. It is likely an artifact due to the combined consequences of key points (#2) and (#5) discussed in Section 4.6, with (#2) reducing inferred reddening at 1 Myr for some non-YNOs and (#5) permitting some higher $E(B-V)$ values at 2–4 Myr that are a result of unresolved degeneracy. In any case, the overall long-term trend of $E(B-V)$ versus age is robust. It has been previously noted (e.g., Figure 10 in B. C. Whitmore & Q. Zhang 2002), though only for smaller age ranges, and based on a much smaller sample. This result is not surprising and matches expectations for the evolution in local environment from dusty star-forming regions to the diffuse ISM.

5.3.2. Galaxy-specific Age–Reddening Diagrams

Figures 25 and 26 present the age–reddening diagrams for all PHANGS-HST galaxies after applying our improvements to the SED-fitting procedure. The first panel (NGC 1365) includes a diagonal line used in B. C. Whitmore et al. (2023a) to roughly define an upper limit to the reddening as a function of age for a majority of clusters in typical spiral galaxies. The paper advocates the use of this diagonal to check for cases where the age–reddening degeneracy has resulted in large numbers of incorrectly age-dated GCs, which have been given intermediate ages and large values of reddening. We note that this diagonal roughly follows, but is well above, the median reddening trend shown in Figure 24. It is in excellent agreement with the 84th percentile level of $E(B-V)$ we determined across our PHANGS-HST sample. As such, and because it is directly grounded in the data, we adopt the 84th percentile result as a reference curve moving forward, and have added it to all panels of Figures 25 and 26.

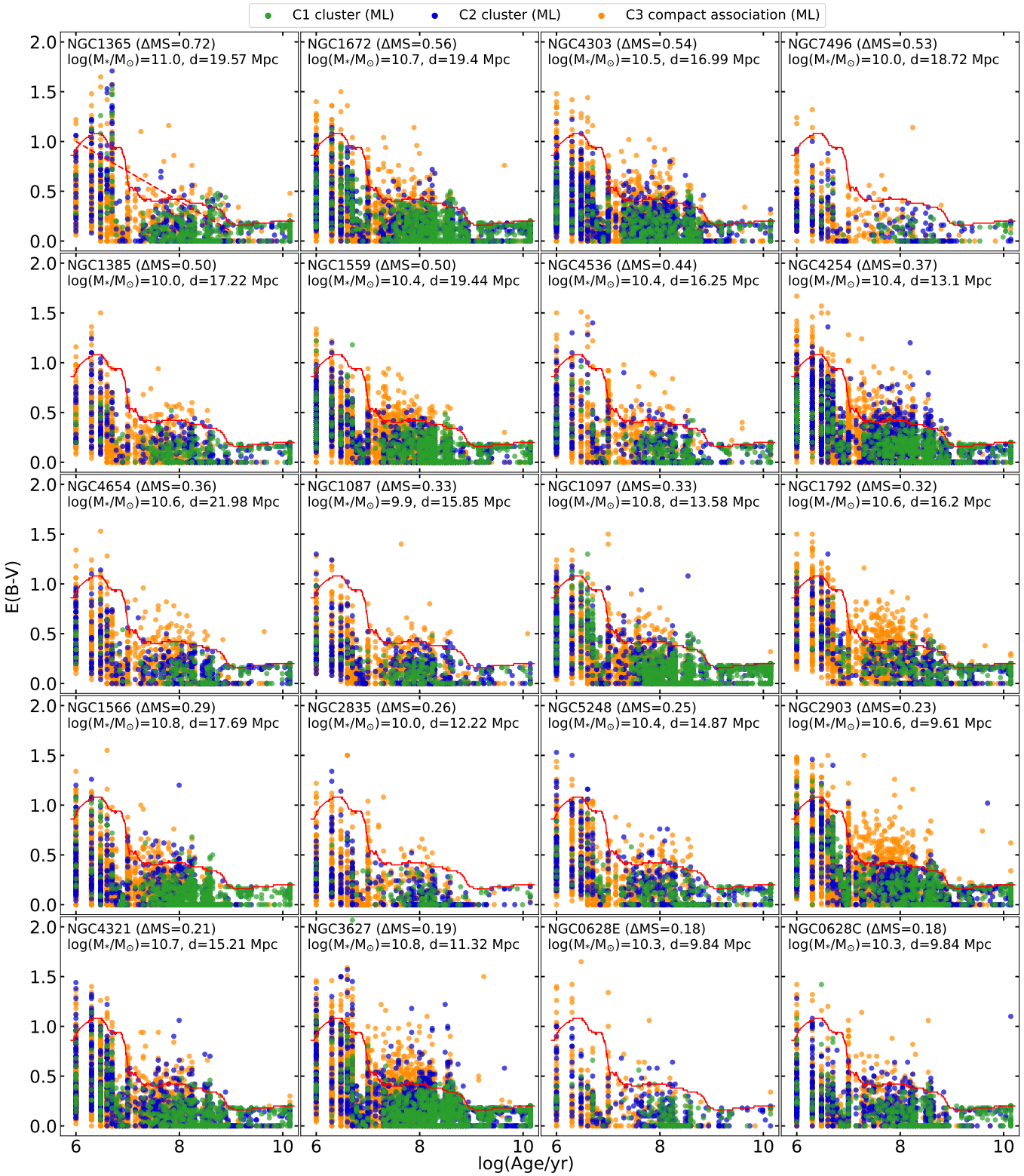

Figure 25. Distribution of reddening and cluster age for all 38 PHANGS-HST galaxies for ML-classified clusters of Class 1 (green), Class 2 (blue), and Class 3 compact associations (orange). The panels are presented in order of decreasing ΔMS. In the first panel only (NGC 1365), the indicative (age, $E(B-V)$) diagonal line from B. C. Whitmore et al. (2023a) is drawn as a dashed red line. For all galaxies, we show the 84th percentile envelope of the aggregated $E(B-V)$ distribution as a function of age, as established in Figure 24, with a solid red curve. Figures 25 and 26 are interactive, allowing one to examine C1+C2+C3 objects jointly (as in the static figure); plus C1-only, C2-only, and C3-only views.

(An animation of this figure is available in the online article.)

If we examine the various galaxies in Figures 25 and 26, we find that the vast majority of the clusters are below the reference curve in most galaxies (by construction). However, this is especially true for galaxies below the galaxy MS, with negative values of ΔMS (e.g., NGC 1317, NGC 1433, NGC 2775, NGC 4548, NGC 4571), and low rates of star formation for their

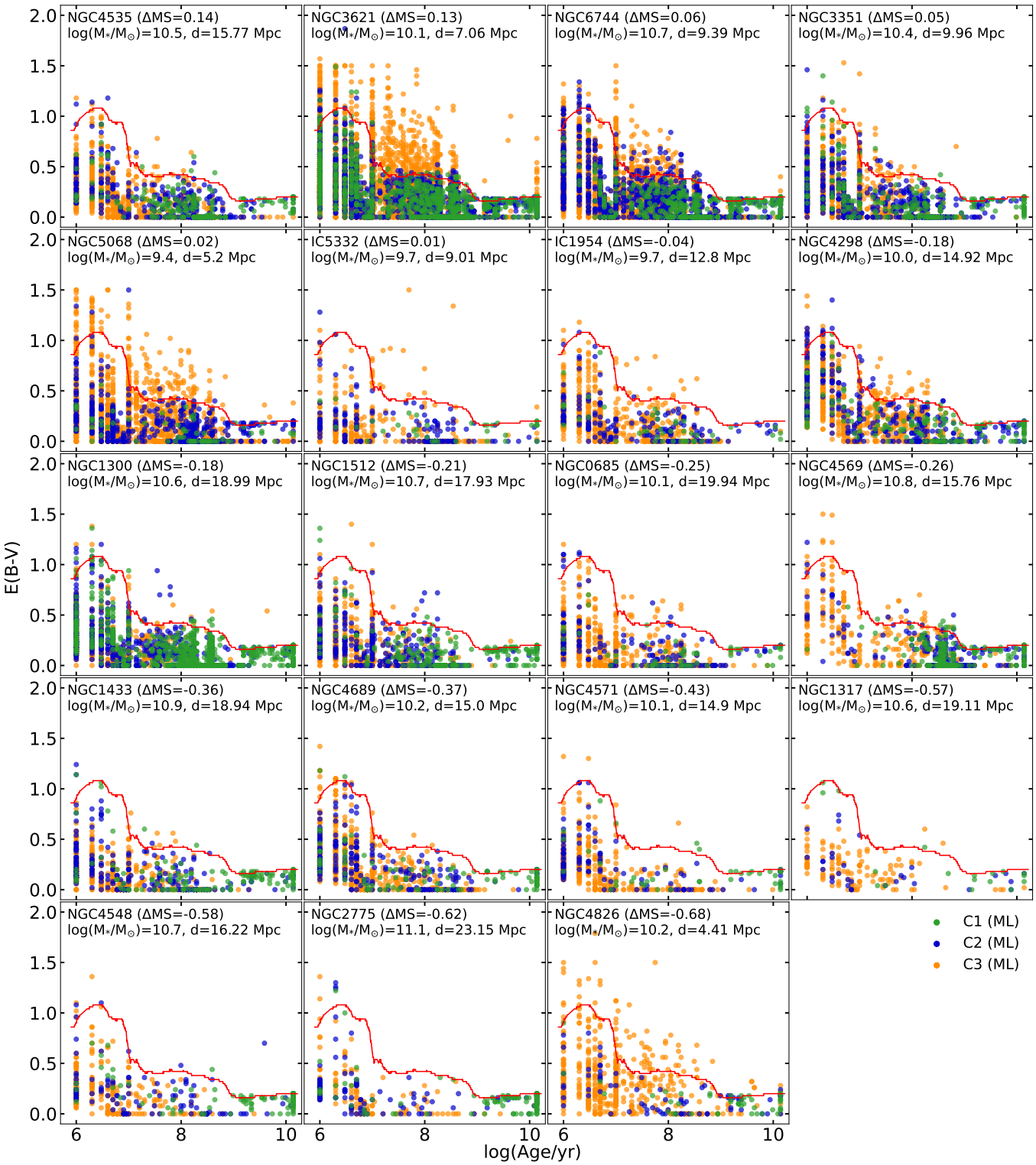

Figure 26. Continuation of Figure 25, with its own animation.
(An animation of this figure is available in the online article.)

mass. Our results show that these galaxies may be characteristically low-reddening environments, even though size-of-sample effects (e.g., D. A. Hunter et al. 2003; B. C. Whitmore et al. 2007) also influence the apparent age–reddening distribution.

We also find this is a good way to identify special cases where there are large numbers of clusters or compact associations above the reference curve. A good example is NGC 4826, the last galaxy in Figure 26. This is sometimes called the "Evil-Eye Galaxy," and is a case where a merger event has thrown up dust in front of a wide range of aging populations (H.-W. R. Rix et al. 1995). A similar situation is shown for NGC 3627, where a merger event (M. P. Haynes

et al. 1979; M. Weżgowiec et al. 2012) appears to have produced a large number of intermediate-age clusters, along with a chaotic dust distribution. Several of the barred galaxies with star-forming central rings also show enhancements in both young super star clusters and intermediate-age clusters (e.g., NGC 1365, NGC 1672, NGC 1097). The "300 Myr" plume population of NGC 1365, discussed in B. C. Whitmore et al. (2023b), is an especially interesting example where the bar produces both the intermediate-age clusters and the dusty ring, which later obscures and reddens the light from the "plume" clusters. Two galaxies have an apparent population of particularly reddened compact associations, which we believe to be spurious and caused by a large number of RSG stars distributed widely throughout the disk. Inspection of our HST imaging showed there are enough such RSGs that random contamination of the compact associations is likely, leading to erroneously high $E(B-V)$ SED-fitting solutions.

5.4. Global Galaxy Properties (i.e., MS) versus Cluster Age–Mass Distribution and Mean Cluster Age

This section explores the dependence of the formation history of the star cluster populations on host galaxy properties. The integrated stellar mass (M_*) and SFR measurements of star-forming galaxies are known to define a clear sequence, the galaxy MS (e.g., J. C. Lee et al. 2007; K. G. Noeske et al. 2007; S. Salim et al. 2007), which evolves with redshift. Figure 27 shows the $z=0$ MS and positions of each PHANGS-HST galaxy in the (M_*, SFR) plane (see Paper I for a description of the details used to produce this particular rendition of the MS). As was done in Paper I, we place a galaxy-specific derived product of our work at the location for each galaxy in this diagram rather than simply a data point. In the case of Paper I, each galaxy was represented by a color–color diagram. Figure 27 instead shows the age–mass distribution for C1 and C2 clusters of each target, rendered as in Figure 17.

A close look at the age–mass distribution renderings in Figure 27 shows systematic trends dependent on galaxy position relative to the MS. For instance, galaxies furthest below the MS (especially NGC 2775, NGC 4548, NGC 4826) all have a strong GC population relative to the number of other clusters, and the intermediate-age population is weak (except for NGC 4826). These galaxies all belong to the bulge-dominated, flocculent and/or quiescent morphological categories as indicated in Table 4 of Paper I. This is consistent with the finding in Paper I that flocculent and quiescent galaxies, where recent star formation has been minimal, had the majority of their star cluster formation earlier in their evolutionary history, resulting in negative MS-residuals (ΔMS, the offset in SFR of the galaxy's position with respect to the MS). The relative prominence of GCs in negative ΔMS galaxies, however, does not mean that other targets do not have GC, only that they do not dominate the observed number of clusters.

A second trend seen in Figure 27 is that for massive spirals on or above the MS (e.g., $\log M_*/M_\odot \gtrsim 10.4$ and $\Delta\mathrm{MS} \approx 0$ or greater) the intermediate-age ($\log\ t\ \mathrm{yr}^{-1} \sim$ 8–9) cluster population dominates, even for galaxies with high recent SFR (such as NGC 1365, NGC 1672, and NGC 4303). This intermediate-age strength is likely indicative of "build up" of an accumulated cluster population surviving from earlier, though not ancient, epochs of active star formation despite continual destruction. Such a large number of not yet disrupted intermediate-age clusters in massive, recently star-forming galaxies is difficult to overwhelm, even by galaxies hosting strong bar- and ring-related current SF (e.g., NGC 1300 and NGC 3351, respectively). A reversal is eventually seen in Figure 27 at the low ($M_*/M_\odot$) half of the PHANGS-HST sampled MS, with many of the age–mass distributions taking on a peanut-like form, having two strong enhancements in cluster counts (both young and intermediate, e.g., IC 5332, IC 1954). This indicates the susceptibility of low M_* to globally relevant starbursts, even those of short duration, similar to the regime of gas-rich dwarf galaxies. Our (M_*, SFR) plane coverage is non-optimal at low M_* (only three galaxies with $\log M_*/M_\odot \leqslant 9.9$, all with $\Delta\mathrm{MS} \sim 0$), hindering the ability to probe the transition to dwarf galaxies or to explore ΔMS dependency for low M_* objects.[46]

Finally, two galaxies are of special note with respect to the relation of galaxy MS position and cluster ensemble properties. NGC 4571 and NGC 4689 are among only a few galaxies for which the young ($\log\ t\ \mathrm{yr}^{-1} \leqslant 7$) cluster population is the strongest of all age demographics. In Figure 27, both galaxies occupy a similar position with respect to the MS, with $\log M_* \sim 10.15$ and $\Delta\mathrm{MS} \sim -0.4$. Both are "anemic" in terms of their H I gas content (J. M. van der Hulst et al. 1987; S. van den Bergh 1991; D. M. Elmegreen et al. 2002; R. A. Koopmann & J. D. P. Kenney 2004) and have been morphologically categorized as flocculent (Paper I). Evidently, the molecular gas that remains in each is presently supporting a low-level SF episode, although at the current rate, this is unlikely to significantly change either galaxy, challenging the notion that a dominant YC population is an indicator of low ΔMS galaxy movement onto and above the MS.

We can quantify the galaxy MS dependence of cluster age–mass distributions visualized in Figure 27 by plotting the mean cluster age versus ΔMS. Such plots are shown in the top panels of Figure 28, for the human catalogs on the left and the ML catalogs on the right. Both catalogs show weak correlations at best, with the star-bursting galaxies having low values of mean age and positive ΔMS.

The bottom panels in Figure 28 show similar plots, but this time using mass-weighted mean age values. These have much stronger correlations, with a Spearman coefficient ~ -0.7. This improvement is probably due to the fact that the highest mass values are generally at the extremes of the age (i.e., OGCs and young super star clusters), which provide the most leverage on the mass-weighted mean age values. Note that the mass-weighted mean age for the galaxies at the high ΔMS end of the correlation is approximately several hundred Myr, an age only slightly older than the timescale of the FUV +MIR SFR tracer used to construct the MS. In all panels of Figure 28 galaxies are marked with symbol type corresponding to their morphological classification from Paper I. We focus on the lower right panel (ML12, mass-weighted) to discuss trends with respect to morphology. It can be seen that having any certain classification does not cleanly predict (ΔMS, mean age) for a galaxy, even if the tendency in the plot is that various classified morphologies most frequently occupy different regimes. For instance, the "SF bar" category (blue squares, union of "bar-driven SF," "central-ring" and "end-of-bar SF" classes in Table 4 of Paper I) typically can

[46] An ongoing Cycle 31 HST Treasury program GO-HST-17502 (P.I. D. Thilker) is adding many more galaxies in this regime.

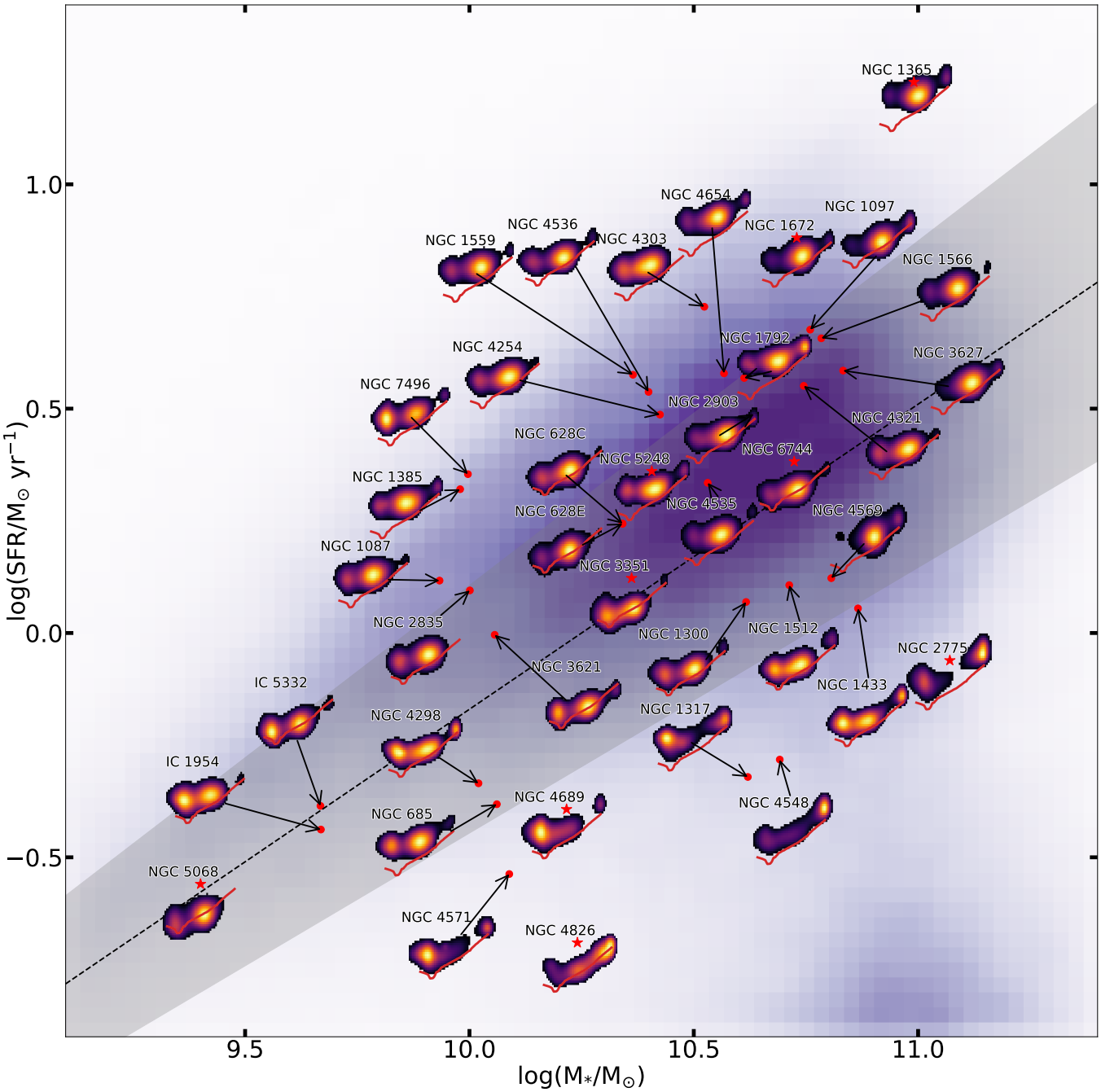

Figure 27. The MS of star-forming galaxies. We represent each galaxy of the PHANGS-HST sample as an age–mass diagram (Figures 19 and 20) at the position on the MS of their host galaxy. The age–mass diagrams are presented in the manner of Figure 17 for the ML catalog of C1 and C2 clusters. As a reference, we show a fixed notional completeness curve ($M_V = -6$) in red for all galaxies. For crowded regions, we shift the age–mass diagrams and denote their position on the MS with a red point and an arrow. For those galaxies that are not in a crowded region, we mark their position on the MS with a red star, situated in the center of the age–mass diagrams. The purple background represents the density of SDSS galaxies of $z < 0.2$ with M_* and SFR values computed by S. Salim et al. (2016). The dashed line is the predicted MS at $z = 0$ defined by A. K. Leroy et al. (2021) and the gray area shows the standard deviation computed by B. Catinella et al. (2018). The essence of this figure is the connection between star formation activity and the cluster population of all PHANGS-HST galaxies. As discussed in the text, the SFRs are sensitive to timescales of <100 Myr and age–mass density of clusters having such ages correlate with the relative position on the MS.

be found at high ΔMS with low mean age, but four of the "SF bar" galaxies are at the low (negative) ΔMS end of the correlation. The still positive, though moderate, ΔMS typical of "global arm" morphologies (orange circles) indicates that spiral arm-dominated SF activity is not the primary driver sending galaxies above the MS, at least for such changes on timescales of $\log t\ \mathrm{yr}^{-1} \lesssim 8$. On longer timescales, given that bars are most frequently associated with spiral arms (and less frequently found in lenticular galaxies), global arm morphology likely plays a bigger role in sustaining galaxies at positive ΔMS. No strong pattern for bulge-hosting galaxies (green stars) is apparent in Figure 28. As we saw earlier in this subsection, lenticular and flocculent (red diamonds) show a strong preference for older cluster populations, quantified here as having mass-weighted cluster ages of $\log t\ \mathrm{yr}^{-1} \gtrsim 9.3$ (2 Gyr).

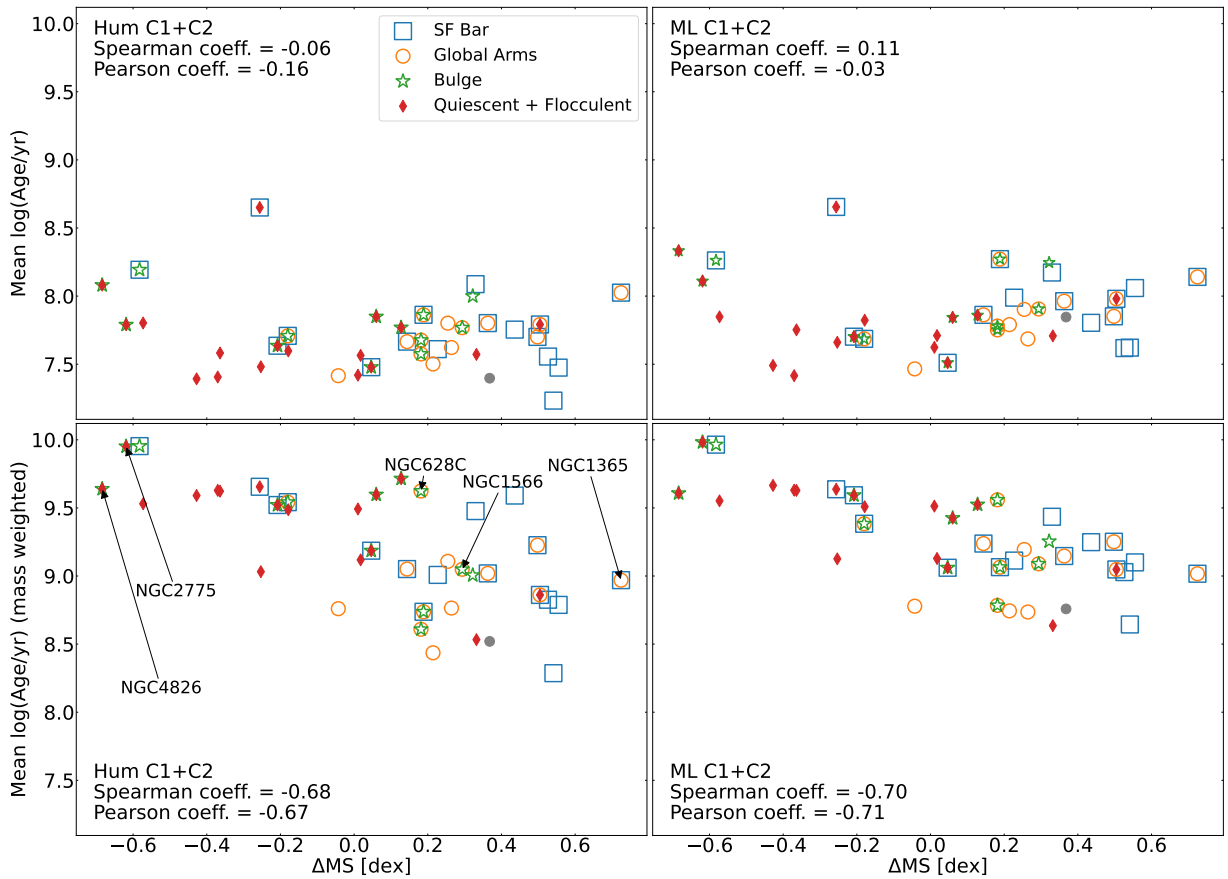

Figure 28. Mean cluster age (upper panels) vs. the offset from the star-forming galaxy MS (ΔMS). A weak correlation is seen for the human C1+C2 catalogs (left), but not for the ML C1+C2 catalogs (right). A much stronger correlation for both the human and ML catalogs is seen when using a mass-weighted mean cluster ages (lower panels). Symbol types encode galaxy characteristics as tabulated in Paper I.

6. Caveats of Our Study and Future Work

6.1. Caveats

To aid the user of our catalogs, this subsection collects all of the important SED-TreeFit caveats previously noted in the paper, with reference to the text location having a full description.

Caution is advised when interpreting the specific distribution of ages for the youngest clusters ($t \leqslant 10$ Myr). Our SED-TreeFit analysis has markedly improved the recovery of the young population but there are still systematic factors that influence the precise age outcomes:

1. Current assumptions with respect to nebular model contributions (e.g., mainly f_{esc}, but also log U and n_e) have enhanced the population of YNO clusters and compact associations given age of $\sim$ 3±1 Myr (Figure 13, see also Sections 4.2, 4.5, and 4.7). We note that studies of the ionized gas properties are expected to improve vastly with the combination of forthcoming HST and JWST emission line imaging.
2. The similarity of 1–3 Myr non-nebular models has resulted in overpopulation of the non-YNO (general grid) clusters assigned an age of 1 Myr, due to a very slight color difference of the 1 Myr model in a direction more consistent with the observed photometry for YCL objects (see also Sections 4.5 and 4.6). In reality, both these excess 1 Myr general grid objects, and the ∼3±1 Myr YNOs discussed immediately above, would be expected to (independently) have a roughly equal distribution in the range 1–3 Myr (perhaps to 4 Myr).
3. We have also identified cases of unresolved degeneracy in which non-YNO objects belonging to the MAP have erroneously been given ages of $\lesssim$4 Myr along with $E(B-V)$ greater than that substantiated by other independent dust/gas tracers (see also Section 4.6). Our current estimate is that this failure mode affects ∼30% of the non-YNO population age dated at $\lesssim$4 Myr (∼20% of the total YNO + general population at these ages). The issue is a topic of continued work. Essentially, the current information guiding SED-TreeFit processing is irrelevant with respect to this challenging case, but some of the ideas in Section 6.2 are thought to hold promise.
4. Our analysis assumes the same near-instantaneous formation history for all objects ($\delta t = 1$ Myr implemented as 10 0.1 Myr bursts in CIGALE). Fully resolved studies of local Milky Way and Magellanic clusters show this is overly simplistic. S. Deger et al. (2022) present evolutionary tracks computed for longer duration starbursts. They are conceivably a better match to our photometry, but would add another free parameter we

sought to avoid at this time. (see also Section 4.1, Table 1)

Despite the issues above, our provided upper and lower limits on age (see top left and top center panels of Figure 30), being estimated according to the manner described in Appendix A, generally bracket the range of viable ages (with the exception of unresolved degeneracies) and should be taken into consideration carefully by users of the catalog during independent analyses.

Cautionary comments related to older populations are also important to reiterate. Generally, they concern particular characteristics of the BC03 model tracks and our choices of metallicity. In particular:

1. Although our current procedure takes the most likely mode of the OGC model grid as the preferred solution (frequently giving GCs an age of 13.75 Gyr), some of these GCs probably have mildly younger ages by a few to several Gyr. This is an instance of the "sweep up" effect discussed in several contexts throughout the paper (see Section 4.6), and, in this specific case, the very slow variation of predicted SED for clusters older than a few Gyr until the track terminus. As above, the upper and lower limits on age (see top right panel of Figure 30) should be used to understand the allowable variation consistent with our photometry.
2. "Gaps" in the age distribution at 10–30 Myr and to a lesser extent at ages between 1–10 Gyr are artificial. The 10–30 Myr gap is probably due to the "bow tie" portion of the BC03 track leading to relative depopulation of ages where redundant choices exist, compounded by limited cases of unresolved degeneracy giving MAP objects ages more appropriate to the YCL. The 1–10 Gyr deficit is a combined result of our two low-metallicity ($Z_{\odot}/5$, $Z_{\odot}/50$) choices rather than a continuum of options, co-alignment of the old track path and the reddening vector in SED (color–color) space, and general age-related dimming leading to nondetection (see also Section 5.1.3 for more details on both gaps).
3. In addition to influencing the estimated age of OGC branch clusters, our two allowed metallicities for such objects clearly also impart additional systematic uncertainty to their mass and reddening determinations. This has not yet been fully explored but should be kept in mind when interpreting GC properties (Section 5.2). Recall that our study was not designed to optimize GC characterization, but rather focuses on younger clusters.

We have demonstrated that the use of HST Hα imaging provides superior SED-TreeFit branch assignment compared to outcomes reliant on ground-based narrowband imaging. The difference is not largely impactful when studying properties of entire cluster and compact association populations (e.g., galaxy-wide, sample-wide), but we emphasize that for single objects the increased resolution of HST can lead to dramatic changes in the estimated physical properties simply due to a different outcome of the first decision point (Hα related, blue circle in Figure 3). In complex, crowded regions (or even simply nearby pairs), we urge the reader to consider seemingly odd or discrepant SED-TreeFit fit results with additional scrutiny. See the full discussion of such issues in the part of Section 4.5 pertaining to NGC 3351.

Another caveat related to the Hα decision point stems from stochastic sampling of the stellar IMF in low-mass clusters. Section 4.5 noted that young, low-mass clusters could occasionally be incorrectly assigned to the OGC branch if they lack an ionizing star and are sufficiently dusty. We quantified the likely degree of such misassignment in two ways. First, the distribution function of CO integrated intensity for OGC branch objects was examined and found to have a noticeable tail to high values, $S(\mathrm{CO}) \gtrsim 80\,\mathrm{K\,km\,s^{-1}}$. The tail contains 101 objects, slightly less than 2% of the OGC branch population. Second, we examined the *UBVI* color–color distribution of general grid (non-YNO) objects given an age $\leqslant$5 Myr and saw a truncation of the YCL traced by this subset of objects at the point where the OGC color–color region is intercepted by a reddening vector extending from the colors of a dust-free 5 Myr cluster. Such a truncation is not seen in the color–color distribution of YNO objects. Using the counts of YNO and non-YNO ($t \leqslant 5$ Myr) clusters both outside and inside the OGC region, we estimate how many non-YNOs could possibly be wrongly assigned as OGCs, finding about 4% at most. These checks lead us to believe that this stochasticity-related classification issue is a minor problem, probably due to the relatively high degree of dust ($A(V) \gtrsim 3$–4 mag) required to redden a VYC all the way into the OGC color–color region. We note in passing that, since we do not fit against stochastically sampled models, the properties of low-mass clusters need improvement in any case, even if they are properly handled by our SED-TreeFit method.

Lastly, we highlight two issues pertaining to PHANGS-HST catalog completeness that have been noted elsewhere (Paper I; D. A. Thilker et al. 2022; M. J. Rodríguez et al. 2023) but are worth repeating:

1. Our current optically selected cluster and compact association catalogs certainly miss a significant population of young embedded and emerging clusters. This is a topic of intense JWST-based study by our group (H. Hassani et al. 2023; M. J. Rodríguez et al. 2023; B. C. Whitmore et al. 2023b; M. J. Rodríguez et al. 2025) and by others (e.g., S. T. Linden et al. 2023; D. Calzetti et al. 2025; B. Gregg et al. 2024; T. McQuaid et al. 2024; A. Pedrini et al. 2024).
2. There is a possibility that we are incomplete with respect to clusters that have particularly small effective radius and therefore appear nearly point-like at the distance of PHANGS-HST galaxies. We attempted to include the massive subset of these as cluster candidates ("super H-D" objects in D. A. Thilker et al. 2022), but they would then be expected to generally only survive human classification (if at all—as they would by their compact nature be disqualified unless some other aspect like their absolute magnitude or potentially impacted environment caught the attention of our expert classifier coauthor B.C. W.). Neural network training samples would certainly not contain enough human-accepted compact clusters to permit them to pass successfully through ML classification as currently implemented.

The caveats recapped above are intended to make the reader aware of the most significant cautionary issues in the context of our current analysis and SED-TreeFit catalogs. Nevertheless, we do advocate the products of our study as a major

step forward in our pursuit of the physical properties of extragalactic clusters and compact associations.

6.2. Future Work

There are a variety of other issues beyond the scope of our analysis that should be kept in mind when using the age, mass, and reddening determinations. Many of these are already discussed in earlier papers, for example, the selection of BC03 SED models rather than other models (e.g., YGGDRASIL—as used in LEGUS) (E. Zackrisson et al. 2011; J. A. Turner et al. 2021) and the effect of stochastic sampling of the IMF for low-mass clusters (M. Fouesneau et al. 2014; M. R. Krumholz et al. 2015a; J. A. Turner et al. 2021; R. Orozco-Duarte et al. 2022; E. R. Stanway & J. J. Eldridge 2023). Other important topics are the inclusion of rotation and binaries (A. Wofford et al. 2016; E. R. Stanway & J. J. Eldridge 2023; M. Lecroq et al. 2024), treatment of AGB stars (E. E. Martínez-García et al. 2021), estimate of Lyman continuum escape fractions (J. W. Teh et al. 2023), and incorporation of pre-main-sequence (PMS) evolutionary phases.[47] Even something as basic as the slope of the reddening vector (i.e., extinction curve), and whether it depends on environment, can have important ramifications for the determinations of age, mass, and reddening. The PHANGS Collaboration is working on all of these topics and more in their effort to continually improve the age dating of clusters and associations.

In our current procedure, we fixed the metallicity of GCs to either $Z_{\odot}/50$ or $Z_{\odot}/5$, with the determination per object depending on the TCI as we defined it in Section 4.4 using the photometry of a Milky Way GC transformed into our HST filter system. In reality, GCs have a range of metallicities (which produces a bimodal color distribution in optical bands). Blindly assuming $Z_{\odot}/50$ would yield a majority of ages older than 10 Gyr, consistent with resolved color–magnitude diagram studies of GCs in the Milky Way (M. Salaris & A. Weiss 2002; D. A. VandenBerg et al. 2013; N. Chehlaeh 2021, and references therein), although ignoring multiple-age populations known to exist in GCs (G. Piotto et al. 2015; N. Bastian & C. Lardo 2018). However, substantially higher metallicity GCs are common (approaching LMC- and SMC-like levels of $Z_{\odot}/2$ and $Z_{\odot}/4$, respectively), in the Milky Way (D. A. VandenBerg et al. 2013) and in other galaxies (W. E. Harris 2023). We note that prior studies of GCs in nearby spiral galaxies have adopted $Z_{\odot}/20$–$Z_{\odot}/50$ (e.g., L. Lomelí-Núñez et al. 2022) but not reaching as high as $Z_{\odot}/5$. When population synthesis models become increasingly available with more choices at intermediate Z, and as we incorporate photometry in other bands (e.g., with JWST or in the FUV), we look forward to attempting actual constraint of photometric GC metallicity. With our present SED-TreeFit implementation, the allowed OGC metallicities can be viewed as effective bookends on the true range, linked to corresponding systematic uncertainty in inferred physical properties.

We have not included any physically motivated functional (e.g., $p_{\rm prior} \propto M^{\beta} t^{\gamma}$ M. R. Krumholz et al. 2015b; J. A. Turner et al. 2021) and/or environmentally dependent (e.g., $p_{\rm prior} \propto \Sigma_{\rm SFR}$ or local sSFR) Bayesian priors in the current study. These will be considered in future studies, but at present, we sought to develop the SED-TreeFit approach on a cluster-by-cluster basis free from the influence of Bayesian priors. That being said, the outcome of our SED-TreeFit analysis could easily be turned around and used to support the future choice of Bayesian priors for cluster mass and age, and implemented within our decision tree SED-fitting framework. In terms of environmentally dependent Bayesian priors, an upcoming effort is to test a spatially variable prior for the allowed reddening or age during the cluster age-dating procedure. Estimates of the CO column density, Balmer decrement, or other ISM tracer at the location of each cluster should provide a sensible constraint on the amount of reddening possible: if the object lies in front of the dust and gas, it will have minimal reddening, and if it is within/behind the detected ISM, the amount of reddening should be roughly proportional to the measured amount of gas and dust. Age priors linked to photometric and structural properties of the local environment could also be a plausible option, since some fraction of field stars and clusters form together and spread out over time. Finally, additional information that could be used to help break the age–reddening degeneracy is the level of pixel-to-pixel surface brightness variations (B. C. Whitmore et al. 2011) and color variations (i.e., color rms) within a cluster. The color rms will increase for ages (5–10 Myr) when RSGs appear, while clusters with ages $\geqslant$100 Myr should have low color rms. The color rms can be calibrated using synthetically created clusters, and potentially help break the degeneracy between reddened clusters that are $\approx$5–10 Myr and those which have little dust and ages of $\approx$10–50 Myr.

Beyond such improved modeling aspects, the incorporation of new observational data (e.g., PHANGS-JWST photometry or limits on Hα flux measured with HST) into our actual fitting (e.g., Paper III, K. F. Henny et al. 2025; B. C. Whitmore et al. 2025) will affect our age-dating procedures in important ways.

As new age estimates become available, they will be publicly released.[48]

7. Summary

In this paper, we describe and apply our new approach for SED fitting to the largest catalog to date of $\sim$100,000 star clusters and compact associations from the PHANGS-HST survey of 38 nearby spiral galaxies. The SED fitting operates on NUV-*U*-*B*-*V*-*I* aperture-corrected photometry. It provides constraints on the age, mass, and reddening, and assumes that sources can be effectively modeled with SSPs.

This "SED-TreeFit" decision tree procedure uses additional information from Hα imaging, location with respect to the spiral arms, morphology of the object (Class 1 or 2 star cluster; Class 3 compact stellar association), and location within the *UBVI* color–color diagram in the context of the three principal features presented in Paper I. These four pieces of information are used to determine whether the object is likely to be a YNO, or an OGC, and these two groups of objects are then fit with different model grids. YNOs are modeled with solar metallicity SSPs with ages $\leqslant$5 Myr that include nebular contributions to broadband flux, and two maximum $E(B-V)$ limits (1.5 mag nominally and 3.0 mag in special cases). OGCs are characterized using either $Z_{\odot}/50$ or $Z_{\odot}/5$ metallicity models with a maximum $E(B-V) = 0.2$ mag. SED fitting for all other objects continues to be based on a

[47] The Sun spends 30 Myr in the Kelvin–Helmholtz contraction phase before H burning sets in. For low-mass stars, this phase can last more than a billion years. So, realistically, also PMS evolutionary phases and the corresponding PMS tracks should be included in the cluster SED-fitting process.

[48] https://archive.stsci.edu/hlsp/phangs/phangs-cat

single grid as presented in J. A. Turner et al. (2021); i.e., solar metallicity, a full range of ages from 1 Myr–13.75 Gyr, and $E(B-V)$ up to 1.5 mag. The adopted ages, masses, and reddenings are derived from the modes of the multivariate probability distribution functions. Overall, the SED-TreeFit procedure assigns ∼14% of the total cluster and compact association population to either the YNO or OGC decision tree branch (21% of C1+C2 clusters, 9% of C3 compact associations).

SED-TreeFit physical parameters are given upper and lower limits determined from the most likely ("best fitting") mode for each object. We use these to understand the effective uncertainty of estimated physical parameters. Our results show that the median age and mass uncertainties clearly depend upon object age, more so than on object mass or distance. The youngest and oldest clusters both have increased uncertainty compared to middle-age clusters. Typical uncertainties at the median distance of our sample for a $\sim 10^4 M_\odot$ cluster with $t \lesssim 3$ Myr reach up to $\pm^{0.4}_{0.2}$ dex in age and up to $\pm^{0.1}_{0.2}$ dex in mass, whereas for a more massive $\sim 10^5\ M_\odot$ cluster with $t > 1$ Gyr uncertainties reach up to $\pm^{0.4}_{0.4}$ dex in age and up to $\pm^{0.2}_{0.2}$ dex in mass. Clusters of intermediate age generally have median age and mass uncertainties approximately $\pm^{0.1}_{0.1}$ dex, with slight age trends seen in Figure 16. The prime reason for increased uncertainty at extreme young and old ages is that models in these regimes have very similar SED shapes with little color variation ($t \lesssim 3$ Myr ⇒ uniformly blue; $t > 1$ Gyr ⇒ uniformly red). An additional factor that raises uncertainties is the frequently complex path of the cluster evolutionary track. We emphasize that the uncertainties quoted above are still underestimated, as they should also account for systematic factors such as the true accuracy of the tracks, assumptions for CIGALE modeling, and SED-TreeFit methodology-related choices.

A summary of our scientific findings is as follows:

1. The ages from our method are key for uncovering the true population of massive GCs. The new ages result in a 550% increase in old massive GCs with $\log M_c/M_\odot \geqslant 5$. ∼90% of the GC population is identified as such due to revised ages. Past analyses often misclassified these clusters as young due to large age uncertainties resulting from the degeneracy between age, metallicity, and reddening, as discussed by S. Hannon et al. (2022), B. C. Whitmore et al. (2023a).
2. Clusters with ages revised downward to $t \leqslant 10$ Myr comprise ∼25% of the population above $M_c = 5 \times 10^4\ M_\odot$. However, twice as many clusters were reclassified from young to older ages, leading to an overall 19% decrease in clusters younger than 10 Myr. Future studies will assess the impact of such changes on age distribution functions. Because of the bidirectional age flow described above, we expect significant adjustment of the age function slope in both young and intermediate-age regimes.
3. The SED-TreeFit ages show that only about one-eighth of the PHANGS-HST galaxies have formed optically selected candidate YMCs with $\gtrsim 10^6\ M_\odot$, with generally only a few to several per galaxy (e.g., NGC 1097, NGC 1672, NGC 2903, NGC 3627, which have 3, 3, 2, and 2, respectively). NGC 1365 is an exception as it contains nine candidate YMCs. Table 4 provides these object counts. However, the census of YMCs (of $\gtrsim 10^6\ M_\odot$ and slightly less massive ones described immediately below) may still be incomplete due to dust and limited spatial resolution—see the last two points of Section 6.1.
4. Clusters of age $\leqslant 10$ Myr with masses $\approx 10^5\ M_\odot$ are common, and form in most galaxies (∼70%) except the least massive, most quiescent systems. Our current results suggest that the most massive YCs (previous paragraph) may be subject to relatively severe destruction, as their analogs are found in much reduced numbers at intermediate age. For context, see previous works regarding cluster destruction by B. C. Whitmore et al. (2007), S. M. Fall & R. Chandar (2012), N. Bastian et al. (2012), and M. R. Krumholz et al. (2019).
5. The sample contains a small number of GCs significantly more massive ($\log M/M_\odot \gtrsim 6.8 - 7.1$) than those found in the Milky Way population, all in galaxies more massive than the Milky Way. This is likely a size-of-sample consequence (B. C. Whitmore et al. 2007; D. A. Hunter et al. 2003). Within the errors due to the low number of candidate very massive GCs, the form of the PHANGS-HST GCMF is in rough agreement with the simulated M31 GC mass distribution of Y. Chen & O. Y. Gnedin (2023) and the more general TNG50-1 (J. E. Doppel et al. 2023) prediction.
6. We quantify the decline in reddening with cluster age: the typical $E(B-V)$ for C1 and C2 clusters decreases from $0.50^{+0.35}_{-0.25}$ mag, at ∼1–4 Myr, to $0.14^{+0.20}_{-0.12}$ mag, by ∼20 Myr, and eventually plateaus at $0.10^{+0.15}_{-0.10}$ mag for ages of several hundred Myr and higher.
7. Age–mass diagrams and age–reddening diagrams are presented for each of the 38 galaxies in the sample, as well as for the cluster population aggregated over the entire survey. Features in the cluster age–mass diagram are correlated with the position of the galaxy along the galaxy MS and reinforce the conclusions from Paper I based on analysis of the color–color diagrams. The mean mass-weighted cluster age of a galaxy decreases with decreasing ΔMS, demonstrating that the star cluster formation history tracks the overall SFH of the galaxy, in spite of significant cluster destruction.

The new procedures presented here address two critical shortcomings of common SED-fitting approaches employing SSP models: (1) the use of $Z_\odot$ models to fit the entire cluster population of a galaxy, which results in an underestimate of the ages of OGCs by a factor of 10 or more; and (2) the inability of broadband HST UV-optical photometry to directly break the age–reddening degeneracy, which in many cases previously led to catastrophic errors in the ages of the youngest dusty clusters and old clusters with minimal dust. Future work will continue to improve upon the SED-fitting and parameter estimation. The most important upcoming work, which will provide improved observational constraints, is to replace the ground-based Hα imaging (∼1.″2 resolution) with Hα imaging from HST (0.″08 resolution) for the complete galaxy sample, to add PHANGS-JWST NIRCam photometry, and incorporate independent constraints on the dust reddening, from the ratio of Paα (JWST) to Hα (HST), Balmer line ratios from MUSE, and dust maps from JWST MIRI and ALMA CO (2–1).

Acknowledgments

We dedicate this paper to the memory of Julie Whitmore (1954 January 13–2023 August 23).

J.C.L. is enormously grateful to Michele Judd, Janet Seid, and the W.M. Keck Institute for Space Studies (KISS) at Caltech for its sustained support of collaboration meetings where key work for this paper was performed, and for providing a quiet space for J.C.L. to think. The PHANGS-HST survey benefited from early discussions between J.C.L., A..L, and other current PHANGS team members, which date back to the 2014 KISS workshop, "Bridging the Gap: Observations and Theory of Star Formation Meet on Large and Small Scales."

R.C.L. acknowledges support for this work provided by a National Science Foundation (NSF) Astronomy and Astrophysics Postdoctoral Fellowship under award AST-2102625.

M.B. gratefully acknowledges support from the ANID BASAL project FB210003 and from the FONDECYT regular grant 1211000.

This work was supported by the French government through the France 2030 investment plan managed by the National Research Agency (ANR), as part of the Initiative of Excellence of Université Côte d'Azur under reference number ANR-15-IDEX-01.

K.G. is supported by the Australian Research Council through the Discovery Early Career Researcher Award (DECRA) Fellowship (project No. DE220100766) funded by the Australian Government. K.G. is supported by the Australian Research Council Centre of Excellence for All Sky Astrophysics in 3 Dimensions (ASTRO 3D), through project No. CE170100013.

A.W. acknowledges UNAM's DGAPA for the support in carrying out her sabbatical stay at UCSD, USA, through the PASPA program.

This work is based on observations made with the NASA/ESA Hubble Space Telescope (program Nos. 15654 and 17126) and NASA/ESA/CSA James Webb Space Telescope (program No. 2107). The data were obtained from the Mikulski Archive for Space Telescopes at the Space Telescope Science Institute, which is operated by the Association of Universities for Research in Astronomy, Inc., under NASA contract 5-26555 for HST and NAS 5-03127 for JWST.

Data Availability

The PHANGS-HST star cluster catalogs will be made publicly available through the Mikulski Archive for Space Telescopes (MAST)[49] at doi:10.17909/jray-9798. PHANGS-HST data products are available via MAST[50] doi:10.17909/t9-r08f-dq31.

Software: DOLPHOT (v2.0; A. Dolphin 2016), CIGALE (D. Burgarella et al. 2005; S. Noll et al. 2009; M. Boquien et al. 2019).

Appendix A
Peak Extraction from Multimodal PDFs, Estimation of Parameter Uncertainties

The distribution of likelihoods in age and $E(B-V)$ from CIGALE reflects the discrete nature of the adopted model libraries, complicating the task of identifying the number and properties of significant modes. For instance, the step size in $E(B-V)$ [0.01] is small enough that a peak finder algorithm frequently returns nearly adjacent peaks that should really be considered as equivalent. Therefore, we smooth the nominally returned CIGALE 2D probability distribution function (PDF) using a Gaussian kernel with FWHM equal to three steps along both axes, taking special care not to artificially down-weight the edges of the grid. After smoothing, we then identify any well-defined modes using PHOTUTILS/SOURCEFINDER (L. Bradley 2023) to segment the (age, $E(B-V)$) PDF. For each of these modes, we record the age, reddening, and associated stellar mass, taking the parameters linked to the pixel having the highest likelihood in the segment.

Once all modes and their associated physical parameters have been identified, we threshold the PDF segment of each mode in each of the SED-TreeFit model grids at the 50% level with respect to its peak. This operation yields a set of (age, $E(B-V)$) pairs for which the observations are consistent with the model library at a level comparable to, but slightly less than, the mode's peak model. Each of these solutions has an associated stellar mass. For the subset of models distinguished in this way, for each mode, we adopt the minimum and maximum value of age, $E(B-V)$, and mass belonging to the ensemble as lower and upper limits on the determined physical parameters. Figure 29 illustrates this limit determination procedure for a single cluster. Our limits account for the covariance between age and $E(B-V)$ that can still remain within a single mode (e.g., peaks in the PDF are generally elongated). For this reason, we believe the tabulated lower and upper limits are a conservative choice. They are often asymmetric about the mode's assigned peak value. Figure 30 illustrates the limits for each SED-TreeFit parameter as a function of the most likely value, separately for each of the three decision tree branch populations.

[49] https://archive.stsci.edu/hlsp/phangs/phangs-cat
[50] https://archive.stsci.edu/hlsp/phangs/phangs-hst

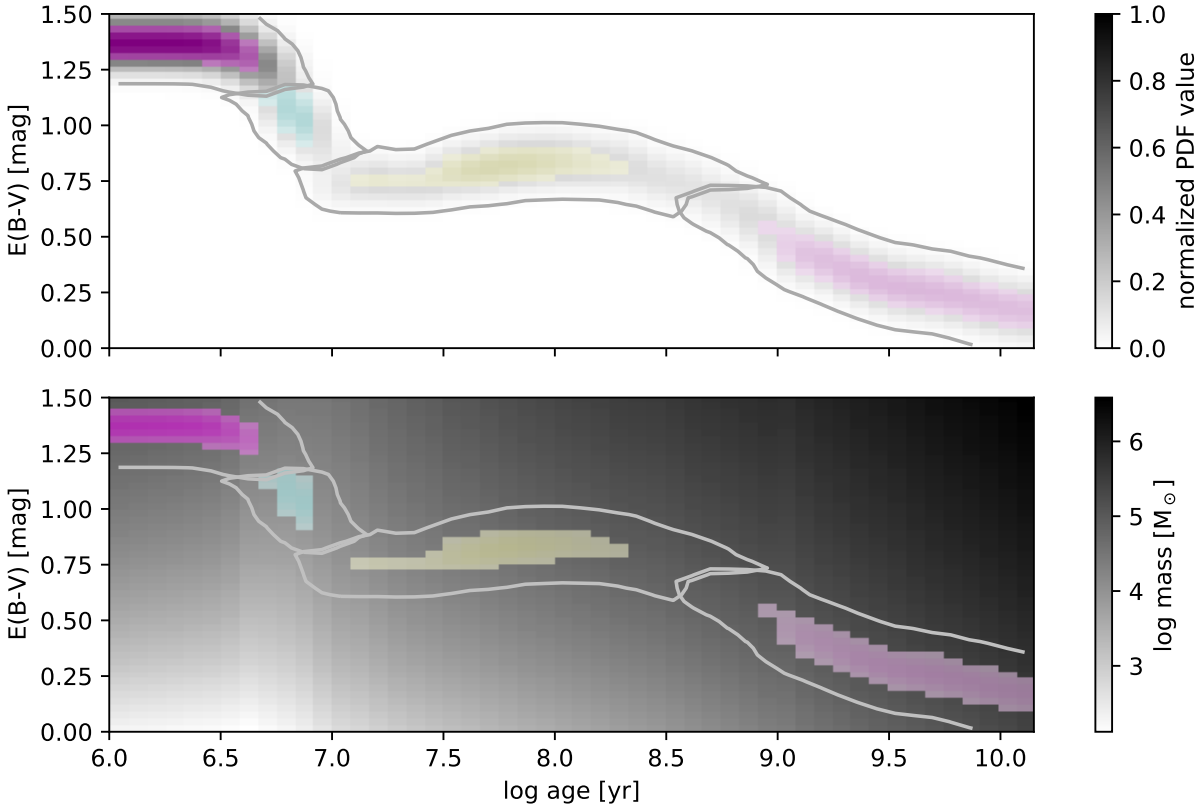

Figure 29. Illustration of the upper and lower physical parameter limit determination procedure using CIGALE outputs. (Top) 2D probability distribution function for a highly multimodal cluster, showing normalized probability vs. (age, $E(B-V)$). Each identified mode (and its segment in the PDF) is surrounded by a single contour. Using color highlighting, we indicate the pixels of each segment with a value greater than 50% of the mode peak. As described in the text, this set of pixels (each associated with a mode of given age and reddening) is used as the basis for setting upper and lower limits on age and $E(B-V)$, by recording the extrema in each set. (Bottom) The values of stellar mass vs. (age, $E(B-V)$). CIGALE computes a stellar mass for each model considered in the SED fitting. With the pixel sets of the top panel, we are able to tabulate the maximum and minimum stellar mass to be used as limits for each mode.

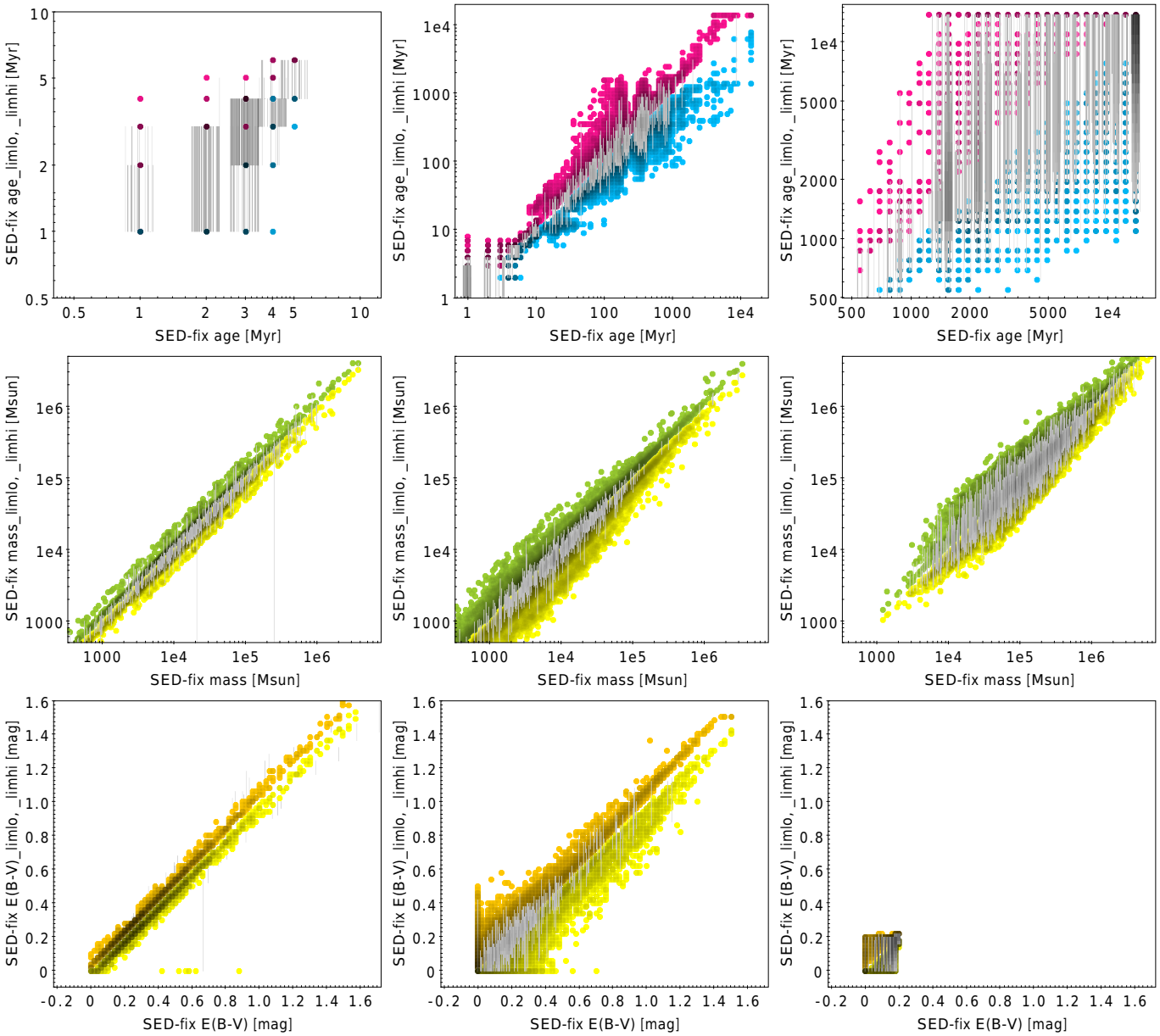

Figure 30. Upper limit, lower limit values (colored points) determined as shown in Figure 29 vs. the SED-TreeFit age, mass, and $E(B-V)$. In each panel, a random subset of the clusters is shown as lines connecting their upper and lower limit values. (Left column) Objects in the YNO branch. (Middle column) Objects in the standard branch. (Right) Objects in the OGC branch. Note that the axis limits change for the different branch populations in the case of age (top row).

Appendix B
How Do We Determine whether a Source Has Hα Emission?

We use narrowband Hα images, available from ground-based observations for all 38 PHANGS-HST galaxies, and from HST for a subset of 17 galaxies, to identify whether an object will enter the YNO or OGC branch. In this appendix, we describe the steps used to associate Hα emission with a given source for this purpose.

B.1. Narrowband Data

B.1.1. PHANGS-HST Hα Imaging

We are in the process of obtaining HST Hα imaging for all PHANGS galaxies, but as of the writing of this paper, only a subset of these data have been acquired and fully processed. R. Chandar et al. (2025) describe the PHANGS-HST Hα survey, including data sets from (HST-GO-17126, HST-GO-17502, HST-GO-17457), with complete details on the WFC3/UVIS observations, stellar continuum-subtraction method, flux anchoring, and [N II]-contamination correction using PHANGS-MUSE IFU spectroscopy. A sampling of initial science applications is also provided. One of these applications is developed further by A. T. Barnes et al. (2025, in preparation), who present a study of HST-detected substructure within H II regions identified previously from PHANGS-MUSE observations (B. Groves et al. 2023). We use the products of R. Chandar et al. (2025) in our SED-TreeFit analysis for the 17 galaxies that are currently available (18 targets, because NGC 628c and NGC 628e fields are kept separate due to a filter difference). These galaxies span the entire range of distance in our full sample, and thus can be

used to foresee the improvements in our SED-TreeFit results that will soon become available after our HST Hα observations are completed over the upcoming year.

B.1.2. PHANGS Ground-based Hα Imaging

Hα imaging from ground-based observatories is available for all 38 galaxies in the present sample. For 33 galaxies, narrowband images were taken with the Wide-Field Imager on the ESO/MPG 2.2 m telescope at European Southern Observatory (La Silla) and the DirectCCD on the du Pont 2.5 m telescope at Las Campanas Observatory (A. Razza et al. 2025, in preparation). Hα images for four other galaxies (NGC 1097, NGC 3621, NGC 4536, NGC 4826) are available from the SINGS project (Spitzer Infrared Nearby Galaxies Survey, R. C. Kennicutt et al. 2003), through IRSA, and for NGC 2903 from C. G. Hoopes et al. (2001). In cases where the narrowband filter includes flux from the [N II] 6548 Å, [N II] 6583Å lines, we have estimated and removed their contribution (see A. Razza et al. 2025, in preparation for details). The median resolution of the images is ≈1″. This corresponds to scales of ∼20–110 pc for the distance range spanned by our PHANGS-HST galaxy sample. The ground-based Hα observations have lower resolution (by a factor of ∼10) than the HST images, but as clusters tend to form near one another, the ground-based observations should capture most recently formed clusters associated with line emission, whereas additional SED-TreeFit decision point criteria help identify those mistakenly passed into the start of the YNO branch.

B.2. Removal of Diffuse Hα Background with Constrained Diffusion Decomposition

To prepare our Hα imaging specifically for the SED-TreeFit analysis, we first remove diffuse emission and segment each galaxy into a conservatively defined set of H II emitting clumps. DIG is known to contribute approximately 50% of the Hα luminosity in typical star-forming galaxies (A. M. N. Ferguson et al. 1996; D. A. Thilker et al. 2002; M. S. Oey et al. 2007; F. Belfiore et al. 2022), but cannot be uniquely linked back to a specific ionizing cluster or association. The removal of diffuse line emission distributed over spatial scales large compared to our resolution limit (or alternatively with respect to the physically compact H II clumps resolved by HST) is accomplished (see Figure 31) using a multiscale decomposition technique pioneered by G.-X. Li (2022, called constrained diffusion decomposition or CDD). The goal of the CDD method is similar to that of wavelet-based decomposition analysis in the sense that the emission contained within the original image is divided up into a set of single-scale images, each containing substructures with power over a narrow range of scales. CDD improves upon wavelet analysis via the elimination of negative artifacts around and in between positive features. The complete set of CDD single-scale images is flux-conserving; addition of them all (plus a residual component larger than all requested scales) returns the original image. We modified the original CDD algorithm to operate using a ladder of specific spatial scales, rather than a ladder of pixel scales (as the code was published). Specifically, we adopt scales given by $s = 2^n$ pc where $n = 0$, 0.5, 1, 1.5, 2, ... up to a maximum scale of $s = 128$ pc, and with the minimum scale dependent upon the combination of resolution and galaxy distance. The background-subtracted image at a given scale is obtained by adding up single-scale images only up to the targeted transition scale between "clumpy" and "diffuse" regimes. For our targets and Hα observations with HST, we were able to reach down to a limit between ∼3 and 11 pc ($2^{1.5}$–$2^{3.5}$ pc). We adopted 11 pc uniformly across all 17 HST Hα-available galaxies. Similarly, we used 91 pc ($2^{6.5}$ pc) for ground-based Hα imaging of the full 38 galaxy sample.

With the background-removed Hα images (Figure 31), we then undertake segmentation of clumpy, localized substructures. In brief, the method first evaluates the positionally dependent rms and intensity level of the image using PHOTUTILS/BACKGROUND2D (L. Bradley 2023), over a grid of square bins 7 times larger in dimension than the targeted CDD scale from above. The rms results are used to generate a SNR map of the clumpy substructures, whereas tracking of the Background2D-determined intensity level permits implementing a small SNR correction for any remaining diffuse flux (CDD is not perfect in the presence of noise). Next, the SNR map is segmented/deblended into H II clumps using PHOTUTILS/SOURCEFINDER (L. Bradley 2023), adopting a minimum SNR of 3 for a pixel to be included in a clump. Note that we do not refer to the H II clumps as proper "H II regions," nor do we produce a catalog here. Our processing yields regions of Hα emission with an elevated SFR surface density in the ground-based data, or regions of likely local photoionization in the HST Hα data. In both cases, the presumption is that such regions are where young ionizing clusters should be present.

We utilize a combination of segment-agnostic circular aperture photometry on the background-removed Hα images and the H II clump segments to determine whether any given object should be considered as having physically linked nebular emission. Our conservative criteria are intended to prevent overassignment of the objects to the YNO branch, given that the SED-TreeFit age prior used for YNO objects is quite severe (1–5 Myr). The following two subsections describe our methodology.

B.3. Criteria for Associating Localized Hα Emission with a Given Source

Owing to the morphological cues they embody, especially for high-resolution HST Hα SED-TreeFit processing, H II clump segments are able to provide strong evidence for the association of an object with locally ionized nebulae. For all objects in the catalogs of Paper I, we evaluate a Boolean metric to assess this, adopting the union of three quasi-independent object(cluster/compact association)-versus-H II segment conditions as our indicator of meaningful linkage. The three conditions are: (1) is the object centered within a segment? (2) Is the maximum intensity position of any segment within the PHANGS-HST photometric aperture of the object, e.g., closer than 4 WFC3/UVIS 0.″03962 pixels? Or (3) is the photometric aperture more than 50% covered by one or more segments? If any of these conditions is satisfied, we consider the object to have a tentative nebular confirmation ("HαUnion"==True in our internal working tables).

B.4. Determination of Hα Surface Brightness Threshold

Our Hα segmentation parameters are set uniformly across the PHANGS-HST galaxy sample and without specific optimization to changing environmental morphology of the ionized gas. Because of this, and the desire to remain conservative regarding

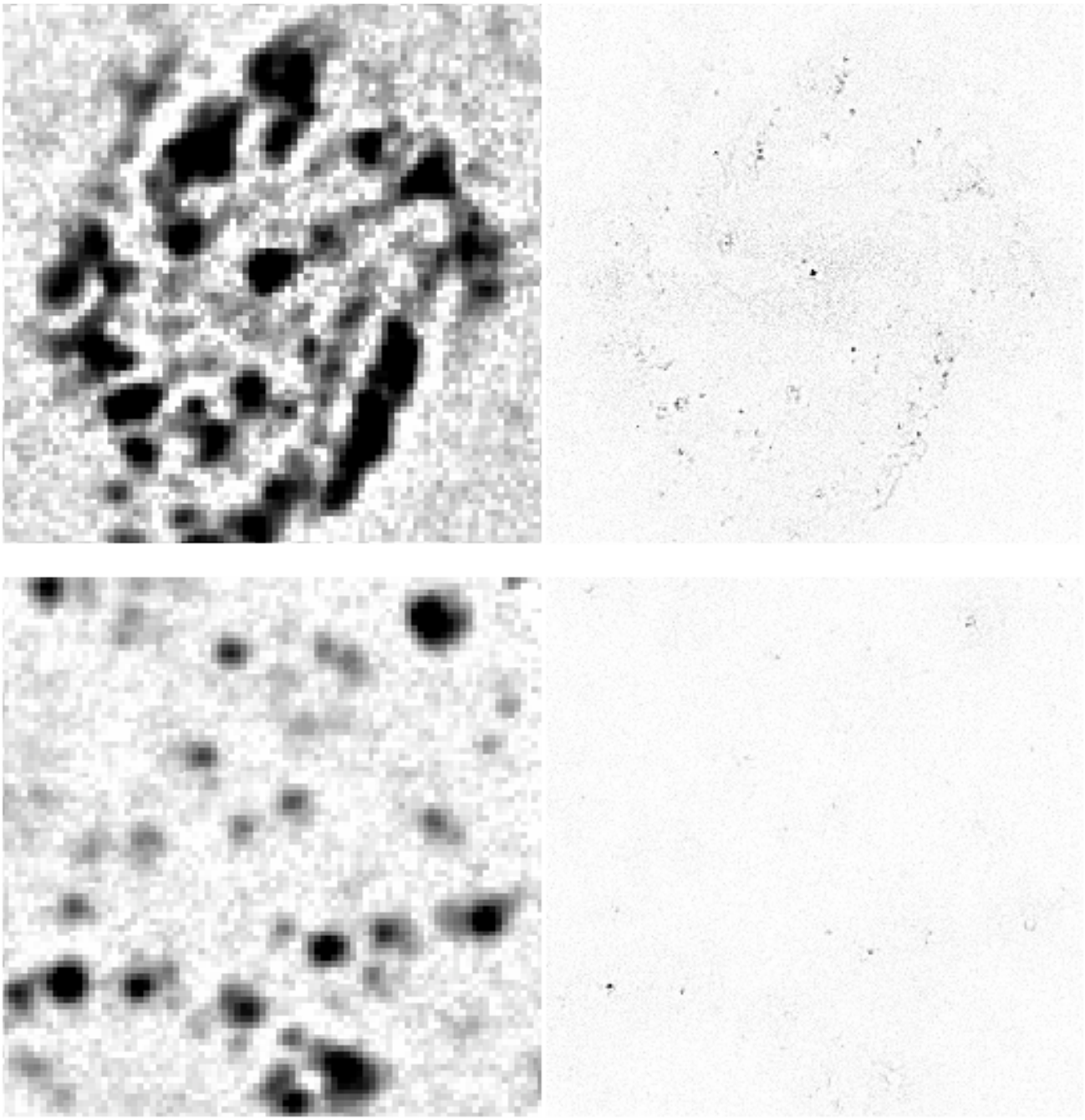

Figure 31. Influence of spatial resolution on Hα surface brightness measurement. We show two portions of NGC 4321 after removal of diffuse emission: the central star-forming ring (top) and a more quiescent region of the southeast spiral arm (bottom). Processed versions (following Appendix B.2) of ground-based (left) and HST (right) continuum-subtracted Hα imaging are shown. Each plot spans 3.5 kpc top to bottom.

YNO branch assignment, we further restrict the selection of objects that are deemed to have localized Hα emission by enforcing a surface brightness threshold that clusters or compact associations having tentative nebular linkages (Appendix B.3) must exceed to be fully accepted.

Surface brightness measurements for this purpose were obtained by evaluating the average of the background-removed Hα intensity $S(\mathrm{H}\alpha)_{\mathrm{bkgdsub}}$ within the PHANGS-HST photometric apertures. In the case of the ground-based narrowband imaging, this effectively reduces to sampling the intensity in a single Hα pixel at the position of the source.

We sought to use these Hα surface brightness measurements in a manner that was maximally equivalent between ground-based and HST-based Hα implementations of the SED-TreeFit decision nodes. Figure 32 presents paired $S(\mathrm{H}\alpha)_{\mathrm{bkgdsub}}$ measurements for all 17 galaxies having both Hα data sets. In these plots, we color-code the symbol markers according to whether a point is a C1, C2, or C3 ML object with HαUnion==True: for HST-only (blue), for ground-based-only (red), or for both (purple). Visible cyan markers correspond to cluster candidates and confirmed C1, C2, and C3 objects with HαUnion==False according to both HST and ground-based assessments. Several horizontal and

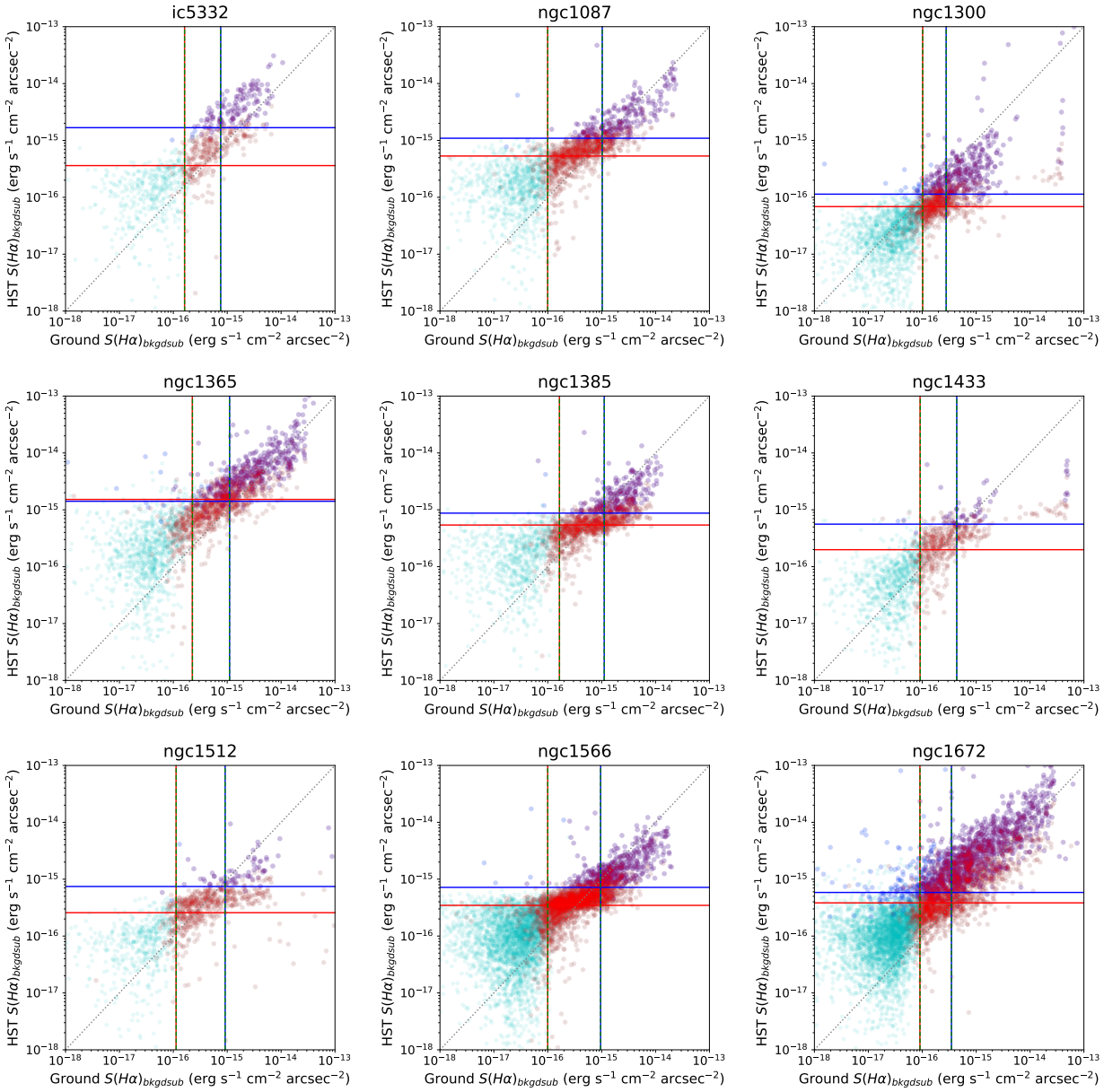

Figure 32. HST and ground-based Hα local background subtracted surface brightness levels ($S(\mathrm{H}\alpha)_{\mathrm{bkgdsub}}$) for all candidates (cyan), for those with HαUnion$_{\mathrm{HST}}$==True (blue), and for those with HαUnion$_{\mathrm{ground-based}}$==True (red). The HαUnion flag indicates if a source meets any of the criteria for locally associated Hα emission outlined in Appendix B.3. The horizontal and vertical lines mark the various $S(\mathrm{H}\alpha)_{\mathrm{bkgdsub}}$ threshold values described fully in the text. We determined them based on selected percentiles of the $S(\mathrm{H}\alpha)_{\mathrm{bkgdsub}}$ values for sets of candidates that were either doubly confirmed as sources having associated Hα (and thus both HαUnion flags set as True) or doubly rejected (both HαUnion flags set as False) with respect to Hα with HST and ground-based imaging. In particular, the horizontal blue line in each panel is the adopted HST $S(\mathrm{H}\alpha)_{\mathrm{bkgdsub}}$ threshold, which varies from galaxy to galaxy, adapting to changes in sensitivity and Hα morphology across the sample. Conversely, for the reasons given in the text, we eventually adopted a fixed $S(\mathrm{H}\alpha)_{\mathrm{bkgdsub}}$ threshold (8.4×10^{-16} erg s^{-1} cm^{-2} arcsec^{-2}) for ground-based Hα SED-TreeFit processing.

vertical lines are shown in each plot. These indicate different possible $S(\mathrm{H}\alpha)_{\mathrm{bkgdsub}}$ threshold values, determined on the basis of guidance from the distribution of sources doubly confirmed as HαUnion==True (purple) or doubly disqualified via HαUnion==False (cyan). Red (and red–green dashed) lines are more tolerant of faint $S(\mathrm{H}\alpha)_{\mathrm{bkgdsub}}$ as they are gauged via doubly False outcome agreement, whereas blue (and blue–green dashed) are more restrictive as they are set by doubly True outcome agreement. Specifically, per galaxy, we determine the HST $S(\mathrm{H}\alpha)_{\mathrm{bkgdsub}}$ threshold (blue horizontal line) as corresponding to the 5th percentile of HST surface brightness values in the doubly True subsample. The vertical blue line was initially set in an analogous manner, but based on ground-based measurements instead of HST based. However, this would erroneously accept a large set of ground-based measurements occupying the portion of the plot just slightly below and right of the intersection of blue lines—i.e., objects not corroborated by HST Hα at higher resolution. Therefore, in preparing to adopt a ground-based $S(\mathrm{H}\alpha)_{\mathrm{bkgdsub}}$ threshold we tested the 25th percentile rather than the 5th percentile. However, not all our galaxies have both HST and ground-based Hα imaging, so a solution was needed that required only ground-based measurements. With this restriction, but wanting the guidance from galaxies having both data sets, we first thought to iteratively determine the percentile level of the

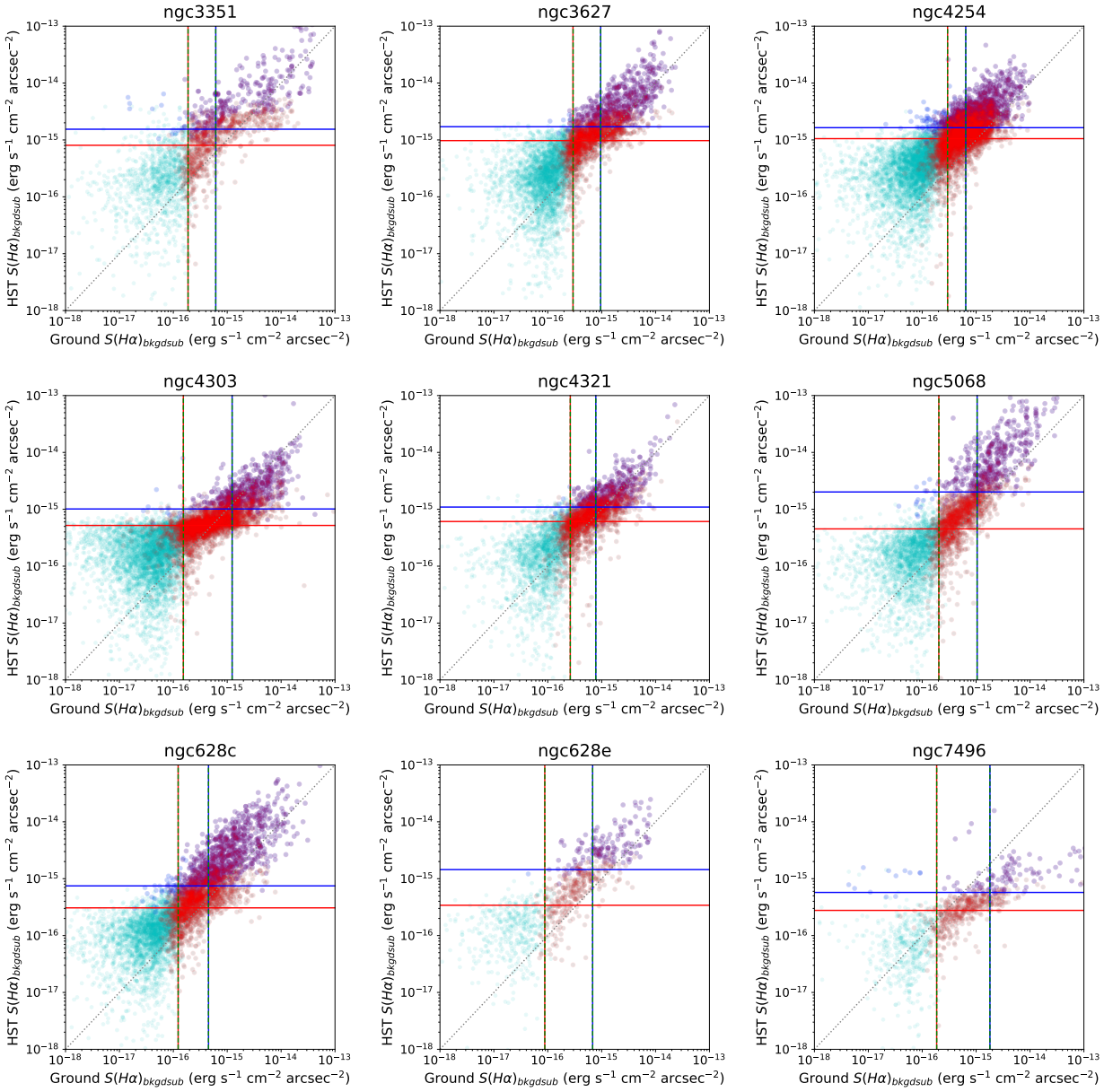

Figure 32. (Continued.)

ground-based HαUnion==True surface brightnesses that corresponded to the 25th percentile in the doubly True sources and then use a typical value of that percentile across the board. Because the $\sim$1″ resolution leads to HαUnion==True more easily, such percentiles ended up being significantly higher (43rd to 77th percentiles, green vertical dashed lines) and we noted considerable variation galaxy to galaxy. This ultimately convinced us to simply adopt a single fixed $S(\mathrm{H}\alpha)_{\mathrm{bkgdsub}}$ threshold in the ground-based context, chosen as the median of the 25th percentile doubly True source ground-based levels. This was found to be 8.4×10^{-16} erg s^{-1} cm^{-2} arcsec^{-2}. Satisfied with this solution, we did not further explore thresholds driven by a doubly HαUnion==False set of sources (red lines), though they are retained in the plots for illustration. For instance, the relative ratio of restrictive (blue) and inclusive (red) thresholds for HST Hα-based work is 2 to 3. Analogous ratios for ground-based work are larger, perhaps indicating increased fidelity in HST Hα for this metric.

Summarizing, any source that has a tentative nebular confirmation ("HαUnion"==True) and also exceeds the Hα surface brightness threshold is confirmed to have locally associated Hα emission ("PHANGS_HALPHA_PASS_FLAG"==True in our internal tables), and would therefore pass the first node into the YNO branch. Refer to Section 4.3 for higher-level considerations pertaining to the YNO branch. Due to slight differences in imaging footprint for Hα imaging (ground-based and from HST) and the HST broadband data sets used to originally construct our cluster catalogs, a tiny fraction of objects could not be evaluated for significant, localized Hα. These are indicated in our released tables (Table 2) with PHANGS_HALPHA_EVAL_FLAG == False.

Appendix C
Environmental Masks

We utilize binary masks delineating spiral arm structures in our PHANGS-HST galaxies. These masks were created by

M. Querejeta et al. (2021) as part of a broader study examining the dependence of molecular gas properties and star formation activity as a function of subgalactic environment. Although masks are available for many stellar structures (centers, bars, spiral arms, interarm regions, discs without strong spirals, rings, and lenses), we only utilized the spiral arms in our work. However, not all of the PHANGS-HST galaxies have spiral arm structures defined in these masks. During mask preparation by M. Querejeta et al. (2021), the choice was made to only include well-delineated spiral arms able to be followed across most of the galaxy disk. Particularly, in some multi-armed/flocculent spirals, the distinction between arm and interarm would have become increasingly arbitrary. For spirals that are included, a log-spiral function is fitted to bright regions along arms on the near-IR images, and assigned an empirically determined width based on CO emission in PHANGS-ALMA images (A. K. Leroy et al. 2021). For galaxies in the Spitzer Survey of Stellar Structure in Galaxies (S^4G), M. Querejeta et al. (2021) mostly followed H. Salo et al. (2015) and M. Herrera-Endoqui et al. (2015). For the remaining galaxies, the environmental masks rely on measurements from the literature and new fits to IRAC 3.6 μm images. All of the environmental masks are publicly available at the Canadian Advanced Network for Astronomy Research storage system.[51]

ORCID iDs

David A. Thilker https://orcid.org/0000-0002-8528-7340
Janice C. Lee https://orcid.org/0000-0002-2278-9407
Bradley C. Whitmore https://orcid.org/0000-0002-3784-7032
Daniel Maschmann https://orcid.org/0000-0001-6038-9511
Kiana Henny https://orcid.org/0000-0001-7448-1749
Rupali Chandar https://orcid.org/0000-0003-0085-4623
Daniel A. Dale https://orcid.org/0000-0002-5782-9093
Sinan Deger https://orcid.org/0000-0003-1943-723X
Médéric Boquien https://orcid.org/0000-0003-0946-6176
Aida Wofford https://orcid.org/0000-0001-8289-3428
Leonardo Úbeda https://orcid.org/0000-0001-7130-2880
Alessandro Razza https://orcid.org/0000-0001-7876-1713
Ashley T. Barnes https://orcid.org/0000-0003-0410-4504
Francesco Belfiore https://orcid.org/0000-0002-2545-5752
Frank Bigiel https://orcid.org/0000-0003-0166-9745
Kathryn Grasha https://orcid.org/0000-0002-3247-5321
Brent Groves https://orcid.org/0000-0002-9768-0246
Hwihyun Kim https://orcid.org/0000-0003-4770-688X
Ralf S. Klessen https://orcid.org/0000-0002-0560-3172
Justus Neumann https://orcid.org/0000-0002-3289-8914
Francesca Pinna https://orcid.org/0000-0001-5965-3530
M. Jimena Rodríguez https://orcid.org/0000-0002-0579-6613
Erik Rosolowsky https://orcid.org/0000-0002-5204-2259
Eva Schinnerer https://orcid.org/0000-0002-3933-7677
Thomas G. Williams https://orcid.org/0000-0002-0012-2142

References

Adamo, A., Östlin, G., Zackrisson, E., et al. 2010, MNRAS, 407, 870
Adamo, A., Ryon, J. E., Messa, M., et al. 2017, ApJ, 841, 131
Adamo, A., Zeidler, P., Kruijssen, J. M. D., et al. 2020, SSRv, 216, 69
Anand, G. S., Lee, J. C., Van Dyk, S. D., et al. 2021, MNRAS, 501, 3621
Anderson, J., & van der Marel, R. P. 2010, ApJ, 710, 1032
Ashworth, G., Fumagalli, M., Krumholz, M. R., et al. 2017, MNRAS, 469, 2464
Astronomical Society of South Africa (ASSA) 2008, MNSSA, 67, 82
Bañares-Hernández, A., Calore, F., Camalich, J. M., & Read, J. I. 2025, A&A, 693, A104
Barnes, A. T., Chandar, R., Kreckel, K., et al. 2022, A&A, 662, L6
Barnes, A. T., Glover, S. C. O., Kreckel, K., et al. 2021, MNRAS, 508, 5362
Barth, A. J., Ho, L. C., Filippenko, A. V., Sargent, W. L., et al. 1995, AJ, 110, 1009
Bastian, N., Adamo, A., Gieles, M., et al. 2012, MNRAS, 419, 2606
Bastian, N., & Lardo, C. 2018, ARA&A, 56, 83
Baumgardt, H., & Hilker, M. 2018, MNRAS, 478, 1520
Baumgardt, H., Hilker, M., Sollima, A., & Bellini, A. 2019a, MNRAS, 482, 5138
Baumgardt, H., He, C., Sweet, S. M., et al. 2019b, MNRAS, 488, 5340
Belfiore, F., Santoro, F., Groves, B., et al. 2022, A&A, 659, A26
Boquien, M., Burgarella, D., Roehlly, Y., et al. 2019, A&A, 622, A103
Boselli, A., Boissier, S., Cortese, L., et al. 2006, ApJ, 651, 811
Bradley, L. 2023, astropy/photutils: v1.8.0, Zenodo, doi:10.5281/ZENODO.7946442
Brodie, J. P., & Strader, J. 2006, ARA&A, 44, 193
Bruzual, G., & Charlot, S. 2003, MNRAS, 344, 1000
Burgarella, D., Buat, V., & Iglesias-Páramo, J. 2005, MNRAS, 360, 1413
Byler, N., Dalcanton, J. J., Conroy, C., & Johnson, B. D. 2017, ApJ, 840, 44
Calzetti, D., Adamo, A., Linden, S. T., et al. 2025, A&A, 693, A104
Calzetti, D., Lee, J. C., Sabbi, E., et al. 2015, AJ, 149, 51
Cardelli, J. A., Clayton, G. C., & Mathis, J. S. 1989, ApJ, 345, 245
Catinella, B., Saintonge, A., Janowiecki, S., et al. 2018, MNRAS, 476, 875
Chabrier, G. 2003, PASP, 115, 763
Chandar, R., Barnes, A. T., Thilker, D. A., et al. 2025, AJ, 169, 150
Chandar, R., Caputo, M., Mok, A., et al. 2023, ApJ, 949, 116
Chandar, R., Fall, S. M., Whitmore, B. C., & Mulia, A. J. 2017, ApJ, 849, 128
Chandar, R., Whitmore, B. C., Kim, H., et al. 2010, ApJ, 719, 966
Chehlaeh, N. 2021, JPhCS, 2145, 012004
Chen, Y., & Gnedin, O. Y. 2023, MNRAS,
Chernoff, D. F., & Weinberg, M. D. 1990, ApJ, 351, 121
Chevance, M., Kruijssen, J. M. D., Krumholz, M. R., et al. 2022, MNRAS, 509, 272
Conroy, C. 2013, ARA&A, 51, 393
Dalcanton, J. J., Williams, B. F., Lang, D., et al. 2012, ApJS, 200, 18
Deger, S., Lee, J. C., Whitmore, B. C., et al. 2022, MNRAS, 510, 32
Della Bruna, L., Adamo, A., McLeod, A. F., et al. 2022, A&A, 666, A29
Dolphin, A. 2016, DOLPHOT: Stellar Photometry, Astrophysics Source Code Library, ascl:1608.013
Doppel, J. E., Sales, L. V., Nelson, D., et al. 2023, MNRAS, 518, 2453
D'Souza, R., & Rix, H.-W. 2013, MNRAS, 429, 1887
Egorov, O. V., Kreckel, K., Glover, S. C. O., et al. 2023, A&A, 678, A153
Elmegreen, D. M., Elmegreen, B. G., Frogel, J. A., et al. 2002, AJ, 124, 777
Emsellem, E., Schinnerer, E., Santoro, F., et al. 2022, A&A, 659, A191
Fall, S. M., & Chandar, R. 2012, ApJ, 752, 96
Fall, S. M., & Zhang, Q. 2001, ApJ, 561, 751
Ferguson, A. M. N., Wyse, R. F. G., Gallagher, J. S. I., & Hunter, D. A. 1996, AJ, 111, 2265
Floyd, M., Chandar, R., Whitmore, B. C., et al. 2024, AJ, 167, 95
Fouesneau, M., Johnson, L. C., Weisz, D. R., et al. 2014, ApJ, 786, 117
Grasha, K., Calzetti, D., Adamo, A., et al. 2017a, ApJ, 840, 113
Grasha, K., Calzetti, D., Adamo, A., et al. 2019, MNRAS, 483, 4707
Grasha, K., Calzetti, D., Bittle, L., et al. 2018, MNRAS, 481, 1016
Grasha, K., Elmegreen, B. G., Calzetti, D., et al. 2017b, ApJ, 842, 25
Gratton, R., Bragaglia, A., Carretta, E., et al. 2019, A&ARv, 27, 8
Gregg, B., Calzetti, D., Adamo, A., et al. 2024, ApJ, 971, 115
Groves, B., Kreckel, K., Santoro, F., et al. 2023, MNRAS, 520, 4902
Häberle, M., Neumayer, N., Seth, A., et al. 2024, Natur, 631, 285
Hannon, S., Lee, J. C., Whitmore, B. C., et al. 2019, MNRAS, 490, 4648
Hannon, S., Lee, J. C., Whitmore, B. C., et al. 2022, MNRAS, 512, 1294
Hannon, S., Whitmore, B. C., Lee, J. C., et al. 2023, MNRAS, 526, 2991
Harris, W. E. 2010, arXiv:1012.3224
Harris, W. E. 2023, ApJS, 265, 9
Hartman, K., & Harris, W. E. 2024, AJ, 168, 75
Hassani, H., Rosolowsky, E., Koch, E. W., et al. 2024, ApJS, 271, 2
Hassani, H., Rosolowsky, E., Leroy, A. K., et al. 2023, ApJL, 944, L21
Haynes, M. P., Giovanelli, R., & Roberts, M. S. 1979, ApJ, 229, 83
Henny, K. F., Dale, D., Chandar, R., et al. 2025, ApJ, in press

[51] https://www.canfar.net/storage/vault/list/phangs/RELEASES/PHANGS_env_masks

Herrera-Endoqui, M., Díaz-García, S., Laurikainen, E., & Salo, H. 2015, A&A, 582, A86
Hilker, M., Baumgardt, H., Sollima, A., & Bellini, A. 2020, in IAU Symp. 351, Star Clusters: From the Milky Way to the Early Universe, ed. A. Bragaglia et al. (Cambridge: Cambridge Univ. Press), 451
Hoopes, C. G., Walterbos, R. A. M., & Bothun, G. D. 2001, ApJ, 559, 878
Hunter, D. A., Elmegreen, B. G., Dupuy, T. J., & Mortonson, M. 2003, AJ, 126, 1836
Jordán, A., McLaughlin, D. E., Côté, P., et al. 2007, ApJS, 171, 101
Kennicutt, R. C., Jr., Armus, L., Bendo, G., et al. 2003, PASP, 115, 928
Kim, J., Chevance, M., Kruijssen, J. M. D., et al. 2023, ApJL, 944, L20
Koopmann, R. A., & Kenney, J. D. P. 2004, ApJ, 613, 866
Krumholz, M. R., Adamo, A., Fumagalli, M., et al. 2015b, ApJ, 812, 147
Krumholz, M. R., Fumagalli, M., da Silva, R. L., Rendahl, T., & Parra, J. 2015a, MNRAS, 452, 1447
Krumholz, M. R., McKee, C. F., & Bland -Hawthorn, J. 2019, ARA&A, 57, 227
Lacchin, E., Mastrobuono-Battisti, A., Calura, F., et al. 2024, A&A, 681, A45
Larsen, S. S., & Richtler, T. 1999, A&A, 345, 59
Larson, K. L., Lee, J. C., Thilker, D. A., et al. 2023, MNRAS, 523, 6061
Lecroq, M., Charlot, S., Bressan, A., et al. 2024, MNRAS, 527, 9480
Lee, J. C., Kennicutt, R. C., Funes, J. G., Sakai, S., Akiyama, S., et al. 2007, ApJL, 671, L113
Lee, J. C., Sandstrom, K. M., Leroy, A. K., et al. 2023, ApJL, 944, L17
Lee, J. C., Whitmore, B. C., Thilker, D. A., et al. 2022, ApJS, 258, 10
Leroy, A. K., Schinnerer, E., Hughes, A., et al. 2021, ApJS, 257, 43
Li, G.-X. 2022, ApJS, 259, 59
Licquia, T. C., & Newman, J. A. 2015, ApJ, 806, 96
Linden, S. T., Evans, A. S., Armus, L., et al. 2023, ApJL, 944, L55
Linden, S. T., Evans, A. S., Rich, J., et al. 2017, ApJ, 843, 91
Lomelí-Núñez, L., Mayya, Y. D., Rodríguez-Merino, L. H., Ovando, P. A., & Rosa-González, D. 2022, MNRAS, 509, 180
Martínez-García, E. E., Bruzual, G., González-López lira, R. A., & Rodríguez-Merino, L. H. 2021, ApJ, 908, 110
Maschmann, D., Lee, J. C., Thilker, D. A., et al. 2024, ApJS, 273, 14
McQuaid, T., Calzetti, D., Linden, S. T., et al. 2024, ApJ, 967, 102
Mok, A., Chandar, R., & Fall, S. M. 2019, ApJ, 872, 93
Moustakas, J., Kennicutt, R. C., Jr., Tremonti, C. A., et al. 2010, ApJS, 190, 233
Noeske, K. G., Weiner, B. J., Faber, S. M., et al. 2007, ApJL, 660, L43
Noll, S., Burgarella, D., Giovannoli, E., et al. 2009, A&A, 507, 1793
Noyola, E., Gebhardt, K., & Bergmann, M. 2008, ApJ, 676, 1008
Noyola, E., Gebhardt, K., Kissler-Patig, M., et al. 2010, ApJL, 719, L60
O'Connell, R. W., Gallagher, J. S., Hunter, D. A., et al. 1994, ApJ, 433, 65
Oestlin, G., Bergvall, N., & Roennback, J. 1998, A&A, 335, 85
Oey, M. S., Meurer, G. R., Yelda, S., et al. 2007, ApJ, 661, 801
Orozco-Duarte, R., Wofford, A., Vidal-García, A., et al. 2022, MNRAS, 509, 522
Pedrini, A., Adamo, A., Calzetti, D., et al. 2024, ApJ, 971, 32
Piotto, G., Milone, A. P., Bedin, L. R., et al. 2015, AJ, 149, 91
Querejeta, M., Schinnerer, E., Meidt, S., et al. 2021, A&A, 656, A133
Rix, H.-W. R., Kennicutt, R. C., Jr., Braun, R., Walterbos, R. A. M., et al. 1995, ApJ, 438, 155
Rodríguez, M. J., Lee, J. C., Indebetouw, R., et al. 2025, ApJ, 983, 137
Rodríguez, M. J., Lee, J. C., Whitmore, B. C., et al. 2023, ApJL, 944, L26
Salaris, M., & Weiss, A. 2002, A&A, 388, 492
Salim, S., Lee, J. C., Janowiecki, S., et al. 2016, ApJS, 227, 2
Salim, S., Rich, R. M., Charlot, S., et al. 2007, ApJS, 173, 267
Salo, H., Laurikainen, E., Laine, J., et al. 2015, ApJS, 219, 4
Scheuermann, F., Kreckel, K., Barnes, A. T., et al. 2023, MNRAS, 522, 2369
Skillman, E. D., Kennicutt, R. C., Jr., Shields, G. A., Zaritsky, D., et al. 1996, ApJ, 462, 147
Spitzer, L., Jr., & Harm, R. 1958, ApJ, 127, 544
Stanway, E. R., & Eldridge, J. J. 2023, MNRAS, 522, 4430
Sun, J., Leroy, A. K., Rosolowsky, E., et al. 2022, AJ, 164, 43
Teh, J. W., Grasha, K., Krumholz, M. R., et al. 2023, MNRAS, 524, 1191
Thilker, D. A., Walterbos, R. A. M., Braun, R., & Hoopes, C. G. 2002, AJ, 124, 3118
Thilker, D. A., Whitmore, B. C., Lee, J. C., et al. 2022, MNRAS, 509, 4094
Turner, J. A., Dale, D. A., Lee, J. C., et al. 2021, MNRAS, 502, 1366
van den Bergh, S. 1991, PASP, 103, 390
van der Hulst, J. M., Skillman, E. D., Kennicutt, R. C., & Bothun, G. D. 1987, A&A, 177, 63
van der Marel, R. P., & Anderson, J. 2010, ApJ, 710, 1063
VandenBerg, D. A., Brogaard, K., Leaman, R., & Casagrande, L. 2013, ApJ, 775, 134
Wei, W., Huerta, E. A., Whitmore, B. C., et al. 2020, MNRAS, 493, 3178
Wężgowiec, M., Soida, M., & Bomans, D. J. 2012, A&A, 544, A113
Whitmore, B. C., Allam, S. S., Budavári, T., et al. 2016, AJ, 151, 134
Whitmore, B. C., Brogan, C., Chandar, R., et al. 2014, ApJ, 795, 156
Whitmore, B. C., Chandar, R., Lee, J. C., et al. 2025, ApJ, 982, 50
Whitmore, B. C., Chandar, R., & Fall, S. M. 2007, AJ, 133, 1067
Whitmore, B. C., Chandar, R., Kim, H., et al. 2011, ApJ, 729, 78
Whitmore, B. C., Chandar, R., Lee, J., et al. 2020, ApJ, 889, 154
Whitmore, B. C., Chandar, R., Lee, J. C., et al. 2023a, MNRAS, 520, 63
Whitmore, B. C., Chandar, R., Rodríguez, M. J., et al. 2023b, ApJL, 944, L14
Whitmore, B. C., Chandar, R., Schweizer, F., et al. 2010, AJ, 140, 75
Whitmore, B. C., Lee, J. C., Chandar, R., et al. 2021, MNRAS, 506, 5294
Whitmore, B. C., Schweizer, F., Leitherer, C., Borne, K., & Robert, C. 1993, AJ, 106, 1354
Whitmore, B. C., Sparks, W. B., Lucas, R. A., Macchetto, F. D., & Biretta, J. A. 1995, ApJL, 454, L73
Whitmore, B. C., & Zhang, Q. 2002, AJ, 124, 1418
Whitmore, B. C., Zhang, Q., Leitherer, C., et al. 1999, AJ, 118, 1551
Wofford, A., Charlot, S., Bruzual, G., et al. 2016, MNRAS, 457, 4296
Zackrisson, E., Rydberg, C.-E., Schaerer, D., Östlin, G., & Tuli, M. 2011, ApJ, 740, 13
Zaritsky, D., Kennicutt, R. C., Jr., Huchra, J. P., et al. 1994, ApJ, 740, 13
Zhang, H.-X., Puzia, T. H., Peng, E. W., et al. 2018, ApJ, 858, 37